TOOLBOX DEVELOPMENT FOR MINIATURE INTEGRATED PARTICLE ACTUATOR

A Dissertation

Presented to the Faculty of the Graduate School

of Cornell University

In Partial Fulfillment of the Requirements for the Degree of

Doctor of Philosophy

by

Yue Shi

January 2013

TOOLBOX DEVELOPMENT FOR MINIATURE INTEGRATED PARTICLE ACTUATOR

Yue Shi, Ph. D.

Cornell University 2013

Charged particle beam actuators such as particle accelerators and particle beam optics systems have wide applications in industry and academia, from medical and industrial diagnostics to investigations in fundamental science. This work details the preliminary efforts in the miniaturization of charged particle accelerators and manipulators to be highly compact and portable, by developing a toolbox of beam actuation components, which can be integrated for different applications. The three components that were developed are the electrostatic curved particle beam guide, a co-planar waveguide based RF resonator architecture for linear accelerators, and the Einzel lens for beam focusing. The central thesis is to use micro-fabrication techniques to attain micron precision in structures with 100-500 micron feature sizes, channels in which high electric fields ($>10^6$V/m) could be sustained to act upon charged particles. The use of electrostatic fields is feasible in many applications, eliminating the need for permanent magnets required in macro-scale charged particle systems. The micro-fabricated components utilizing electrostatic fields are realized on a planar substrate with the electrodes defined by micro-machined doped silicon or PCB copper, on a substrate such as silicon handle wafer or PCB dielectric. Within the planar implementation, the charged particle beam propagates in the plane of the substrate, with device sizes varying from 1cm^2 chips to cell-phone dimensions. Micro-fabrication processes were developed to accommodate electrically isolated actuator patterning, as well as multilayer high aspect-ratio structures. Planar fabrication and assembly would enable integration of the individual components of the toolkit with micron-precision channel-channel alignment within each layer. Ar^+ ion guidance of 90° and 127.5° are

demonstrated in 10μm channels of radii of 1mm and 2mm. On-chip Ar^+ ion acceleration and deceleration of 30eV is also shown with the use of longitudinal electrical fields of a linear accelerator channel (driven at 35MHz). Using an electrostatic lens focusing of a beam of 2keV electrons is achieved in the plane of the substrate, with focal length shifts of up to 167mm for lens actuating voltages up to 300V. The components of the charged particle beam manipulation toolkit pave the way towards miniaturized systems with applications including e-beam and ion beam imaging, lithography, x-ray generation, spectroscopy, biological scanning and ion-beam therapy.

BIOGRAPHICAL SKETCH

Yue Shi was born in Beijing, China to Zhou Shuqin and Shi Shaoqi and is their only child. Her earliest memories consist of train tracks, rides on the back of a bicycle and hopping among different schools. In 1989 she found herself on a plane ride and landed with her family in Harare, Zimbabwe. There, Yue attended Dominican Convent, a Catholic school for girls, through the Cambridge O- and A- level system, and graduated in 1999.

After a summer school in Johns Hopkins University, Yue enrolled in 2001 at MIT in Cambridge where she majored in Physics (Course 8) with the Electrical Engineering option. During her undergraduate years, Yue was involved in several different research projects and wrote her thesis at the MIT LNS Drift Gas R&D, a high energy physics laboratory and part of the LHC effort. She graduated with a B.Sc. in 2005.

Subsequently Yue entered Cornell University for a one-year M.Eng program (degree awarded in 2006) in the Applied and Engineering Physics Department She then continued on to pursue a Ph.D degree. After working for one year in a biophysics laboratory, Yue joined the SonicMEMS group in 2007, working under the guidance of Prof. Amit Lal.

To my parents

ACKNOWLEDGMENTS

I would first and foremost like to thank Prof. Amit Lal for his genuine creativity, resourcefulness, and love of engineering which are truly inspiring. He has taught by example, and has shown me wisdom and insight beyond pure academia.

I would especially like to thank Serhan Ardanuç for his engineering expertise and June Ho Hwang for his help on the AXIS project.

Thanks also goes to my labmates and friends of SonicMEMS for their patience, invaluable advice, help, moral support and encouragement: Janet Ching-Ping Shen, Abhishek Ramkumar, Steven Tin, Norimasa Yoshimizu, Shankar Radhakrishnan, Sarvani Piratla, Po-Cheng Chen, Jason Hoople, Kwame Amponsah, Yuerui Lu, Ved Gund, Sachin Nadig, Hadi Hosseinzadegan, Justin Kuo, Tiffany Cheng, Eugene Hwang, Prof. Sunil Bhave, Dana Weinstein, Manoj Pandey, Alper Bozkurt, Joseph Miller and Hamid Vajihollahi.

Gratitude goes to Prof. Clifford Pollock and Prof. Farhan Rana for their patience, advice and guidance.

I would like to acknowledge DARPA, the agency which funded my research under the AXIS program and seedling on the concept of curved electrostatic accelerators. Thanks also goes to the CNF staff, as well as the administrative staff Sue Bulkley and Daniel Richter.

I would like to specially mention Michael Hall, for his understanding and

encouragement through my years at Cornell.

Lastly, I would like to show my great appreciation to my parents who unfailingly supported me throughout my academic endeavors, and who believe in me still.

TABLE OF CONTENTS

LIST OF FIGURES

LIST OF TABLE

1. INTRODUCTION & MOTIVATION

The ability to control the transport of charged particle beams has been essential in the development of technology as a whole in the past century. Electron and ion beam imaging has afforded us the ability to look at surfaces at the micro and nano scales that were not possible before using light optics. Surface material properties could be changed by the addition, or doping of particles using ion beam tools. Indeed, the precise control of charged particle motion has been the tool upon which much of semiconductor fabrication and MEMS industry depend upon. In addition, X-ray generation from electron beams has made new medical diagnostic capabilities possible, while x-ray and ion radiation therapy have benefitted millions of cancer patients. Hard x-ray generation has opened up an entire field of crystallography to study protein structure at the atomic level.

It can be argued that much of the advances in the nanotechnology industry go hand in hand with advances made in the development of charged particle actuating tools. This work aims to miniaturize these particle beam manipulators by building a toolbox of miniature, planar, charged particle actuating components. These components would be highly integratable into compact, cost-effective systems such as an x-ray source using inverse Compton scattering, and electron beam lithography tools, among many other applications

The present work is devoted to the first efforts in the development of three components of the toolbox of beam actuating components: curved ion beam guidance, linear RF acceleration and focusing of electron beam with electrostatic Einzel lens. Particle guidance and acceleration will be described in Chapter 2, while Chapter 3 will discuss preliminary efforts in beam focusing. Each chapter will also suggest future work for device improvements. The experimental setup system which was built for device testing is encapsulated in Chapter 4.

1.1 Historical Perspective

The story of mankind's manipulation of charged particle beams began in earnest in 1838 when Michael Faraday passed an electric current through rarefied air filled glass tube, and noticed a strange light glow between the cathode and the anode. In subsequent decades, this glow or rays were shown to follow magnetic field lines and was called "cathode rays". Hittorf confirmed in 1869 that these rays indeed travelled in straight lines (without magnetic fields), and if an object were placed in the illumination, its shadow would appear on the anode side screen. Varley (1871) suggested the rays were made of particles and in 1896 Thomson measured the charge/mass ratio – calling them "electrons".

At the time there was a great debate on whether the rays were corpuscular in nature (made of particles) or of a wave structure (a disturbance of an ether). Hence there was a lot of experimental interest in cathode rays and in 1895 Röngten discovered that a screen near a cathode ray source was fluorescing without any other known sources nearby. He found that this radiation can travel through paper and photographic plates and called them x-rays [3]. He took a famous x-ray image of his wife's hand with her wedding ring. There was great excitement at the time about this mysterious radiation which could penetrate certain materials. Indeed the ability to use x-rays to image inside the body transformed medicine and surgery forever. One of the major applications for the present project (Section 1.5) is to realize a compact x-ray imager (by actuating electron beams onto a metal target) with greater portability than current x-ray equipments would allow. The discovery of x-rays were one of the first experimental results to upset the complacent view at the close of the 19^{th} century that all physics of the natural world were discovered and could be described by Newtonian classical mechanics, thermodynamics and

electromagnetic waves (Maxwell's equations).

In addition to x-rays, the discovery of the electron, the photoelectric effect, blackbody radiation among others, revealed shortcomings of the classical theories. To correct for these discrepancies, the beginning decades of the 20th century saw investigations that would lead eventually to the quantum theory, which describes phenomenon on the atomic scale. In 1909 Rutherford saw the backward reflection of alpha particle on gold foil which confirmed the hard core nature of the nucleus. However the resolution at which he could investigate the atom is limited to the energy of the probing particle (in Rutherford's case alpha particle). In order to attain better resolution and to reveal finer details of the fundamental structure of elementary particles, the energy of the probing particle must be increased since the wavelength λ and hence resolution, associated with the particle, is related to its momentum p (and hence energy) as $\lambda = \frac{h}{p}$. Later, when a concerted effort was being made to uncover ever heavier particles, in order to produce them, particles with ever greater energy E would be needed as: $E = mc^2$ [4]. Therefore, a tremendous need arose for the ability to generate high electric fields to accelerate the charged particles.

Immediately after World War I, there were no accelerators. In fact Rutherford used naturally occurring elements undergoing alpha, beta, and gamma decay, not accelerated ones, for his experiments. The first attempts at making accelerators used DC electric fields to accelerate particles. Electrical breakdown, even in vacuum, was a problem once a few tens of kilo-volts was reached. The first high voltage generator to approach 1MeV was made by Cockroft and Walton utilizing voltage multipliers of diodes and capacitors to stack up the voltages on the capacitors. In 1932, they were able to accelerate protons to hundreds of keV, and became the first to transmute an element (Li) into others (Helium included) by bombarding with protons. These

were the first nuclear reactions triggered. (They received the Nobel Prize in 1951). Another direct high-voltage generator was proposed by Van de Graaff (1929) to mechanically carry charges by a conveyor belt from low potential to a high potential collector - several MV could be reached.

As even higher energies were required, other acceleration schemes were proposed. Gustav Ising of Stockholm proposed the first multi-stage acceleration (in a straight line) concept to lower the high potential, in 1924 [5]. Wideröe realized the first linear accelerator (1927), while the first proton accelerator was built by Alvarez in 1946, using the newly available high frequency power generators that were developed during World War II for radar purposes. See section 2.2 for more details. E. O. Lawrence was at first involved in building a linear accelerator after Wideröe's design, and in trying to make the LINAC more compact, Lawrence designed the "cyclotron" in 1930 [6]. In this device, acceleration occurs between 2 "dee" shaped electrodes, with the particles following a circular trajectory, due to a magnetic field acting perpendicular to the plane of particle motion. He was awarded a Nobel Prize in 1939. Particle physics itself developed with ever increasing sizes of accelerators to target higher and higher energies. Many accelerators are the size of football fields e.g. the Cornell High Energy Synchrotron Source (CHESS) which produces x-rays of up to 8GeV [7]; the Tevatron at Fermilab (the second largest particle collider at 1GeV) [8]; and the largest collider in the world, the Large Hadron Collider (LHC) [9] which comprises of a tunnel 17km long in circumference to reach proton energy of up to 7TeV.

Charged particle beams are not only useful at such high energies, but have many applications in industry in the much lower energy range in the keV and MeV range. In the late 1930's in addition to requirements for particle physics, industrial demands such as the electron

microscopes, cathode ray tubes and television also drove the need for coherent particle beams to be maintained over long distances - namely the ability to confine the beam in a slowly varying radius about the axis of propagation. Busch and his contemporaries showed that axial symmetric magnetic or electric fields acts like a lens on charged particles [10]. This means that the beam can be focused and imaged, similar to light optics. World War II saw the development of microwave devices such as the klystron and magnetron [11] which, in combination with resonator cavities, made accelerators like Alvarez's design possible for a variety of industrial and scientific instruments. Here some will be briefly mentioned. Since the times of Röngten, x-rays generated by accelerated electron beams are not only used for radiography, but also for tomography, fluorescence imaging and radiotherapy for cancer treatments. High energy x-rays, such as that produced at CHESS, are essential in the study of the crystal structure of molecules. [12] [13] [14]. Ion beam cancer therapy, which involves exposing tumor regions with a beam of ions such as protons and carbon, pin-point the targets with greater precision and are more localized than x-rays [15] [16], [17]. High resolution images of material surfaces are routinely rendered by scanning with electron beams down to the nanometer scale. Some of these charged particle beam microscopes include: the scanning electron microscope (SEM) which operates with 1-30keV electron beams; the transmission electron microscope (TEM); the scanning tunneling microscope (STM); and the Focused Ion Beam microscope (FIB) [18].

As machining and assembly capabilities became more precise, allowing for smaller feature sizes in the 20th century, the instrumentation of accelerators and beam optics systems became more compact. Brief reviews of miniaturization efforts in the past few decades for keV to MeV accelerators will be given in Chapter 2, and Chapter 3 will discuss similar efforts for electrostatic focusing. In the footsteps of Ising, Wideröe, Alvarez, Lawrence, Busch, and other

pioneers of charged beam actuation, the present project also aims to miniaturize century old technologies, to ever more compact sizes with the novel capability of complete systems integration, using 21st century micro-fabrication techniques.

1.2 Central Design Concept – High Aspect Ratio Planar Structures

In traditional accelerator structures, the potential defining electrodes which focus and/or accelerate a charged particle beam, are assembled by stacking disks/cylinders of metal with a hole running through the whole stack/column (Figure 1.1a). In this geometry the beam travels perpendicularly to stack plane. Voltages can be applied to each individual disk, which is separated from its neighbors by air or an insulating material e.g. ceramic disks. The entire column is held together mechanically by tethers to the external anchoring structure. This assembly method is common for SEMs and electron beam lithography tools. In addition to electrostatic focusing, magnetic coils may also part of the column.

The main disadvantage of this method is the limited capability to integrate with and align to subsequent components, for example from a focusing unit to a circular storage ring. Alignment and mechanically adjusting the relative distances and tilt of the disks/cylinders, may be labor-intensive and time-consuming during assembly. In addition the limited selection of disk thicknesses can limit the possible design space. [19] [20] [21] [22]

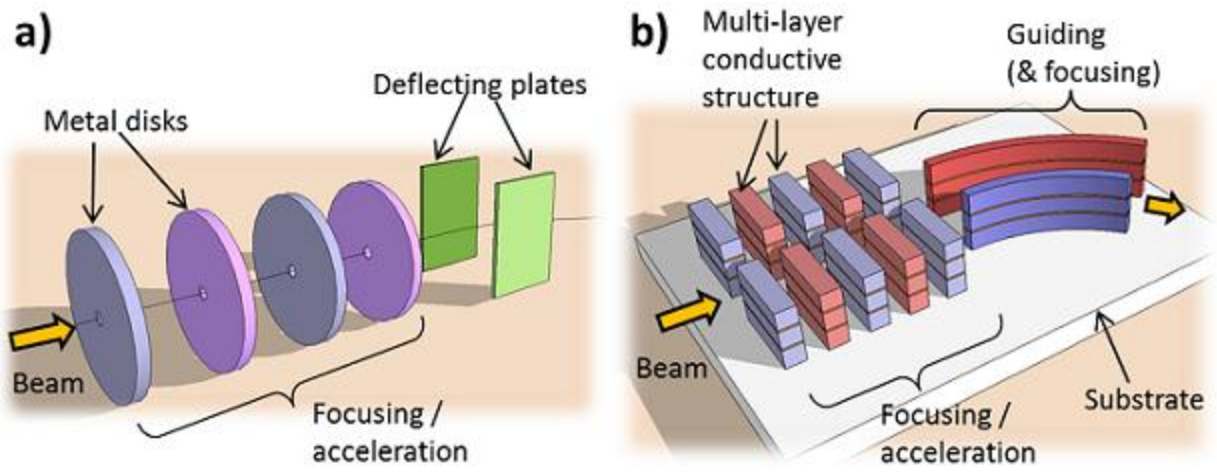

Figure 1.1 Illustration of a) Traditional geometry of electrodes placed so that beam passes perpendicularly through the stack which could be used for focusing or acceleration; deflection by a pair of parallel plates with high potential difference in between. b) Planar geometry developed in this work where the beam travels in the plain of stacked layers of conductors. The layers can be cut to separate out individual electrodes. The beam passes through a focusing/acceleration section first before having its path curved by guiding electrodes.

We present *planar* actuation structures, in which the beam travels *in the plane* of the substrate (Figure 1.1b). Within each layer, the channels (running in-plane) are defined by electrode walls that are precision laser-cut. Hence not only is the electrode-to-electrode alignment precise, but so is the channel-to-channel alignment. The latter is important when the particle beam track threads through different actuating components e.g. from an Einzel lens to an accelerator. Furthermore, the electrode thickness and spacing are flexible and well controlled via lithographic patterning with lithographic tolerances. As the thickness of the conductive layers defines the height of the channel walls, similarly patterned layers can be stacked together to bring about high aspect ratio channels.

If the layers are insulated from each other (e.g. by a layer of silicon-oxide) each layer can be electrically addressed separately. In the case of through-substrate cutting, like that of the

Einzel lens described in Chapter 3, the relative positioning of electrodes can be fixed with tethers which are cut afterwards. This opens up the possibility for electrical quadrupoles, hexapoles and other configurations for out-of-plane focusing.

An important consequence of planar patterning is that the entire system, from beam extractor to the final target placement, can be fabricated and aligned in one substrate. Microelectronic circuitry, also of planar construct, can be packaged with such a charged particle manipulation system. The result is highly integrated system very much resembling the concept of IC for circuits, that is highly compact, of reduced size, and cost effective. Figure 1.2 shows such an envisioned vacuum package, which is designed to be highly portable.

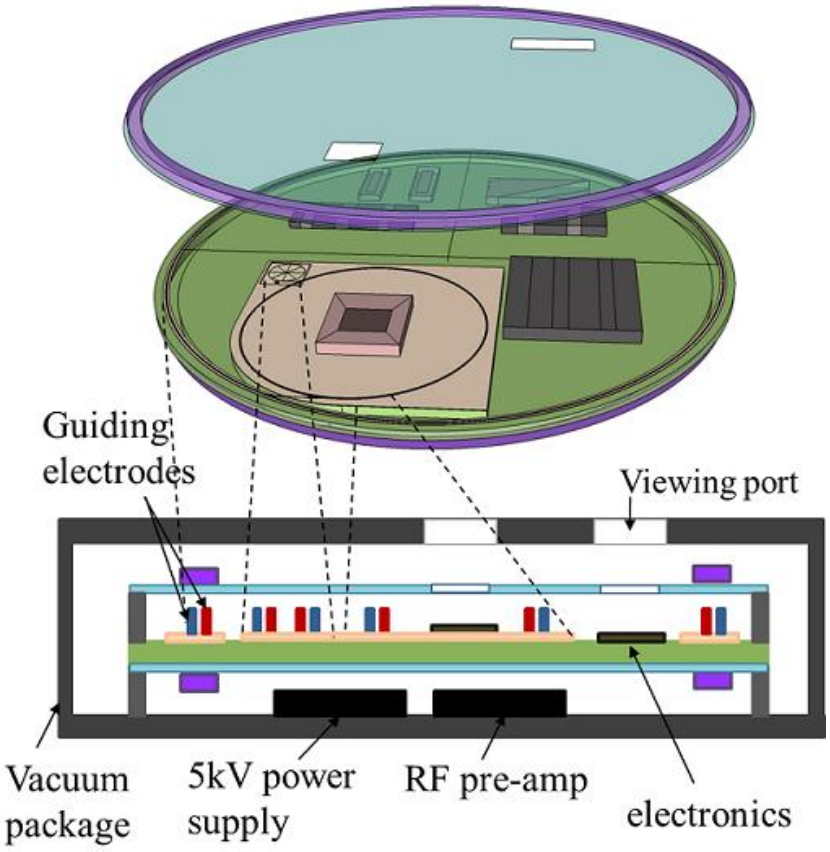

Figure 1.2 Envisioned concept of a charged particle actuating system integrated with circuitry for electric control of actuators. TOP: a 3D illustration of planar integration of particle guides and electronics. BOTTOM: side view of a vacuum packaged system that may be suitcase-sized, with particle actuators and power supply.

1.3 Fabrication Challenges

A crucial part of this work is the development of planar micro- device fabrication processes. As the device requirements evolved, several processes were developed, mainly for Si-based micro-machining. For each of the actuating devices fabricated, a fabrication flow is given: Section 2.1.3 for ion guides; Section 2.2.3 for accelerators; Section 3.4 for Einzel lens. One would question the reason for using different processing and tools for these 3 types of devices,

when in principle they should be all be fabricated the same way. Indeed with the long term goal of integrating all of these varied components on the same substrate, it is envisioned that the components would be patterned at the same time, undergoing the same processing steps. However, this is work under development and with each iteration, which may involve the next device to be studied, different device requirements were addressed. At times for fast processing, printed circuit boards (PCB) were patterned to show proof of principle for example in the case of guidance channels (Section 2.1). Here, general device fabrication considerations are discussed in view of an overall theme of aiming to develop a process which allows for a seamlessly integrated particle actuating system.

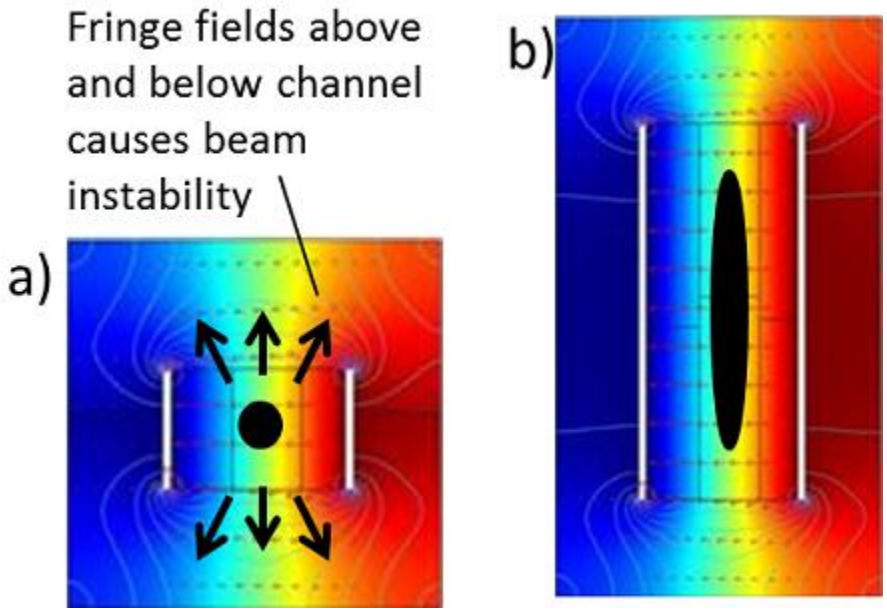

Figure 1.3 The importance of high aspect ratio channel walls. COMSOL simulation of the potential in the cross-section of a channel defined by 2 electrode walls. a) Lower aspect ratio causes more particles to be lost due to fringing fields at the top and bottom regions of the channel. b) Beam flux is enhance when the aspect ratio is higher.

Central to this thesis is the development of a fabrication process that will realize a high

aspect ratio structure with electrically isolated multiple structure layers. High channel walls are essential to minimize the effect of fringing fields near the wall edges (Figure 1.3), and hence reduce the amount of current flux lost due to fringe fields at the channel top/bottom edges. Therefore the channel walls not only needs to be conductive but also high (thick layer on substrate) compared to the channel spacing. In selecting the material for the conductor, several considerations were taken into account. The most obvious choice is metal, however thick metals layers such as copper are not easily patterned with vertical side walls, especially under wet etch. Metal sheets themselves bend/crease regularly and so lack the rigidity required for the device.

On the other hand, commercial doped Si exhibit resistivity down to 0.001Ω-cm which is adequate for low current operations - the electrodes are either held at DC constant voltage, or act as capacitors drawing minimal current in the RF accelerator case. Although less conductive and more brittle, Si retains its rigidity in thin layers and micron feature sizes. It can also be machined with high aspect ratios by Deep Reactive Ion Etching (DRIE) or laser-cutting. Si wafers of thicknesses greater than 500μm are readily available commercially. In addition, the channel height can be increased by stacking layers of similarly patterned channels. Therefore highly doped Si was the material of choice for channel structures. The process development started with DRIE of silicon-on-insulator (SOI) wafers since micro-fabrication processes are well characterized and prevalent in MEMS. The first devise fabricated with this process are the curved guides and linear accelerator (Chapter 2). But SOI itself is not an ideal platform for multilayer electrode stacking, and are more costly than plain doped wafers. Hence through-wafer etching of plain Si was adopted as being more efficient.

The other main concern of fabrication process is of course the method of etching Si itself. As different micro-machining methods were explored, laser-cutting was favored over DRIE as

the former is in-house (readily accessible) and relatively inexpensive, requiring no lithographic masks and hence cutting down the number of fabrication steps. The DRIE process leaves a layer of polymer on the etched side walls which could build up charge after prolonged particle beam operation. However, laser-cutting limits the feature resolution to 100-200 μm, and the wall roughness is about 10 μm. But for channel spacing of greater than 500 μm, the surface roughness leads to very small variations in center-to-channel electric fields due to field divergence. Cleaning is required after laser cutting to remove the Si debris which could short neighboring electrodes. Alternative process flows such as LIGA [23] can allow for high aspect ratio structures, but it is hard to obtain multiple layers of LIGA structures. In Chapter 3, the Einzel lens device is shown to be fabricated with laser-cut, and stacked doped Si.

1.4 Beam Current Limit

Extensive literature has been dedicated to the dynamics charged particle beams [10], [24], [25], and this chapter cannot hope to extensively cover the theoretical details of charged beam propagation. However, of practical interest to this work is having a rough knowledge of what beam current is physically permissible in miniaturized structures. The maximum current allowable in practice may not ever be reached due to the beam losses that are certain to occur in any system. However an upper bound on the current limit is useful in the context of potential applications this type of technology may be relevant for. This section will consider longitudinal current limiting factors due to space-charge effects and that allowed in an accelerating gap, as well as touching upon the transverse expansion of a drifting beam.

Although miniature particle emitting sources were not fabricated in this work, and commercial ion or electron guns were relied upon for device testing, the long-term goal of

building an integrated particle actuating system will no doubt require such compact sources. Hence, the amount of current that can be supplied by the source material will also ultimately be a limiting factor. Of the greatest practical interest to such a long-term goal of an integratable source are thermionic and field emission for electrons, and plasma formation and extraction for ions. Briefly then, in Appendix A.3 thermionic and field emission limits will be touched upon.

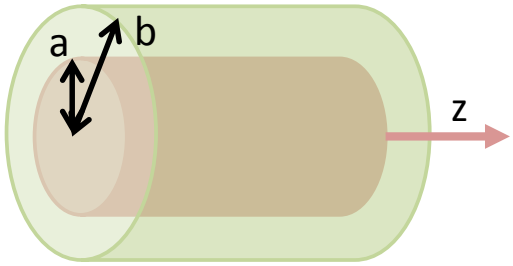

Figure 1.4 Illustration of cylindrical charged particle beam model.

1.4.1 Self-field Potential Limit

The beam current is ultimately limited by the charge repulsion between the particles. This is termed the space charge effect. The particles will experience forces due to the potential field set up by other particles in the beam. If one models a beam simply as a cylinder with constant radius *a* (Figure 1.4), prevented from expansion by some external field (e.g. magnetic field), and transported inside a tube of radius *b*, then the potential in the middle of the beam *r=0* (due to the beam charges itself) is (see Appendix A.1 for derivation) [10]:

$$\phi(0) = \frac{I}{4\pi\varepsilon_0 v}\left(1 + 2ln\left(\frac{b}{a}\right)\right) \qquad (1.1)$$

where *I* is the beam current with particle velocity *v*. As a particle with initial kinetic energy $(\gamma_0 - 1)mc^2$ enters the cylinder, at the center its kinetic energy is reduced by $q\phi(0)$ such that,

$(\gamma_0 - \gamma)mc^2 = q\phi(0)$, where q is the charge. The limit is reached when all of its kinetic energy is sacrificed to the potential energy: $(\gamma_0 - 1)mc^2 = q\phi(0)$. The current limit derived from Eqn.1.1 can be shown to be [10]:

$$I_L = I_0 \frac{\left(\gamma^{2/3} - 1\right)^{3/2}}{1 + 2ln(b/a)} \tag{1.2}$$

where

$$I_0 = \frac{4\pi\varepsilon_0 mc^3}{q}$$

Eqn. 1.2 assumes that $b>a$ so that the beam edge is some distance from the tube wall. This current limit is plotted for 3 types of particles of interest assuming $b=a$, in Figure 1.5 for the particle energy range 0.5keV – 10keV. We see that above 2keV, the limit for electrons is on the order of amperes, for protons tens of milli-amps, and for argon (Ar^+), milli-amperes. Figure 1.6 shows the plot for energy range 10-100keV, and Figure 1.7 for range 100keV-1MeV.

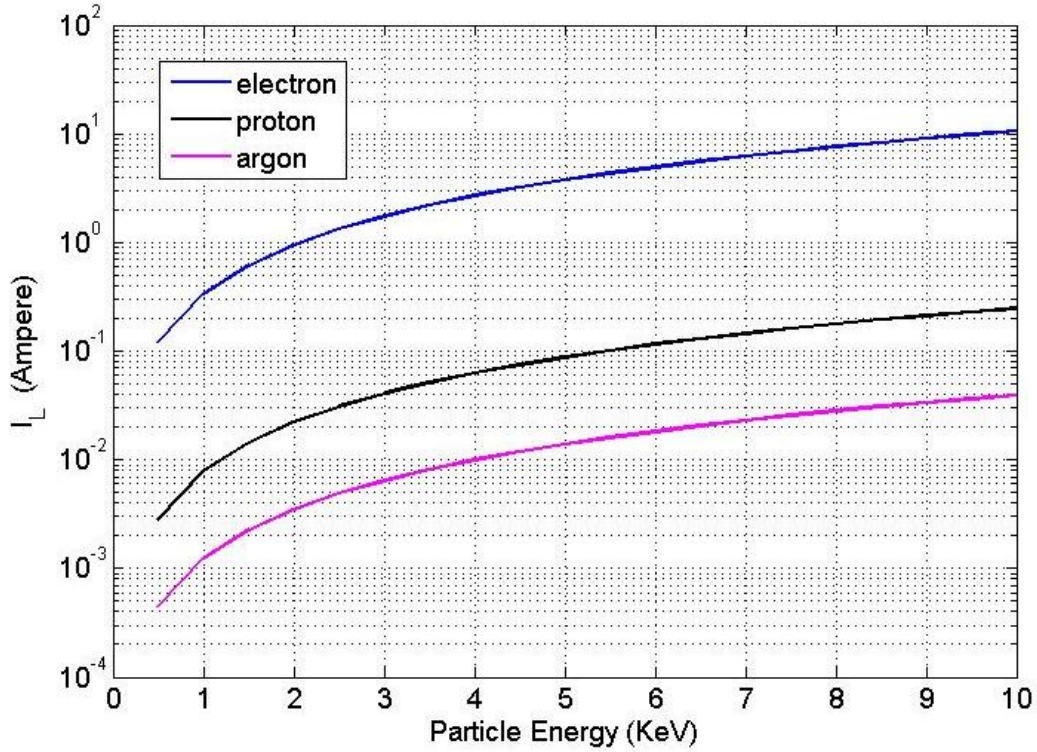

Figure 1.5 Current limit from space charge for a cylindrical model as a function of beam energy for 3 types of particles. Assumption: *b=2a.*

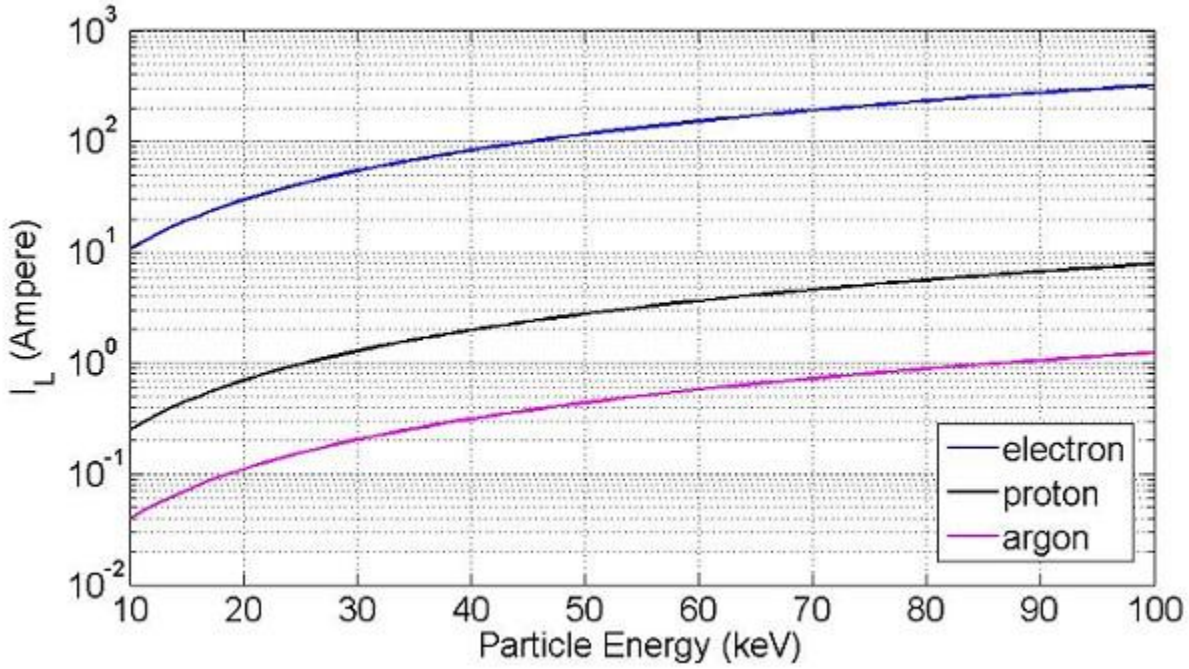

Figure 1.6 Current limit from space charge for a cylindrical model as a function of beam energy for 3 types of particles with energy ranging from 10keV to 100keV. Assumption: *b=2a.*

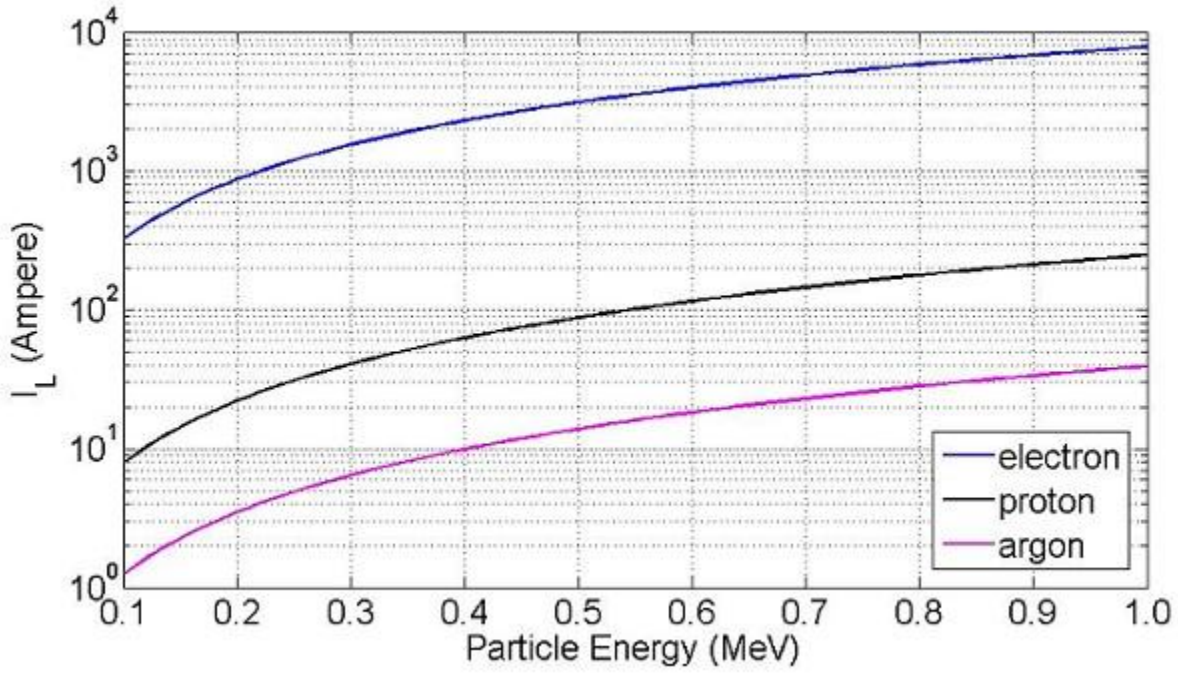

Figure 1.7 Current limit from space charge for a cylindrical model as a function of beam energy for 3 types of particles with energy ranging from 100keV to 1MeV. Assumption: *b=2a.*

The current limit in Eqn. 1.2 is the ideal case which assumes a continuous external force to constantly act on the beam, keeping its diameter to a minimal. Although this estimate is useful, in practice such uniform continuous external force is very hard to maintain. More often than not, the beam traverses regions of space with little or no focusing forces, hence the beam is allowed to expand. Hence the ability to focus the beam is very critical, for example in a periodic structure, to maintain a decent flux throughout the device/system. Chapter 3 describes electrostatic focusing which was chosen to be implemented in this work.

1.4.2 Child-Langmuir Limit

The amount of current is also limited where there is a change in potential of V_0 across a gap distance of d (Figure 1.8), given by the Child-Langmuir law [10]. The longitudinal electric fields (along trajectory axis) resulting from the space-charges inside the gap limits the number of particles that can be pushed into the gap. Hence this current limit applies to gaps at the extraction electrodes near the beam source, and in the gaps between accelerating structures (Section 2.2). The Child law [24] relates the current density limit J to V_0 and d taking onto account the initial energy the particles enter the gaps with:

$$J = \frac{4\varepsilon_0}{9}\sqrt{\frac{2Zq}{m}}\frac{V_0^{\frac{3}{2}}}{d^2}G(\chi) \tag{1.3}$$

where

$$G(\chi) = \chi^{3/2}\left[\left(1-\frac{1}{\chi}\right)^{3/4}+1\right]^2$$

and

$$\chi = \frac{\phi_2}{\phi_2-\phi_1}$$

with ϕ_1 and ϕ_2 the entrance and exit potentials of the gap respectively. See Appendix A.2 for more detailed derivation.

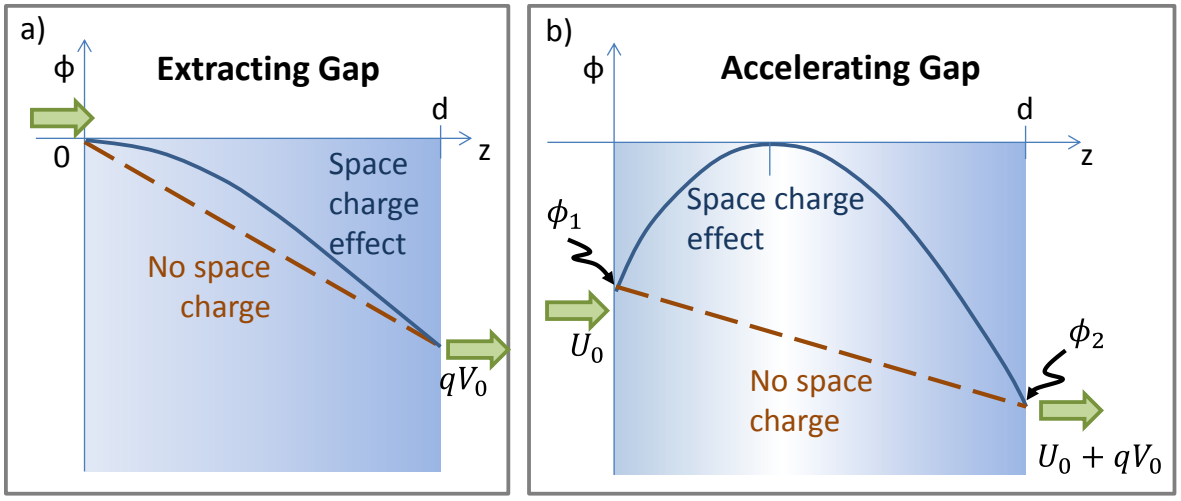

Figure 1.8 Illustration of space charge effect on the potential in a) an extraction gap with initial particle energy almost zero, and b) an accelerating gap with initial energy of U_0. With no space charge the potential profile is linear (brown line). But the presence of space charge changes the potential seen by incoming charges (blue line).

If a charged particle has no initial velocity, $G(\rho) = 1$, then once the field at the entrance becomes repulsive, it may not enter the gap. Figure 1.8a) illustrates the effect of space charge on the potential in such an extraction gap, applicable near emission sources for beam extraction. Charged particles are passed into the gap until the potential gradient at the entrance becomes zero. If more were to enter, a repulsive field would be set up. Figure 1.9 is a plot of the Jd^2 product varying with gap voltages that are realistic for the devices in this work.

For a particle with significant initial velocity, it may still enter the gap even if it sees some repulsive force at the entrance, $G(\rho) > 1$. The space charge potential is illustrated in Figure 1.8b) and the current limit is reached when new particles can no longer overcome the potential at the entrance. Figure 1.10 shows this corrected current limit for accelerating gaps in, for example a linear accelerator (Section 2.2).

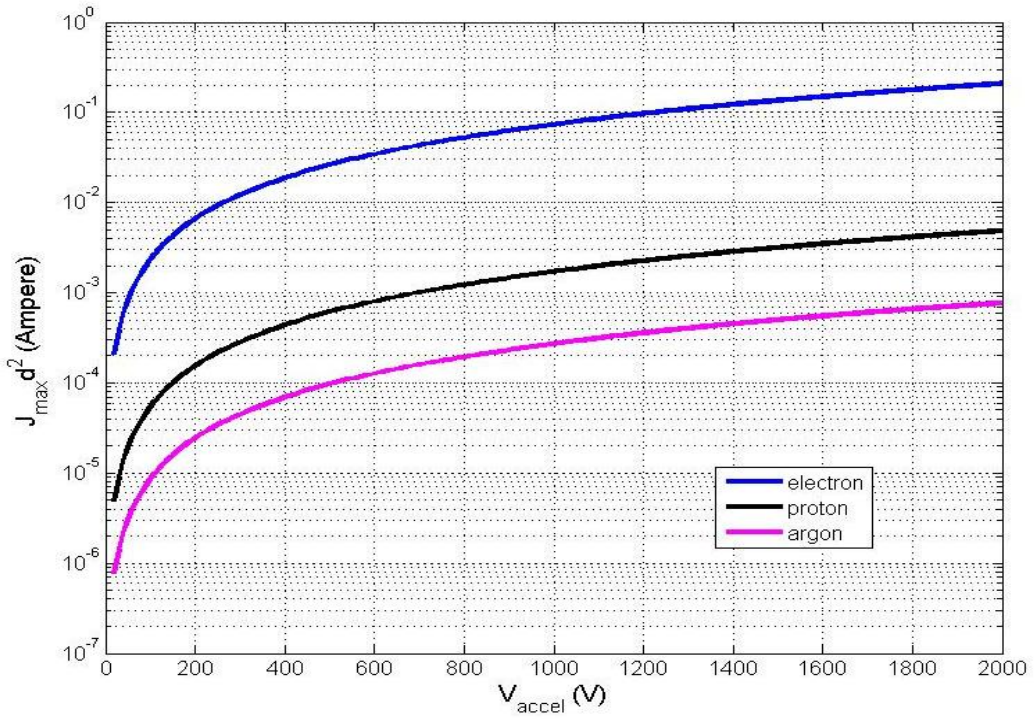

Figure 1.9 Child-Langmuir current limit for longitudinal extraction gap as a function of applied gap voltage, for 3 particles without correction factor such that $G(\rho)=1$.

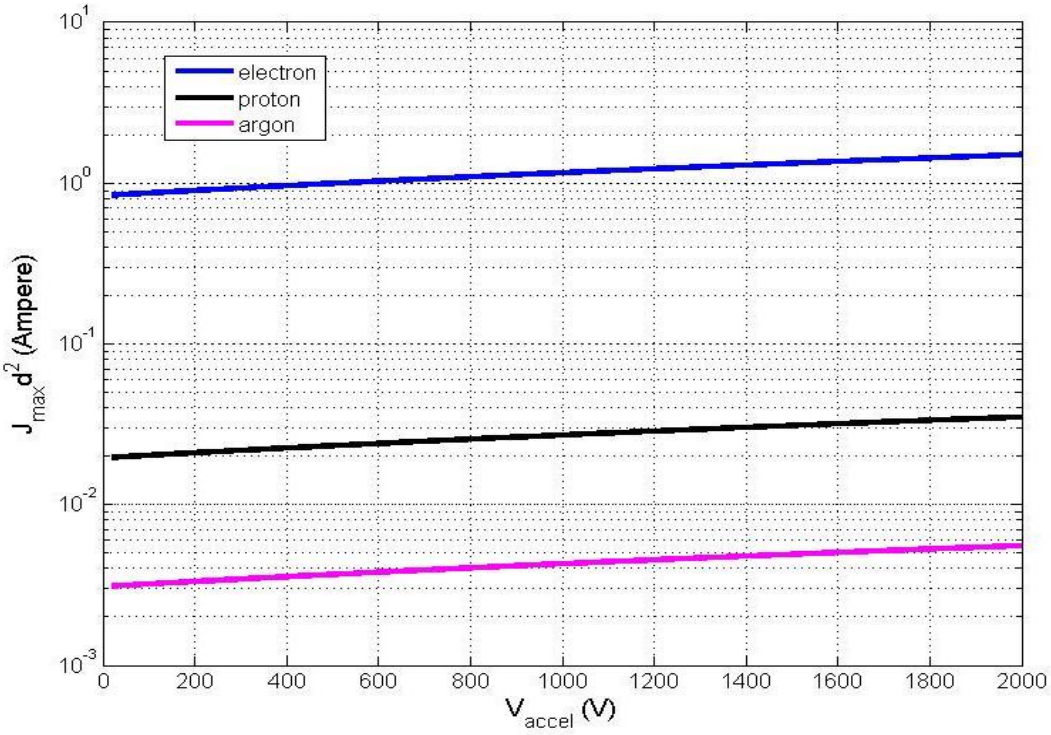

Figure 1.10 Current limit of Child law corrected for initial injection energy of 2keV so that $G(\rho)>1$, for 3 particles.

Comparing Figure 1.9 and Figure 1.10 we see that the $G(\rho)$ factor correction increases the current limit by an order of magnitude. Hence the current limit of an entire beam actuation system is dependent on the beam extraction section. The gap distance inversely affect the beam current density as is evident from Eqn.1.1.3. For the designs of linear accelerators then, this is another reason to minimize the accelerating gap. Higher accelerating voltage is also beneficial to beam current. In Figure 1.11 some values for current density are calculated for $200V<V_0<500V$ and $100\mu m<d<170\mu m$. Conventional SEM systems typically operate at $10^6 A/m^2$. For example, with a gap size of 130μm, the gap voltage should be around 360V to reach this current density.

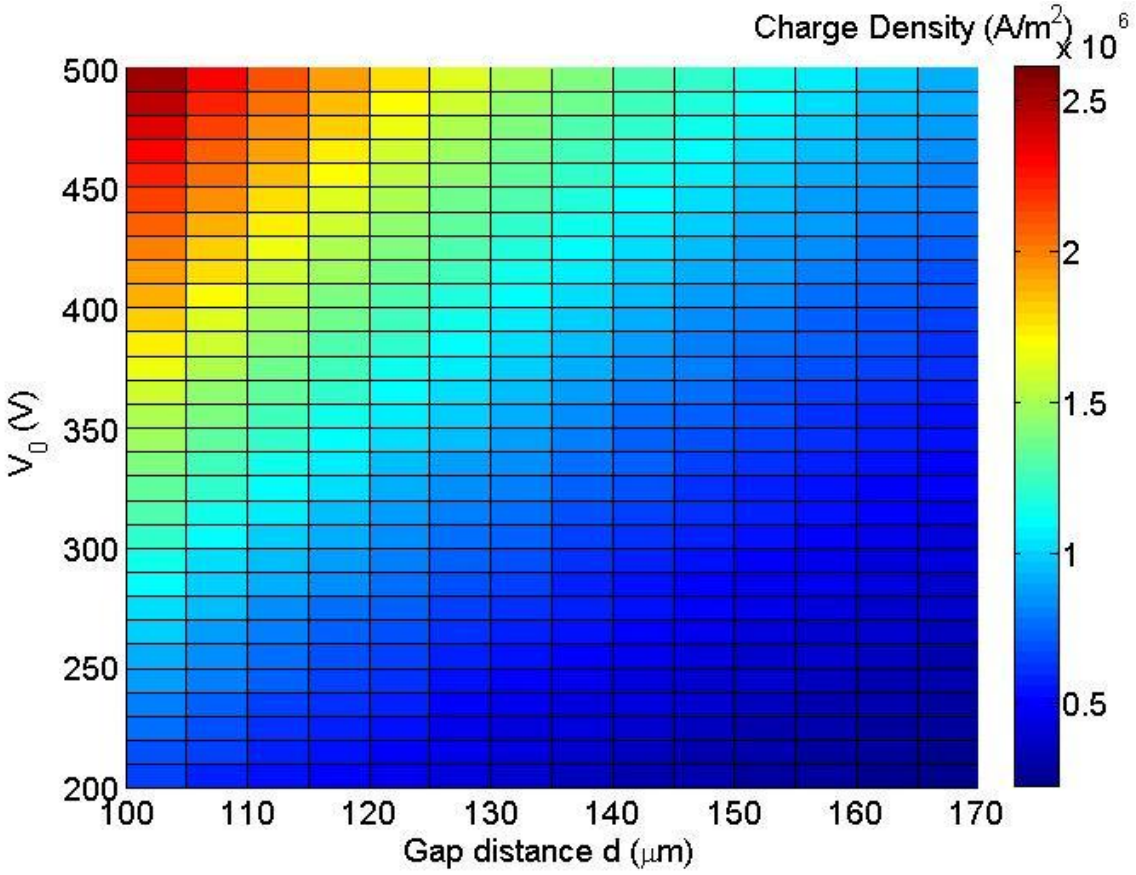

Figure 1.11 Child-limited electron current (shown in color scale) dependence on gap voltage V_0 and gap distance d. Note that for most SEMs today the current density is about $1x10^6$ A/m^2

1.5 Potential Applications

1.5.1 Miniature Einzel Lenses

In principle, a multitude of Einzel lenses can be fabricated on one substrate layer. Through a stacking of substrates, one can realize an array of charged beamlets, each independently controlled as shown in Figure 1.12. Such a device could be used for electron lithography applications. Furthermore, the array of beamlets allows for the precise control of x-ray generation if they target a metal. Localized x-ray generation will greatly aid in medical imaging including phase-contrast imaging.

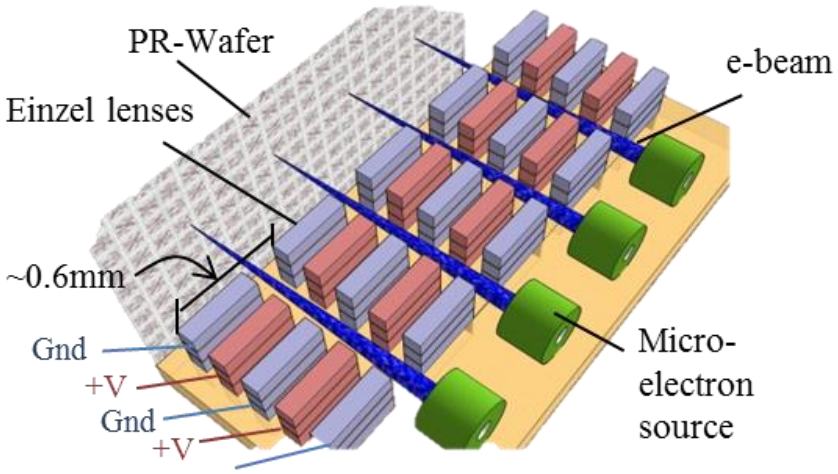

Figure 1.12 Envisioned miniature lithography system with a multitude of beamlets controlled (deflect and focus) individually by Einzel lenses.

1.5.2 Energy Analyzers

Much work has been done on the miniaturization of mass spectrometers [26] and energy analyzers. Some popular electrode configurations are the parallel plate, the

cylindrical and the spherical analyzer. As planar geometry is of interest to this work, the cylindrical configuration is the most relevant. The 90^0 curved guide detailed in Section 2.1 can be used as an energy analyzer, and is used as such in Section 2.2 to determine the resultant energy from acceleration (Figure 1.13). In the most simplistic model of a cylindrical geometry, the energy resolution of the analyzer goes as:

$$\frac{\Delta E}{E} = \frac{w}{r}$$

where E is the particle energy, w the width of the guide channel and r the radius of curvature of the channel. Since w can be made small by microfabrication techniques, in principle, the energy resolution can be greatly enhanced. With the incorporation of a B-field, particle mass can also be found and spectrometers are made possible.

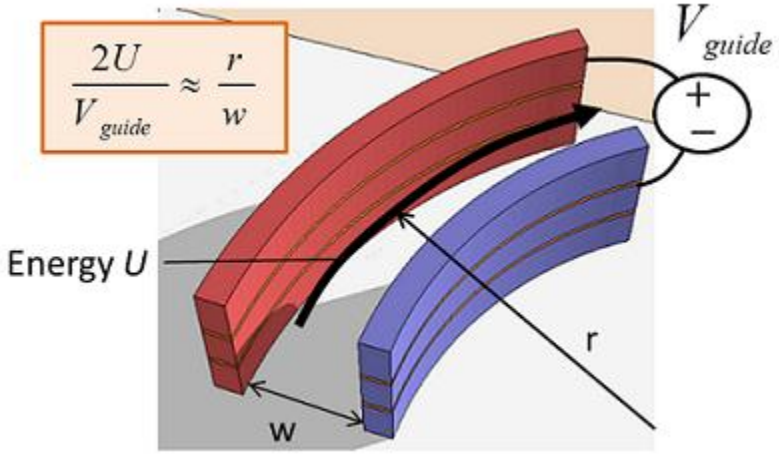

Figure 1.13 Illustration of cylindrical curved guide as a particle energy analyzer. Only particles with particular kinetic energy U can be guided by potential V_{guide} around a radius of curvature r. Hence this structure acts as an energy filter or analyzer. The energy resolution thus obtained depends on the width of the channel w.

1.5.3 X-Ray Generators

X-rays of a few MeV is useful for medical imaging, hence the electron beam for x-ray generation must at least be at that range. To reach the MeV level, electrons could be accelerated in stages. Low energy electrons can be first accelerated with the linear RF accelerator described in Section 2.2 to several hundred KeV. At this energy level, the addition of magnetic beam containment would be required since at speeds close to *c* the magnetic field force becomes significant. For example, at 500KeV, the electron speed is 0.86*c* and the magnetic force in a 1.5T field is $3.87 \times 10^8 q$, whereas the electric force within a 100μm wide channel of 300V across (taking into account electrical breakdown), is $3 \times 10^6 q$, a two orders of magnitude difference.

However, in the low energy regime, RF acceleration and electrostatic focusing and guiding are sufficient. Without bulky and heavy magnets the actuator components are easier to integrate on planar architecture. Figure 1.14 shows an illustration of an particle acceleration system that first takes the beam to hundreds of KeV with a linear accelerator and then to MeV with a race-track implementation in which the particles are cycled through an RF cavity, guided by permanent magnets. All the components of the system from focusing units to accelerator are elements in the toolbox that is being developed in this work.

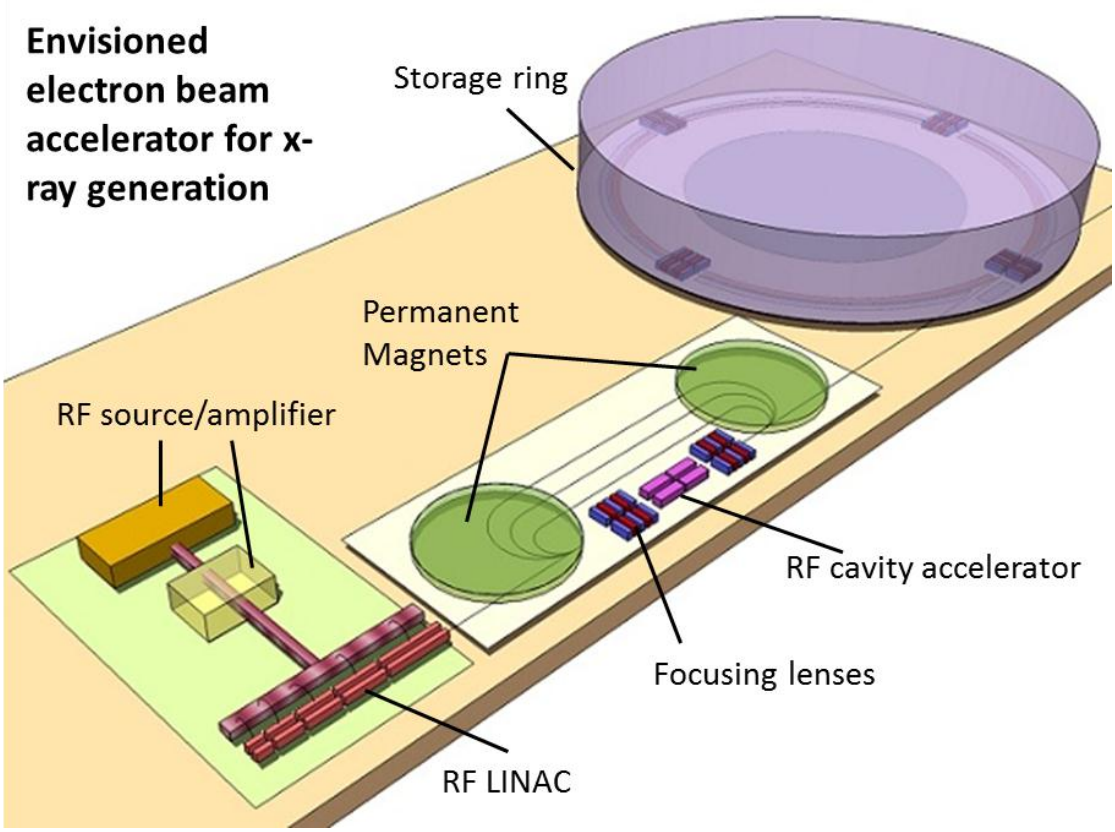

Figure 1.14 Envisioned electron beam accelerator to reach MeV for x-ray generation. Initially the beam enters bottom left and is accelerated by linear accelerator to hundreds of KeV. The next section utilizes magnets to curve the beam in a race track to be accelerated to MeV, then possibly into a storage ring.

2. Argon Ion Manipulation: Guidance and Acceleration

This chapter describes the basic theory and implementation of two essential components of the charged particle manipulator toolbox: electrostatic beam guidance around a curved path, and acceleration of particles by the RF linear acceleration method. In terms of beam transport, the ability to bend the trajectory of the beam in small radii of curvature is important to realize miniaturized charge particle systems. By bending the beam, the beam path can be folded repeatedly to be passed through an accelerating section multiple times, until the target energy is reached. Section 2.1 describes the first efforts in such electrostatic bending of beams, namely for 90° and 127.5° bends as well as the curved structures' use as a particle beam energy analyzer. In Section 2.2, preliminary efforts in realizing a micro-fabricated accelerating charged particles with a RF planar structure will be described as well as an outlook for future designs.

2.1. Curved Ion Guidance

The advantage of using micro-fabrication techniques to define charged particle actuating structures on a planar surface, is that structures such as electrodes can be curved with relative ease and micro-scale precision, as compared to more traditional methods such as metal machining, bending, and forming. Hence the meandering structures can trace the desired particle beam track in almost any curved contour. Furthermore two curved electrodes can be fabricated close together to realize small channel gaps with the voltages on the electrodes forming an electric field acting on the particles along the guided path. The charged particles can continuously experience the high electric field caused by even moderate voltages due to the small dimensions. This allows for high degrees of curvature in the case of low energy charged

particles, and continuous focusing control (Chapter 3). Since the gap dimension between electrodes can be fabricated down to 100μm using laser micromachining or DRIE, , the electric field within that gap can be on the order of 10^6-10^7V/m when ~100V is applied across that gap. As was discussed in Section 1.4, the theoretical beam current limit allowed at such channel gap dimensions and gap potentials is practical for applications including electron-beam lithography, electron microscopy and energy analyzers.

2.1.1. Comparison to Magnetic Field Particle Guiding and Advantages of Electric Field Guiding

Magnetic fields are often used to bend the paths of charged particles in curved shapes in accelerators such as the cyclotron and the synchrotron. Figure 2.1 shows the B-field required to bend three particle species around the radii of curvature of 10mm and 4mm, which are examples of dimensions relevant to miniature particle systems of interest. Commercial permanent magnets possess field strength of up to 1.7T. Hence without the use of electromagnets, only low energy electrons and possibly protons can be kept in a 10mm orbit using permanent magnets.

To reach the high magnetic fields required for compact charged particle beam guidance, electromagnets are essential. However, the use of electromagnets would not be appropriate in terms of reducing the power consumption and size of accelerators. Electromagnets consume a large amount of power due to the high electric current required to support the magnetic field flux – much of the power is lost to heating in metal, and an extensive cooling system (which is also power hungry) is required to remove that heat for

intense field production. Electromagnets are predominantly bulky, and the coils involved are especially not amenable to integration into a planar device structure.

On the other hand, electrostatic guidance of charged particles is attractive in terms of ease of integration into a planar device geometry, space consumption and power requirements. Between closely positioned electrodes, there is negligible current flow (assuming no voltage breakdown), and therefore very low power consumption. Figure 2.2 compares the B-field strength and the guiding voltage (across a channel gap) that are needed to bend an argon ion around radii of 10mm and 4mm. (These radii values are arbitrarily chosen to be representative of the size of curvature in miniaturized charged particle actuation systems). The amount of potential difference that is needed to be applied across the gap for curved guiding within millimeter radius, are reasonably below electrical breakdown (which is mentioned in Section 4.3). All electrodes are defined on a plane with advantages of microfabrication in terms of cost and the ease to scale down.

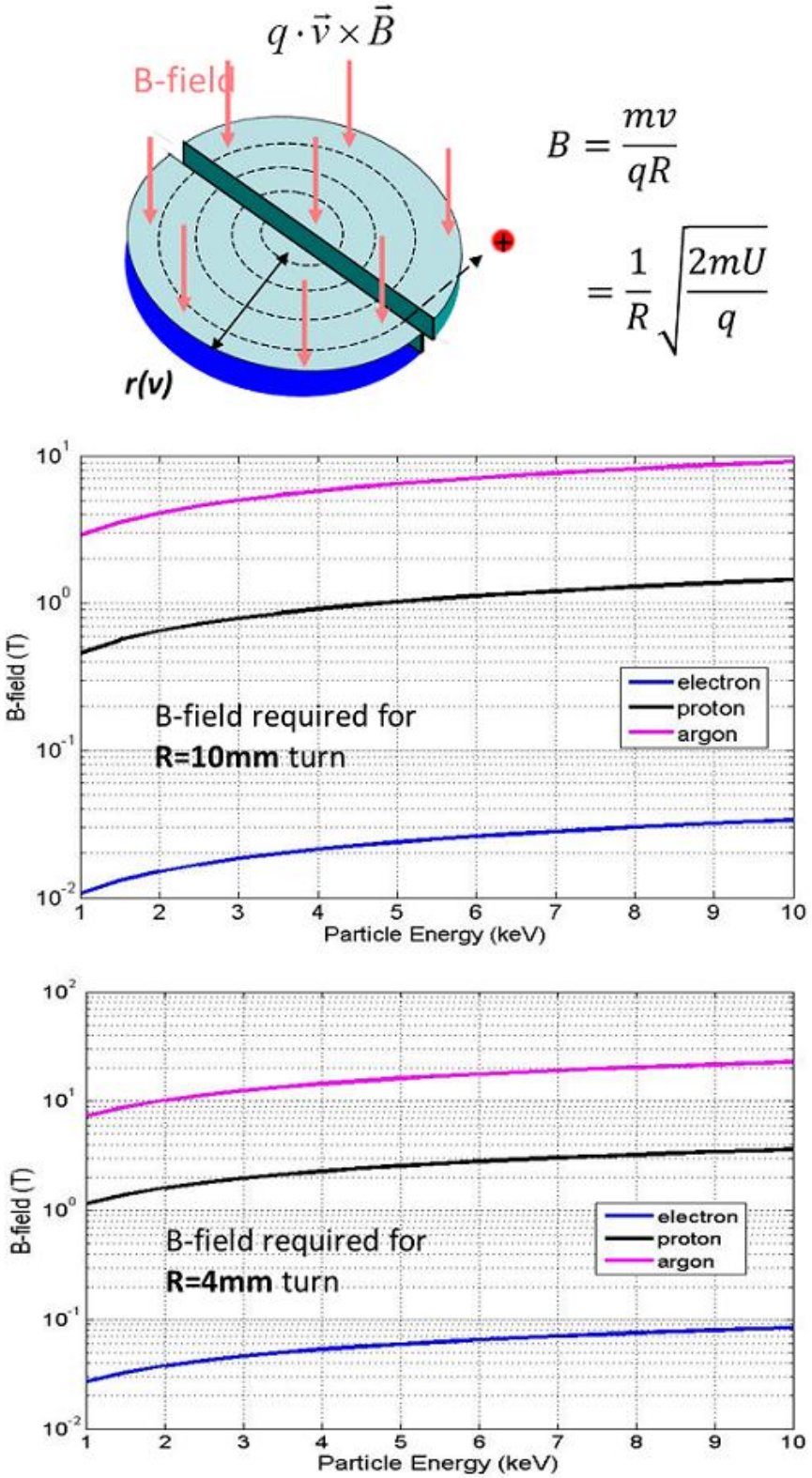

Figure 2.1 Charged particle curving by magnetic field for electrons, protons and argon in radii 10mm and 4mm.

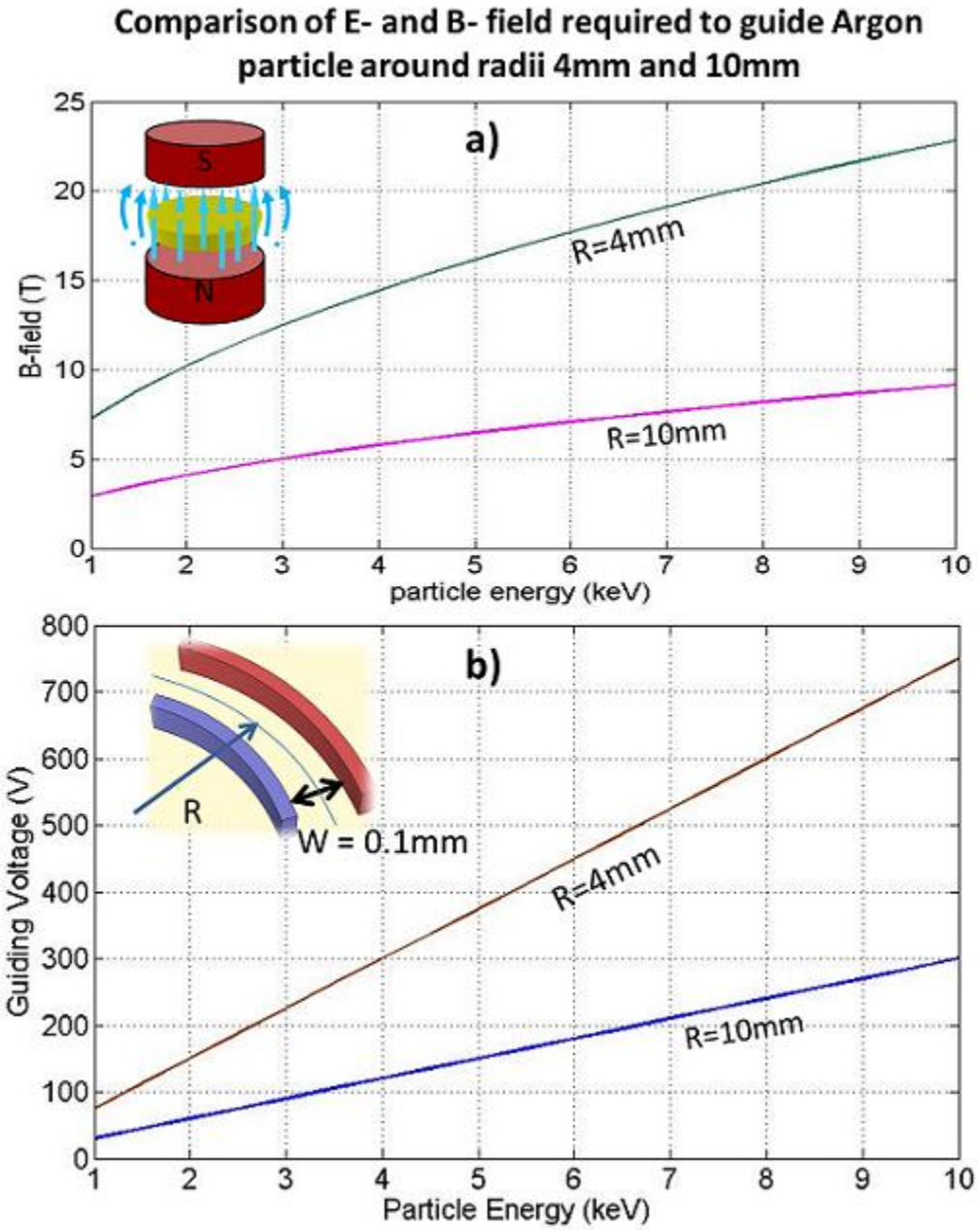

Figure 2.2 Comparing a) B-field strengths and b) guiding voltage, needed to confine an argon ion around a curvature of radii 10mm and 4mm, within ion energy range of 1-10keV

2.1.2. Theory & Design

Curved guidance occurs along a channel, of gap width *w*, defined by two electrodes between which is applied an electric potential V_{guide}. The radius of curvature at any point is given by *r* as shown in Figure 2.3a).

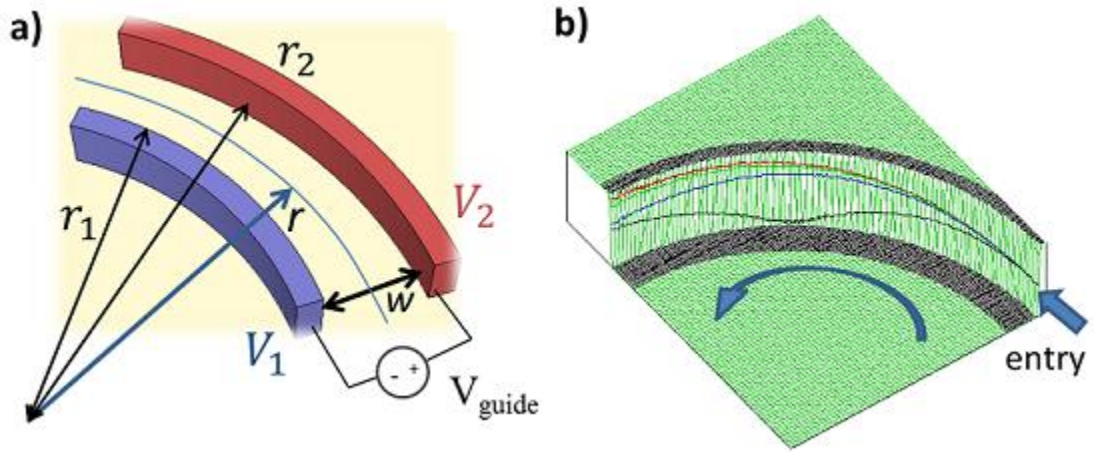

Figure 2.3 a) Illustration of a charged particle being guided around a curve radius *r* by the electric force provided by V_{guide} across gap *w* to compensate for the centripetal force required. Electrodes at positions r_1 and r_2 sustain potential V_1 and V_2 as shown. b) An example of 90° curve guide with particles tracks shown in topographically indicative of the potential landscape.

The curved guide on a planar substrate can be modeled as a concentric cylinders with the inner wall at r_1 and held at V_1, and r_2 held at V_2, so that the potential and electric field in the radial *r* direction in the gap are:

$$V(r) = V_1 + k\ln\left(\frac{r}{r_1}\right) \quad \text{where} \quad k = \frac{V_2 - V_1}{\ln\left(\frac{r_2}{r_1}\right)} \tag{2.1}$$

$$E_r = -\frac{dV(r)}{dr} = -\frac{V_2 - V_1}{\ln\left(\frac{r_2}{r_1}\right)}\frac{1}{r} \tag{2.2}$$

The equations of motion in the radial and azimuthal are:

Radial: $$\boldsymbol{m\ddot{r} - mr\dot{\theta}^2 = qE_r} \tag{2.3}$$

Azimuthal: $$\boldsymbol{\frac{1}{r}\frac{d}{dt}\left(mr^2\dot{\theta}\right) = 0}, \quad \text{or} \quad \boldsymbol{mr^2\dot{\theta}} = \text{const} \tag{2.4}$$

A non-relativistic charged particle is considered to be in an equilibrium orbit angular velocity if

$$\frac{mv_0^2}{r_e} = qE_e \quad \text{so} \quad r_e = \frac{mv_0^2}{qE_e} \tag{2.5}$$

$$\boldsymbol{\dot{\theta}_0^2 = \frac{qE_e}{mr_e}} \tag{2.6}$$

Now in the case of a stable orbit, the particle path may deviate by a small amount *x* from the equilibrium *r*, and still remain stable:

$$\boldsymbol{r(\theta) = r_e + x(\theta)}, \quad \text{where} \quad \boldsymbol{x \ll r_e} \tag{2.7}$$

Plugging this into equations of motion,

Azimuthal: $$\boldsymbol{\dot{\theta} = \dot{\theta}_0 \frac{r_e^2}{(r_e + x)^2} \approx \dot{\theta}_0\left(1 - 2\frac{x}{r_e}\right)} \tag{2.8}$$

Radial: $$\boldsymbol{\ddot{x} + 2\dot{\theta}_0^2 x = 0} \tag{2.9}$$

$$\boldsymbol{x = x_m sin\left[\sqrt{2}\dot{\theta}_0(t - t_0)\right] = x_m sin\left[\sqrt{2}(\theta - \theta_0)\right]} \tag{2.10}$$

Note, that *x* undergoes small oscillations only and does not grow in magnitude over time, and thus the orbit described is stable. The nodes of the oscillations in *x* are spaced when $\sqrt{2}\Delta\theta = \pi$, so that:

$$\boldsymbol{\Delta\theta = \frac{\pi}{\sqrt{2}} = 127°17'} \tag{2.11}$$

Simulations of particle tracks in stable orbits are shown in the next section: Figure 2.5 and Figure 2.6 demonstrate this $127°17'$ behavior. Hence first order focusing can be achieved for a nonrelativistic beam if the arc is subtended by $127°17'$ as is commonly described in cylindrical analyzers [27], [28]. Such an $127°17'$ arc for ion guidance is shown in Section 2.1.5.

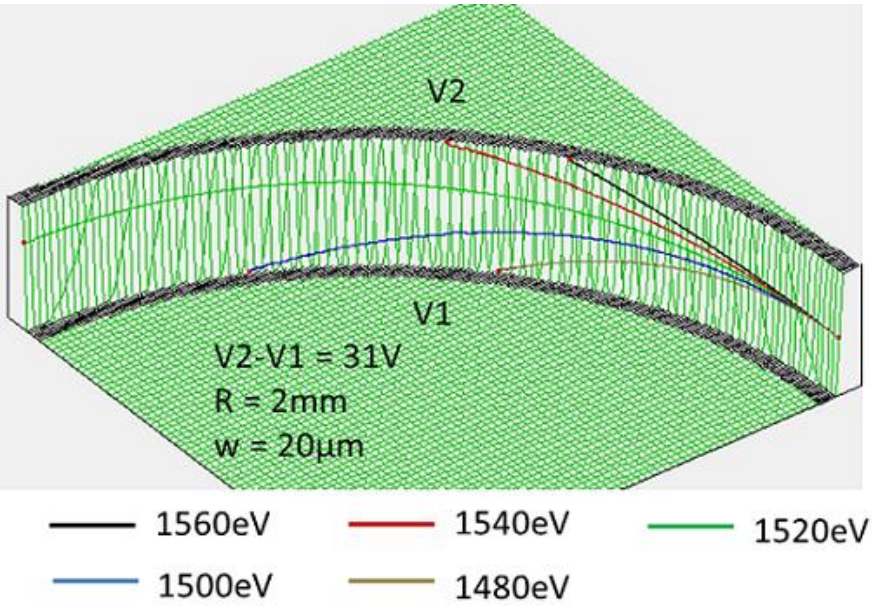

Figure 2.4 SIMION simulation of 90^0 curved guiding for 5 Ar^+ beams between 1.48 – 1.56 keV, starting from the right. The electric potential is represented topographically in green. Geometry is for radius of curvature 2mm; channel width 20µm with V_{guide} = 31V.

2.1.3. Simulations

Numerical solutions to curved guides are widely used as a more practical means of solving for the particle trajectories than analytical ones, especially considering fringe field response and aberrations. SIMION software solves the Maxwell equations in all simulation space for a configuration of electrodes with assigned voltages. Although it does not take into account space charge, SIMION is a good first order solver to provide an understanding of the actuated beam behavior.

Figure 2.4 shows an example of a SIMION simulation with the electrical potential lanscape topographically represented, and all particles starting at the same point, all entering the channel with zero tilt. This simple example illustrates the energy filter function of the curved structure. The figure indicates that particles of lower kinetic energy will follow a smaller curvature, and also suggests that the energy range of the particles allowed through the channel is proportional to the channel width. Hence, in terms of the curved structure's use as an energy analyzer, the energy resolution $\frac{\Delta E}{E}$ obtained is dependent upon the channel gap width *w* such that: $\frac{\Delta E}{E} \sim \frac{w}{r_e}$. In fact, bends of any degree of curvature can be used as an energy analyzer – the greater the angle the higher the selectivity: in Figure 2.5, if a 45° angle was chosen instead, the particle following the blue track would have been allowed to pass as well as the green track. This degree of energy selectivity or resolution is in addition to the dependence in width, and must be uniquely simulated for beams of differing emittance. In this light, electrostatic beam track solvers such as SIMION is crucial to charged particle actuator design.

Figure 2.5 illustrates that a particle will maintain its stable orbit around a ring despite small deviations x(θ) around the equilibrium orbit r_e as was described in Equations 2-.7 to 2-.11. The particle starts off in the middle of the channel, and at every 127.2° it refocuses as shown in Figure 2.5a). After more than 100,000 cycles the proton retains a stable orbit as shown in Figure 2.5b) with the tracks repeatedly overlapping each other. In the same guiding geometry and voltages, a particle with the same energy, but with slightly different initial conditions can also retain a stable orbit as shown in Figure 2.6. In this case, the starting position is *0.4* times the channel-width away from the exact middle of the channel, with an

initial deviation from the axis at that point (i.e. horizontal) of 0.05 radians. Again the refocusing effect after 127.2° of curvature is clear. For this starting position in this example, the maximum initial deviation angle allowed for a stable orbit is 0.07radians.

These two simple cases (Figure 2.5 and Figure 2.6) indicates that only particles with certain combinations of position and trajectory angle will retain stable orbits. This combination is described to be within an ellipse in phase space (see Section 3.1 for phase space explanations) for particles supported by the given electrode configuration. The particles outside the permitted ellipse will be lost to collisions with the side walls, and when fringe fields above and below the channel are taken in account, the restriction on the phase space ellipse becomes much greater. Simulations therefore are important tools to model the phase space of particles which are stable in any given experimental setup, and have been done so for the curved devices that will be described in later Sections 2.1.4 and 2.1.5.

The beam divergences due to space charges (self-fields) within the beam, can be compensated by focusing mechanisms like the electrostatic Einzel lens described in Chapter Three.

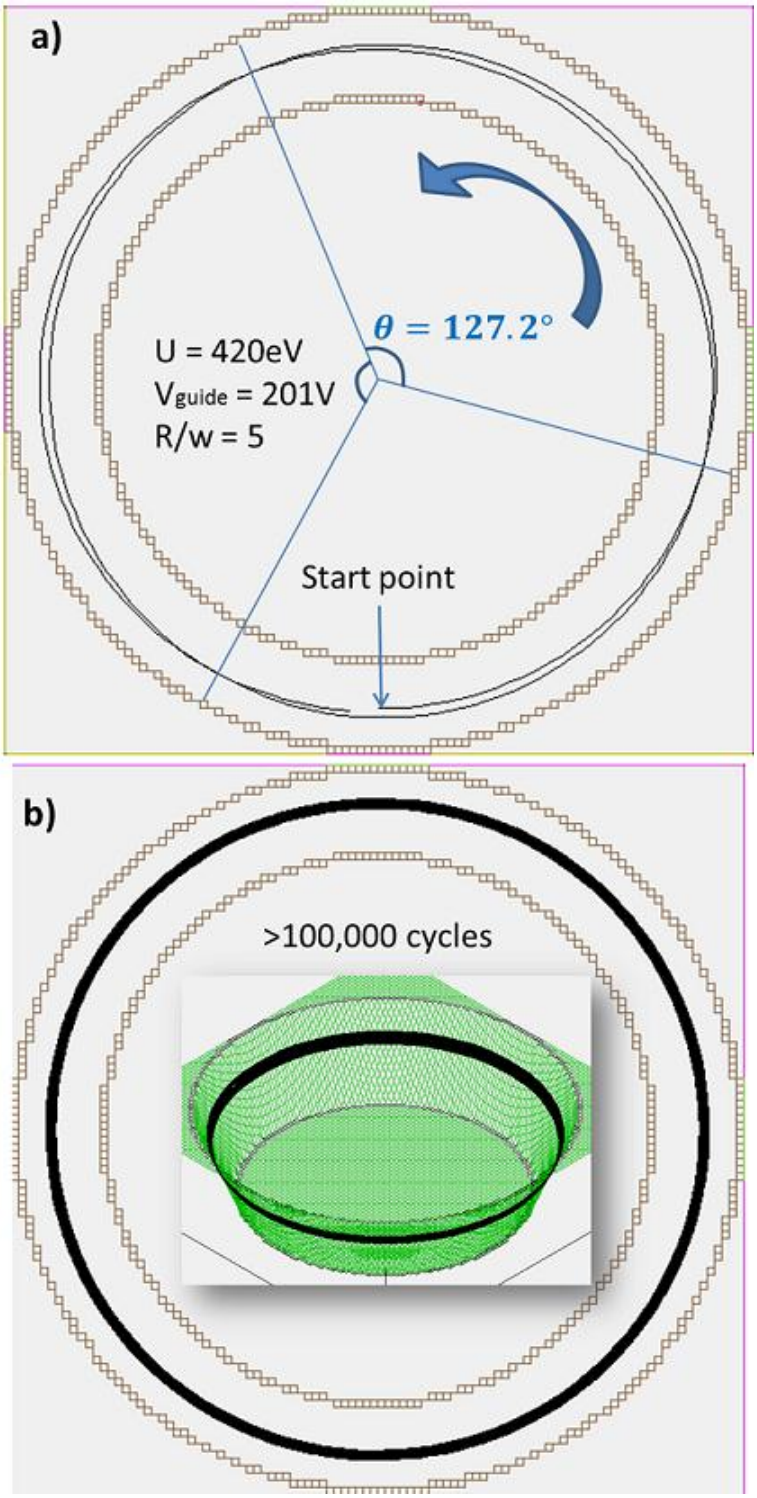

Figure 2.5 SIMION simulation of a 420eV proton guided in a circle at radius to width ratio of 5, with 201V applied across the guides. The particle motion is counter-clockwise. Initial position is mid-way between electrodes. Initial trajectory is along the ring axis. a) Top view of guiding geometry to scale after almost 2 cycles; b) Propagation path after >100,000 cycles in top view and potential topographical view.

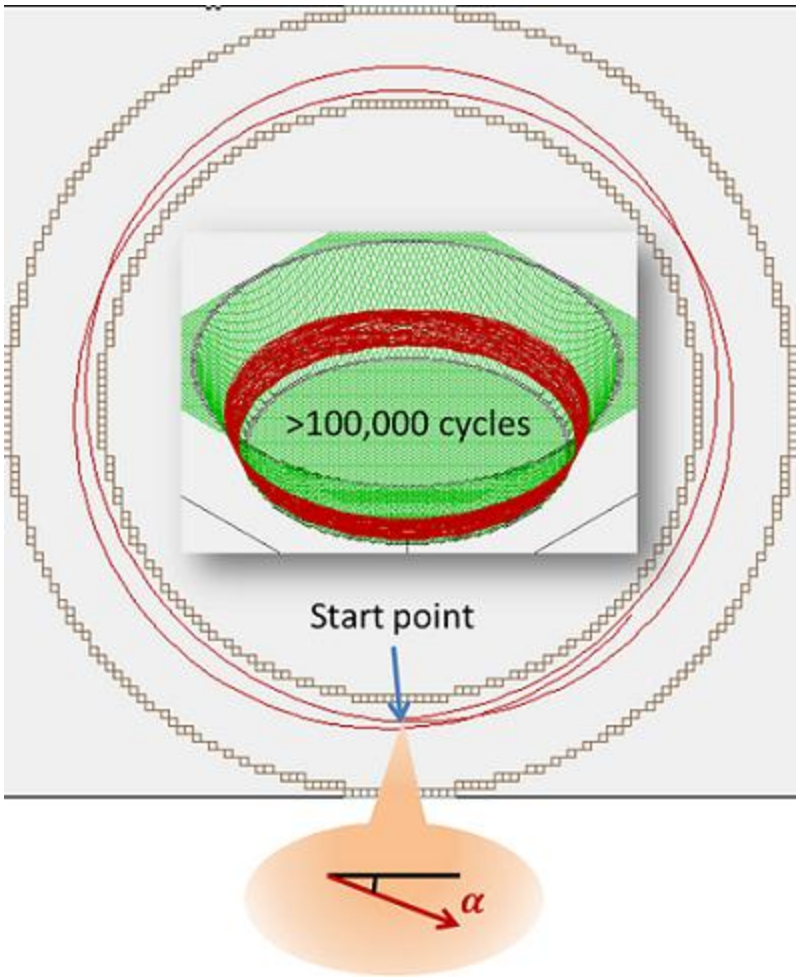

Figure 2.6 SIMION simulation of a 420eV proton as in Figure 2.5 starting at a point closer to the inner ring by 0.4*w*, where *w* is the width of the channel. At the start the particle also follows an initial angle $\alpha=0.05rad$ deviating from the central axis at that point. The particle motion is counter-clockwise. Outer ring shows the top view of the particle track after a little more than 2 full turns. Inset shows the track in topographical view after >100,000 cycles.

Curved guidance channels were implemented both on SOI and PCB. In the SOI case the channels were defined by the doped Si layer. In the PCB case, the electrodes are defined by the copper layer on top of the FR4 dielectric. The methods of fabrication and testing will be discussed with the corresponding results.

2.1.4. SOI Implementation: Fabrication, Testing and Ion Guidance Results

Curved structures were first fabricated on silicon-on-insulator (SOI) wafers, as traditional microfabrication techniques could be utilized achieve micron size channel gaps. Several processes were attempted with differing results. Figure 2.7 shows such a fabrication process resulting in electrically isolated doped silicon electrodes, the top of which is covered with oxide. In discussing the process flow below, additional processes will also be mentioned pointing out the various issues that were met.

The process flow in Figure 2.7 results in a SOI chip with patterned device layer which defines the conductive guiding channels and electric connections. The structures are accessed electrically via Al+1%Si pads (henceforth called Al pads for short) in certain designated regions, by wire-bonding to off-chip pins on the chip carrier package as shown in a photo of an example of such an SOI chip in Figure 2.8. The Al pads' positions are designated to be as far removed as possible from the guiding channels to ensure the signals supplied to the electrodes do not influence and are not influenced by the ion beam. In addition the pads are used to make an electrical connection between two electrodes that are partitioned by another structure – this method of overstepping electrodes is in place of conducting vias which would require more complicated and time-consuming fabrication processes. In using wire-bonding connections on the chip, care must be given to their positioning so that they are not in the direct path of the main actuated beam. On top of all the Si electrodes, a layer of oxide is deposited to insulate the electrodes from extraneous charged particles that is not the main beam itself. The side walls of the Si guiding channels should be clear of oxide. SEM images of examples of resulting structures are shown in Figure 2.10 to Figure 2.12.

The process begins with an SOI wafer with the highly doped device layer chosen to have resistivity down to 0.001 – 0.005Ω-cm with thicknesses of 20 μm and above. The amount of doping is inversely proportional to the thickness of the device layer. In step 1, a >600nm layer of aluminum plus 1% silicon (Al+1%Si) is sputtered onto the Si, and is then patterned by photo-lithography and wet-etching (steps 1-2). 914 nm of Al can be wet-etched in 3.5min at 65°C.

The photolithography process involves the use of the i-Line series of resist *SPR 220 4.5* and/or *SPR 220 7.0* [29]. For example, by spinning *SPR 220 4.5* at 3000rpm for 30sec, a 4 μm thick layer was achieved. Using the *EV620 Contact Aligner* [30] in soft contact mode, the exposure time for *SPR 220 4.5* is 6.5sec, and that for *SPR 220 7.0* is 14sec. Post-exposure baking of the resist at 115°C for 150 sec is required after a holding time of >30min. *AZ 300 MIF* or *AZ 726 MIF* are used to develop the photoresists [31]. The photoresists is stripped by dipping in acetone for 10min, followed by washing with isopropanol and de-ionized water. This chemical combination is highly recommended rather than photoresist removers, namely the *Microposit Remover 1165* from *Shipley* [32], since the *1165* will etch the Al layer as well.

After the Al & 1%Si layer is patterned, the photoresist is stripped and the metal is annealed at 400°C for 60min in 5% N_2/H_2 gas, to realize good Ohmic contact between metal and silicon.

In step 3, an oxide layer is deposited by plasma enhanced chemical vapor deposition (PECVD) for an estimated 1-2μm thickness at a deposition rate of 0.117 μm/min (with rate may be variable). The oxide is patterned by etching in dry CH_3/Ar plasma at an approximate

rate of 37nm/min. The oxide/photoresist selectivity of this etch is about 1.7. This deposited oxide layer only exists on top of the doped silicon, and not on the sidewalls. Its purpose is to shield the electrodes during device testing from extraneous ions in the vicinity immediately above the electrodes, to minimize noise and signal artifacts. The oxide layer does not cover the Al pads. Devices without this oxide layer was also fabricated, which reduced the number of processing steps.

In step 4, the device layer Si is etched by the deep reactive ion etch (DRIE) process. For this DRIE, a patterned layer of photoresist is added to protect the oxide and cover the Al which should not be exposed to the etching plasma. The thickness of the resist must be in proportion to the thickness of Si being etched. For through-wafer etches, a 7 μm thick resist is recommended. Using the *Unaxis 770 Deep Si Etcher* tool [30], the Si etch rate was characterized to be around 0.4 μm/cycle, but may vary from time to time. The SEM image of a DRIE processed channel in Figure 2.13 shows a sidewall surface roughness of less than 0.5 μm, and a very clean substrate. One disadvantage of DRIE is the cost associated with the approximately 5hours of etching time that is needed. Another disadvantage is that hard to remove black polymers are sometimes deposited during the etch, after which no further etching of Si can be done. The deposition may be a result of an unclean chamber that is shared with other users.

In step 5, the resist is removed and is adhered to a commercially available gold-coated chip package. The Al pads are then wire-bonded to the pins on the package, through which they are electrically addressed, as is shown in the photo of Figure 2.8. The entire package is mounted on an x-y-z-stage in the vacuum chamber with wiring connected to the package pins as shown in the photo of Figure 2.9.

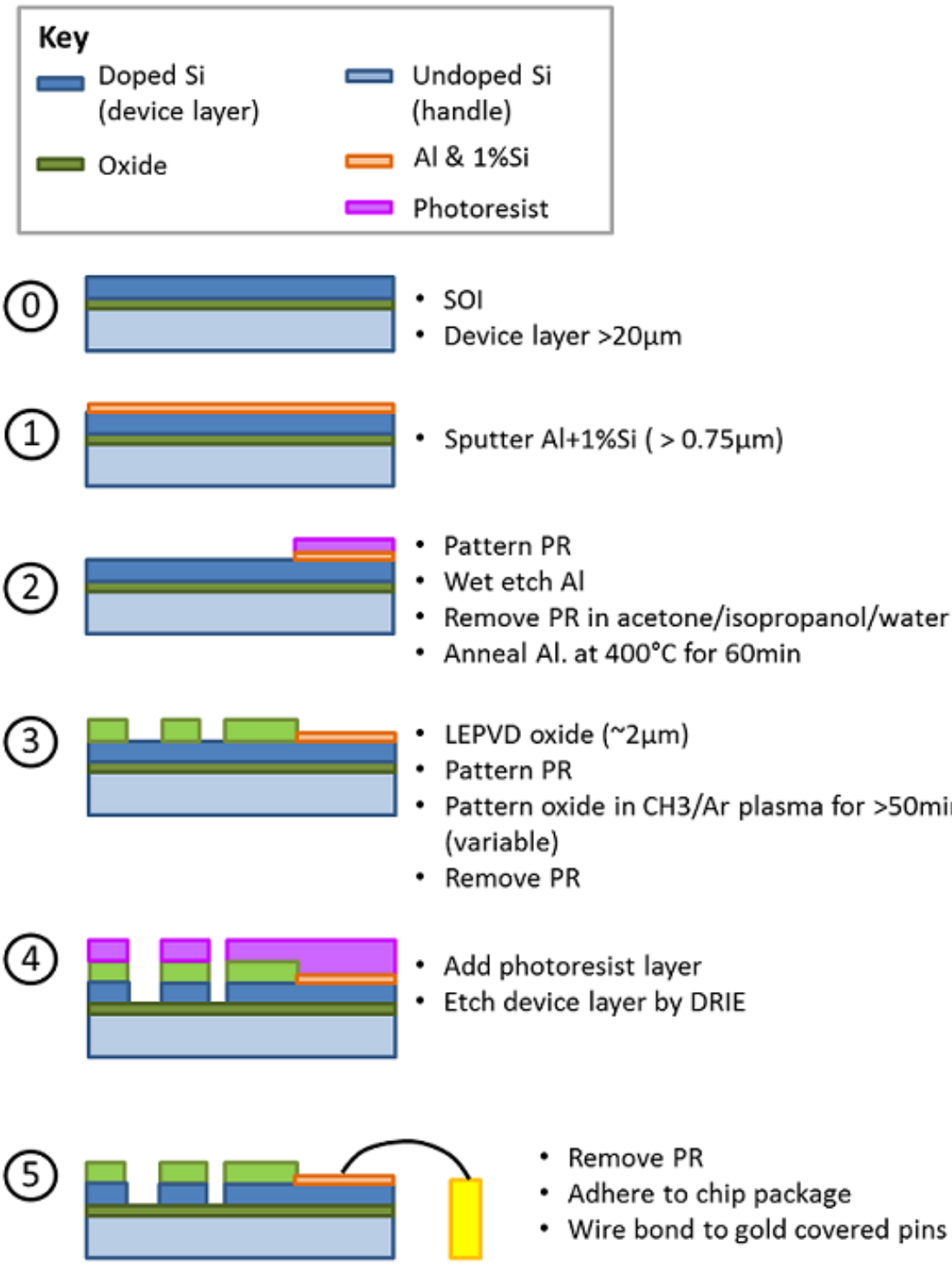

Figure 2.7 Fabrication process on the silicon-on-insulator wafer platforms. The device layer of a SOI wafer was patterned to define the guidance channels. A layer of Al + 1% Si on certain parts of the Si provide bonding pads. The rest is covered with oxide to shield electrode from extraneous charged particles in space immediately above the device. The entire chip sits on atop a chip package with gold covered pins to which the Al pads are wirebonded to.

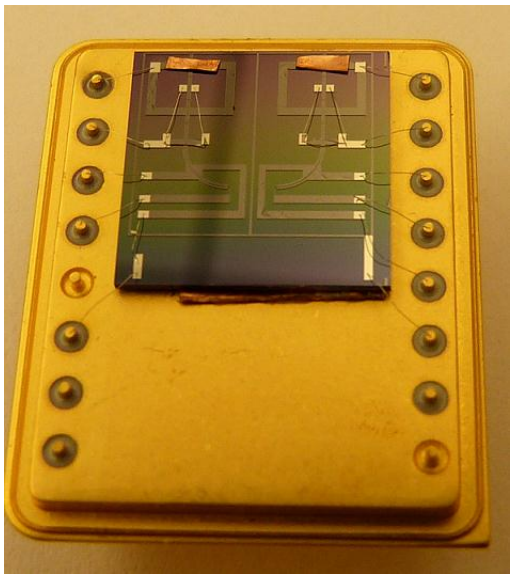

Figure 2.8 Photo of an example of a final SOI- implemented device on a gold-coated chip package. Al square pads are wire-bonded to the round pins along the sides of the package. The The Al pads can also be used to connect different regions of the chip via wire-bonding.

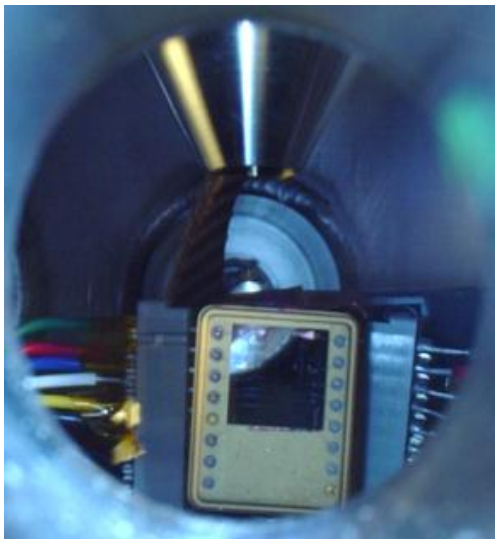

Figure 2.9 View of the mounted chip in vacuum chamber through aglass viewing port. The chip and package from Figure 2.8 is mounted to a holder and x-y-z stage. Connectors to the package pins allows for electrical wiring which exits through the chamber via feedthroughs. The ion gun nozzle is seen at the top of the photo, with the beam propagating vertically downwards.

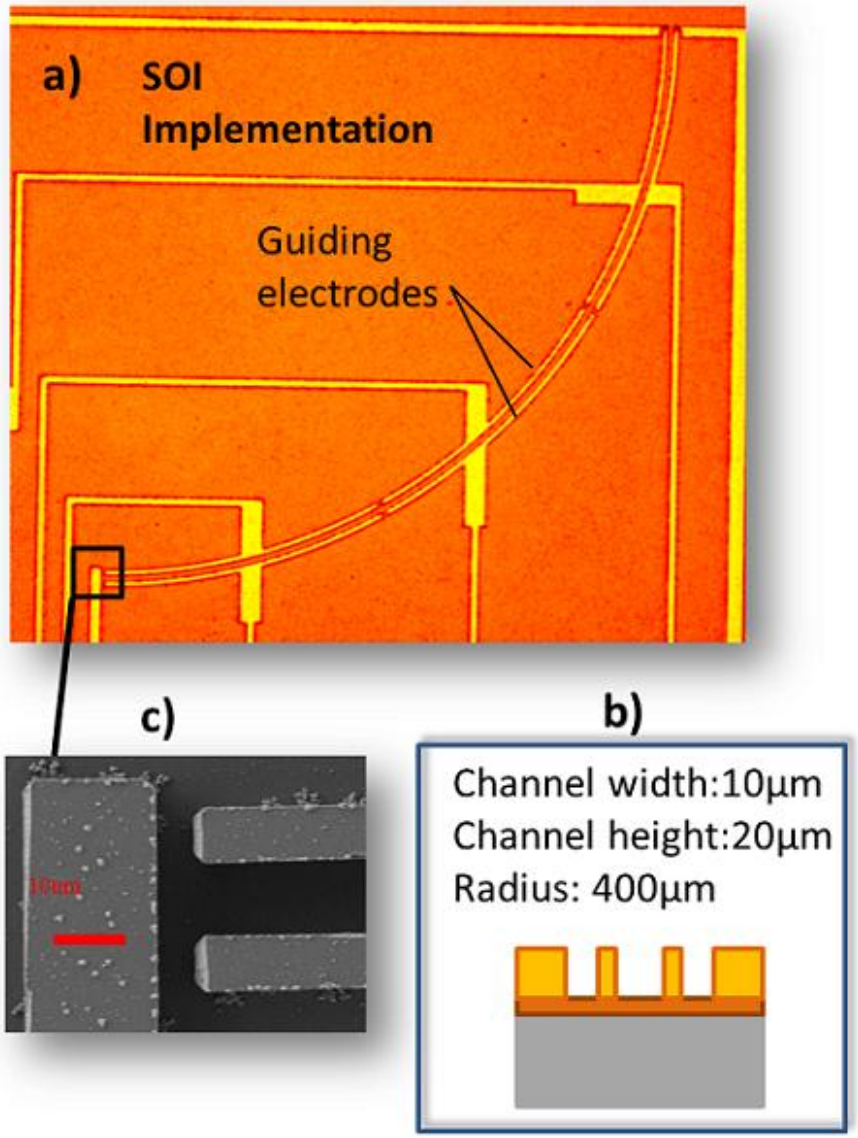

Figure 2.10 First 90° curved fabricated on SOI in a) photo top view; b) side view illustration of the channel with radius of curvature 400 µm, height 20 µm and width 10 µm; c) SEM image of the end electrode located at the channel terminal to detect guided particles.

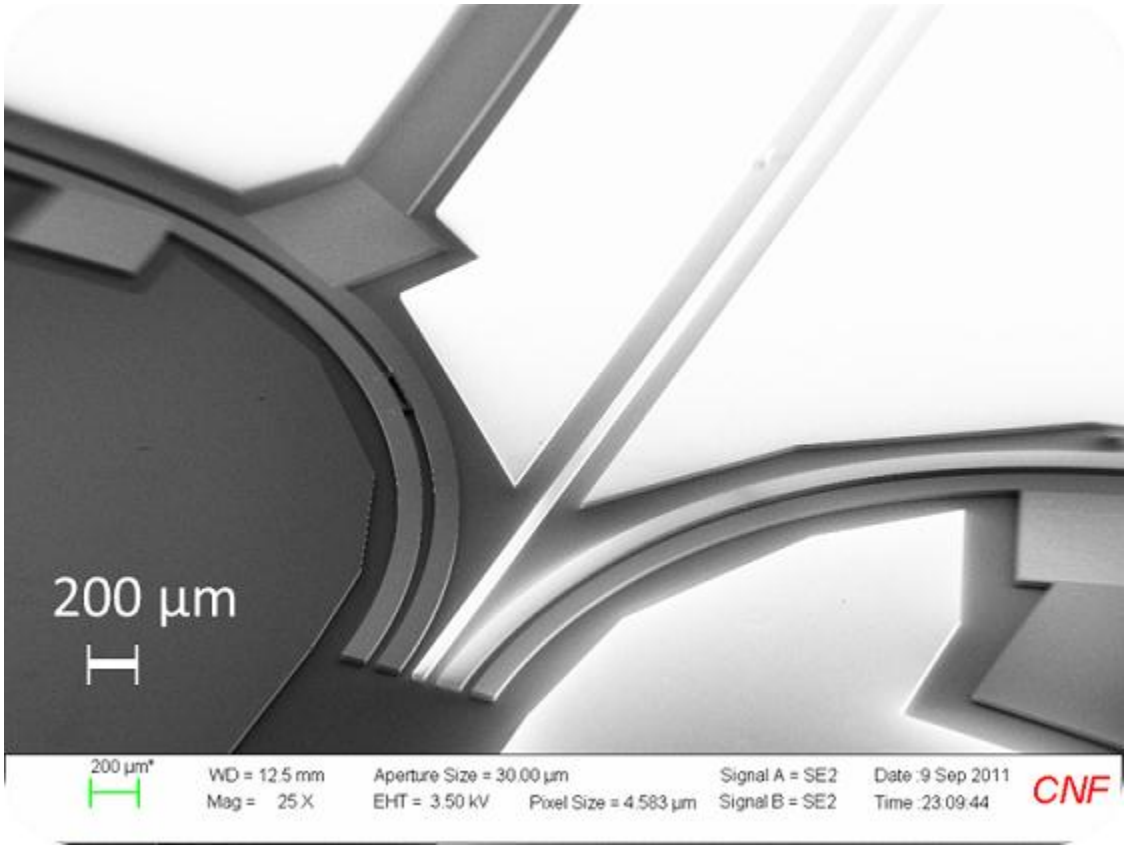

Figure 2.11 SEM photo of two curved guides of the SOI implementation. The straight electrode in the middle is used for alignment of the ion beam. A clean current signal results when the beam directly impinges onto the straight alignment electrode. Then, the beam can be shifted a known distance across to the opening of the guiding channels in close proximity to it, as shown.

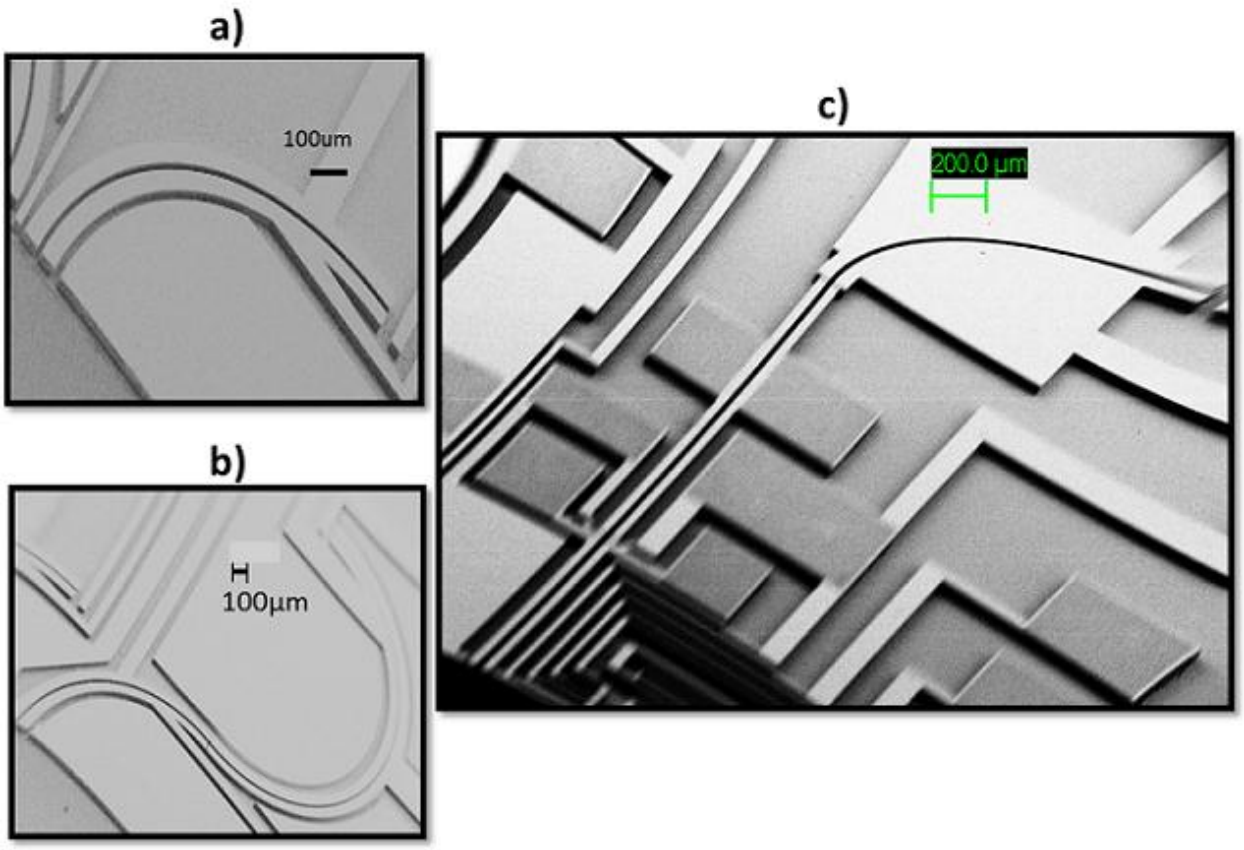

Figure 2.12 SEM images of more examples of fabricated SOI structures: a) a 90° curve; b) a 270° "spoon" shaped curve; c) a linear accelerating section followed by a 90° curve. In all cases the beam enters from the bottom left corner of the image.

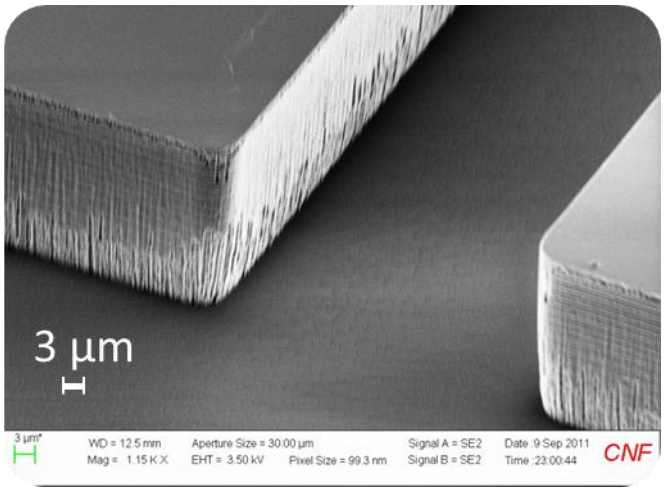

Figure 2.13 SEM image of the side wall roughness of Si after DRIE.

One of the first chips that was tested is shown in Figure 2.10 with a 10 µm gap channel width and side wall height of 20 µm. The 90° curve of radius 400 µm is defined by 3 segment pairs to garner greater flexibility in electrical control. However for all experiments all the outer curve electrodes are at the same voltage, and likewise for the inner guides.

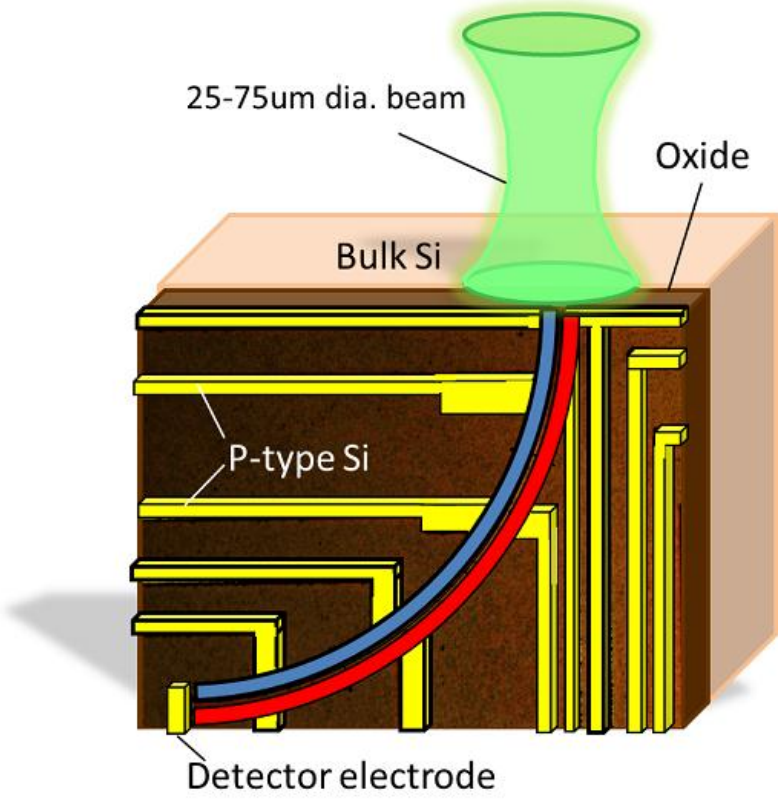

Figure 2.14 Schematic of experimental test for 90° guiding of Ar^+ ions. The ion beam is scanned across the top lip of the chip. When the beam enters the curved channel (defined by electrodes in blue and red), and is guided correctly, it will be detected by the detector electrode at the end of the curve, as a current signal.

Figure **2.14** illustrates the testing of the SOI guiding structures using a commercial ion gun (Chapter 4) as the beam source. The Ar^+ ion beam is scanned across the top edge of the SOI chip. Only if the particles enter the guiding channel *and* is also corrected guided, will they be

detected as a current signal by the end detector electrode at the end of the channel. As the positive ions impact the detector electrode, they are neutralized by negative electrons that must be pulled from the electrode. A continuous ion beam will require a continuous negative current through the electrode, which is connected directly to the Keithley 2400 SourceMeter [33] to measure current signals down to pico-amps. For the beam to be guided, the voltage across the curved electrodes, V_{guide}, must match the value from simulation for this geometry and beam energy. In a first order approximation, the particle energy U is related to V_{guide} by $U = \frac{R}{2w} V_{guide}$, however the simulation results should be relied upon. This method of scanning not only solves the issue of beam alignment into the channel, also demonstrates ion guidance. A background current signal scan is taken first with $V_{guide} = 0$, and is then subtracted from the current signal detected when $V_{guide} \neq 0$ or when V_{guide} is assigned the value predicted by simulation. The background subtraction ensures that other detection artifacts are ignored, and only the signal due to the beam guidance by the bent channel is differentiated. An example of a detection artifact occurs when the beam is positioned directly above the detector and does not pass through the bending channel, and therefore is independent of V_{guide}. Background subtraction is thus critical.

For the device shown in Figure 2.10, let the horizontal direction across the chip edge by called "x", and the orthogonal direction (into the page) be named "y". Hence "x" and "y" defines the plane perpendicular to the beam's direction of propagation, and are controlled by the deflectors within the ion gun optics. The background-subtracted current signal data is plotted as a function of "x", at a fixed "y" position, in Figure 2.15. The clear peak indicates that the 2keV Ar^+ ion beam is successfully guided around the 400 μm radius of curvature between electrodes 10 μm apart and supporting a V_{guide} of 40.11V. In addition, considering the particle beam

width itself is about 75 µm, the peak width of 80 µm is not unreasonable.

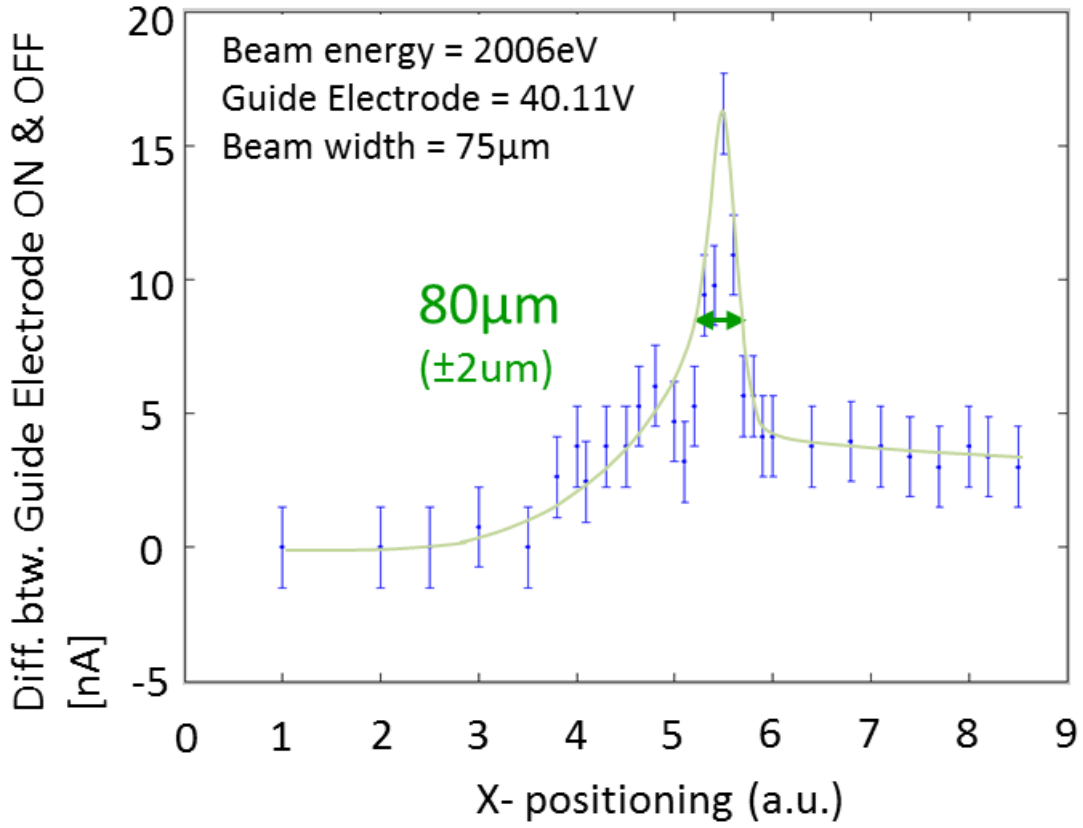

Figure 2.15 Current signal data as a function of particle beam scan position arbitrarily named "x" which is controlled by beam deflectors inside the ion gun optics. Data plotted is the signal difference between the cases for which the guides are on, and that for which the guides are off.

The curved structure can act as an energy analyzer or particle energy filter since the particles with energy U that are allowed through the channel is directly dependent on the voltage across the channel V_{guide}, for a given guide geometry:

$$U \propto V_{guide}$$

Hence, given a beam with a fixed energy distribution, the sweep of V_{guide} should be indicative of that energy distribution. Figure 2.16 shows the current signal detected as described above, for a beam of average energy of 2keV, through a 127.5° curve. The current signal is again background subtracted. The peak corresponds well with simulation result of 86V for this

geometry. The 127.5° angle of curvature was chosen for its first order focusing effect, mentioned theoretically in Section 2.1.2, with simulation examples in Section 2.1.3. The aspect ratio of the channel height to width is 2, which adversely affect the beam intensity detected, as well as the signal-to-noise ratio (SNR). For such low aspect ratio, one expects much of the particle beam to be lost by fringing fields.

Despite these drawbacks, that the predicted peak is nonetheless detectable, is promising as a proof of principle and lays a foundation for future optimization.

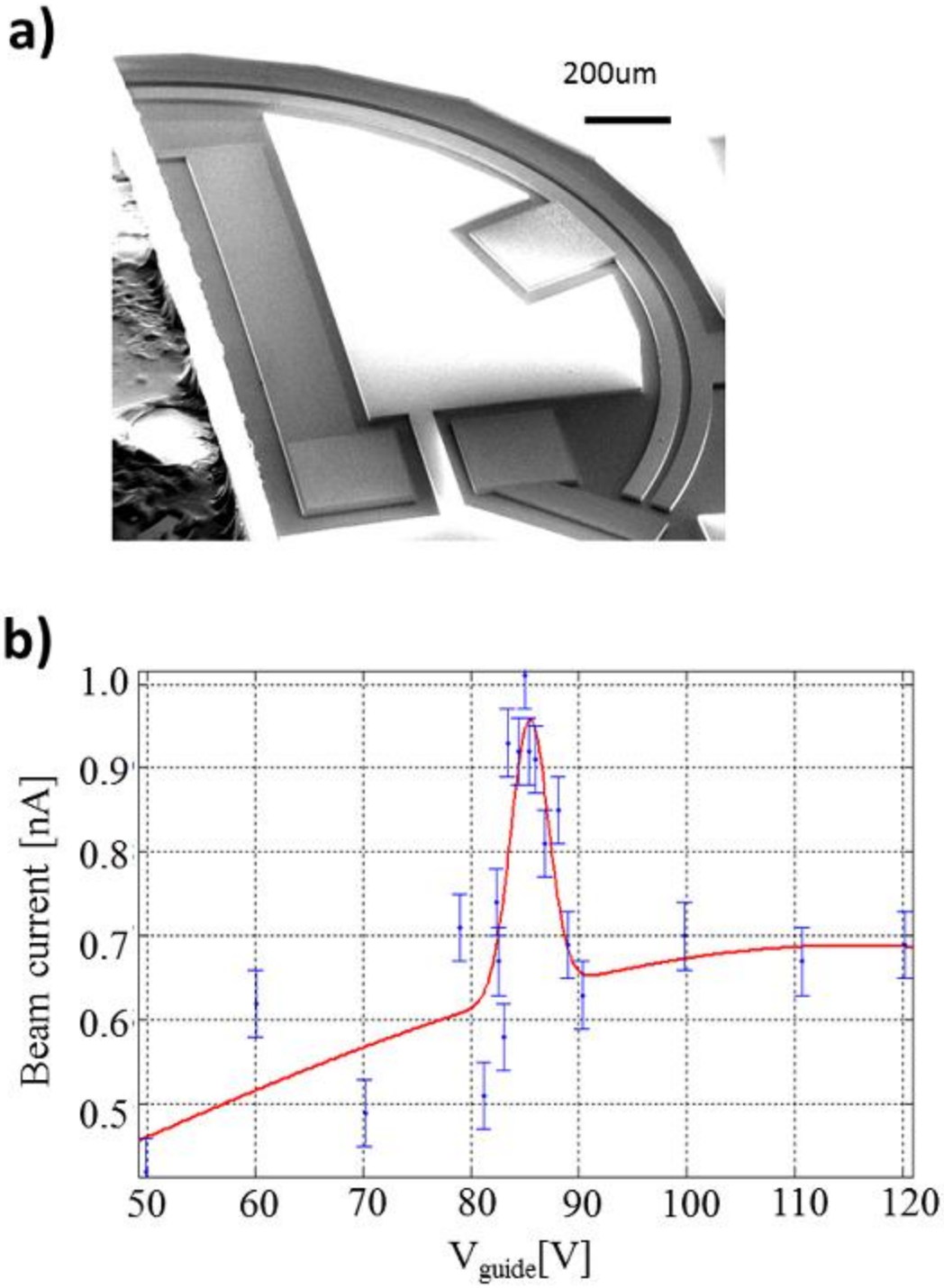

Figure 2.16 a) SEM image of a 127.5° curve guide with channel width 50µm, channel height 100µm, and radius of curvature 2.5mm on SOI. b) For a fixed beam energy, the guide potential difference V_{guide} is swept over a 70V range and the beam current signal (absolute values) from the detector electrode is plotted in blue. The red line is simply to mark the peak position. Data plotted is background subtracted.

2.1.5. PCB Implementation: Device Testing and Results

The microfabrication process is costly, often with a low turn-over rate. Printed circuit board (PCB) processing, on the other hand, can be produced commercially, cutting down the cost by more than 50% and reduce the production time to almost a tenth of the microfabrication processing time. Hence some effort were made into patterning the copper layer on PCB to act as the guiding structures, even though commercially the aspect ratio of such copper channels is $\frac{height}{width} = 0.44$.

Figure 2.17 shows an image of such a PCB device, with the method of testing. The ion beam is scanned in the plane "x-y" perpendicular to the chip substrate plane, as was the case for the SOI case. The scanning is achieved by rastering the movement of the sample on a motorized stage in "x" and "y", keeping the beam fixed in position. Detected current signal on the electrodes over "x" and "y" can be plotted as shown in the figure. For alignment purposes, an electrode extending to the beam-scanned edge of the device, is first located as shown in the clean signal in Figure 2.17A. Then the sample is moved a known distance so that the beam is then in close proximity to the orifice of the desired curved channel at point **B**. A small area around this approximated point can be then scanned quickly by observing the current signal on the detector electrode at the end of the curve. Figure 2.17B shows that detected signal over an "x" and "y" region. After subtracting for the case when $V_{guide} = 0$, there is a clear localized peaking signal.

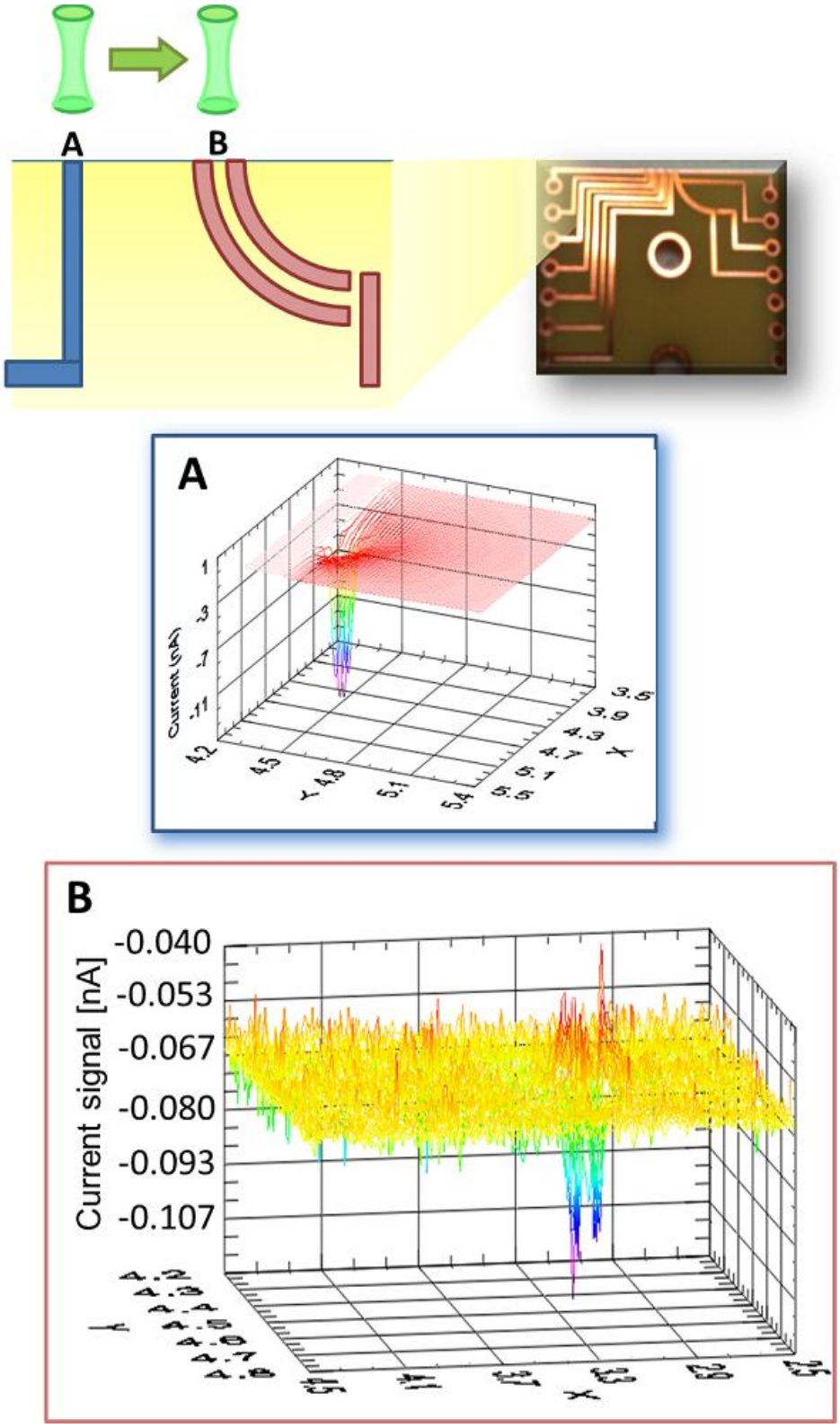

Figure 2.17 TOP: testing methodology of curved ion guide on PCB. The beam is first scans for alignment electrode at position 'A', with associated current signal shown in **A**. Then the beam is moved a known distance to position 'B', resulting in a guided signal shown in **B**.

In Figure 2.17B one notes that around the signal dip in blue/purple (which is the ion beam signal), there are red/orange signal peaks above noise. This may be attributed to the secondary electrons which are generated when the ion beam impinge upon the guide walls, just before the ions are positioned correctly to enter the channel. Some of the secondaries can then be guided to the detector electrode, while there is still no guidance of ions. Negative electrons will induce a current signal of the opposite polarity to positive ions. When the full ion beam enters the channel the signal quickly reverses to indicate successful positive ion guidance. This measurement artifact cannot be subtracted with background because similar to the ions, the secondary electrons in question will not be guided when $V_{guide} = 0$.

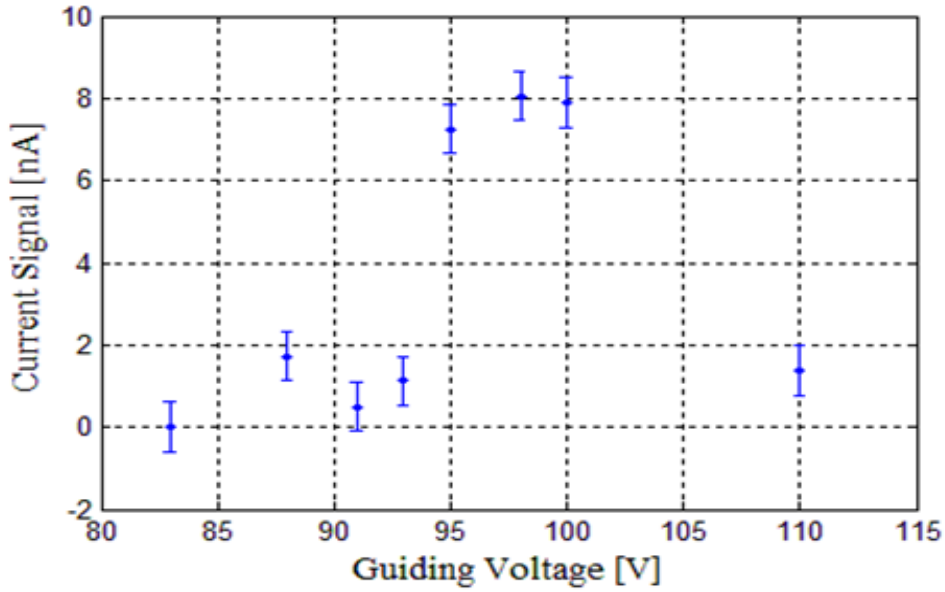

Figure 2.18 Variation of current signal on the detector electrode on PCB, as a function of the guiding voltage V_{guide}. Data is background subtracted.

Just as for the SOI implementation, the energy distribution for a fixed beam can be represented by a sweep with V_{guide}, shown in Figure 2.18. For the given geometry, simulations predict a peak centered around $V_{guide} = 98.11V$, with a spread in the range 92V to104V given

the energy distribution of the ion beam from the source. The distribution in the above figure is reasonable given the simulation results, and hence it is shown that curved guidance is successful even in low aspect ratio channel structures, albeit with low SNR.

2.1.6. Future Directions and Possible Applications

One of the main concerns for the SOI and PCB implementation of charged beam manipulators is the low aspect ratio, and the limitation to one or two layers of structures. In Chapter 3, a process involving the micromachining of bulk silicon wafer will be described, which does not require costly SOI wafers. Each silicon layer can be >500μm and can be stacked to achieve a high aspect ratio. In addition, the channel width can increased to accommodate a higher beam flux, resulting in stronger current signal and higher SNR.

Simulations of a guide channel with walls consisting of 3 layers are shown in Figure 2.19. In this example, the layers are separated from each other by gaps that are 20% the thickness of the conducting layers themselves. This large gap size is responsible for the beam losses shown (without considering fringing fields outside the channel). However following the fabrication process that was developed in Chapter 4, the gap between silicon layers are the oxide layers which is about 4 μm, or 0.8% of the conductor layer. Thus particle loss due to non-conductive gaps is minimal.

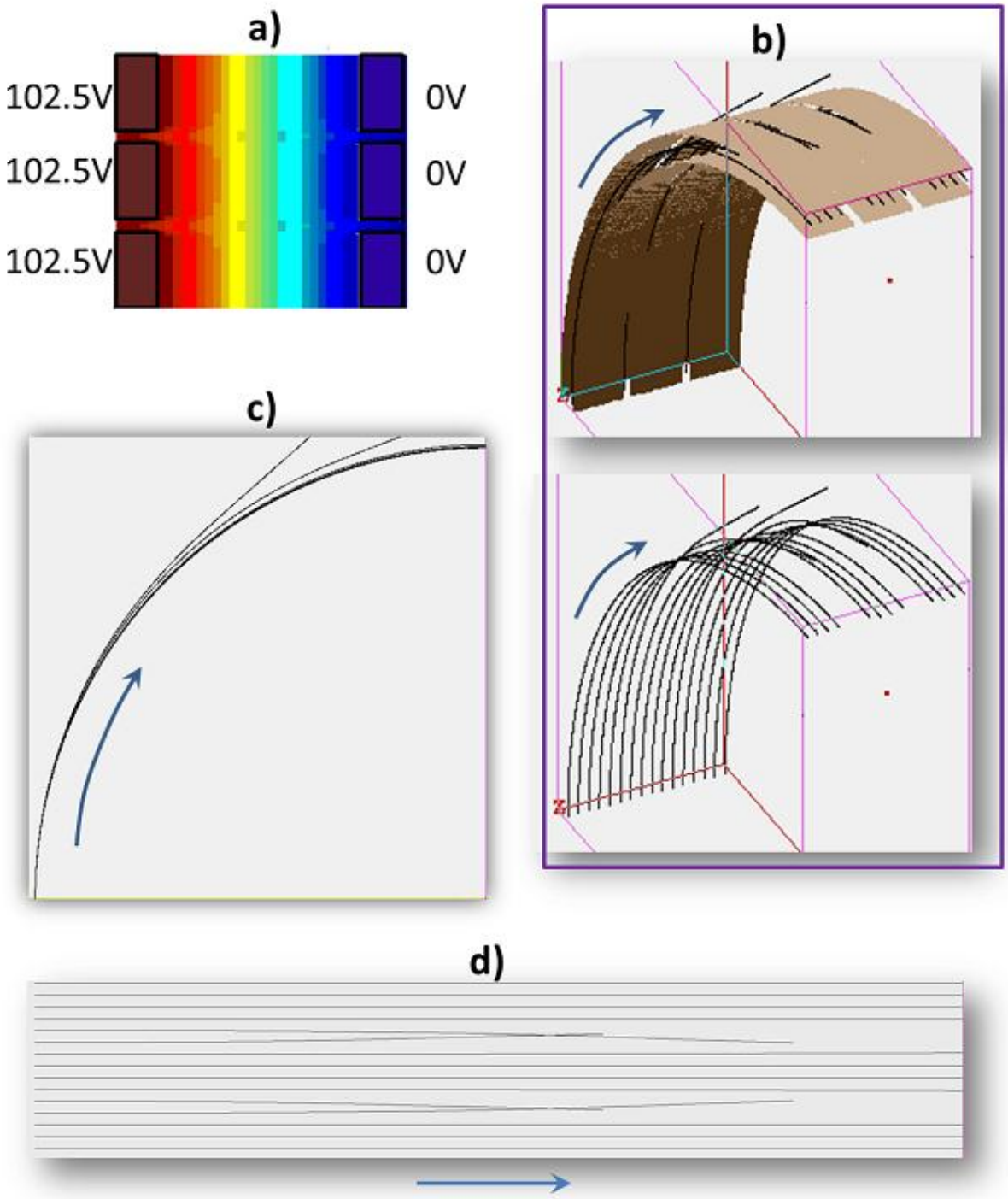

Figure 2.19 Simulations of a three layer sidewall electrode architecture: a) cross-sectional view into the channel such that a beam will travel into the page, with the COMSOL simulated electric potential intensity represented in color. b) electrode geometry in SIMION in 3D: TOP - three electrode layers are seperated by gaps that is a fifth of one layer thickness; BOTTOM - trajectories of the particles shown in 3D view. c) Top view of tracks of guided particles (guides invisible). d) Side view of the particle tracks propagaing from the left.

The ability to fabricate multilayered channel structures will also add the benefit of focusing out-of-plane, when the layers are electrically insulated from the others. Figure 2.20 shows the potential in the channel cross-section when the 3 layers of the two side walls can be addressed individually. The potential gradients in the channel space engender forces which acts perpendicular to the beam's direction of propagation, with vertical components that push particles towards the center of the channel as illustrated in Figure 2.21. In the figure, the simulated results show that such 3-layer curved guides can simultaneously focus *and* guide ion beams. Hence with the multi-layer conductive silicon fabrication process developed, implementation of out-of-plane focusing is made possible

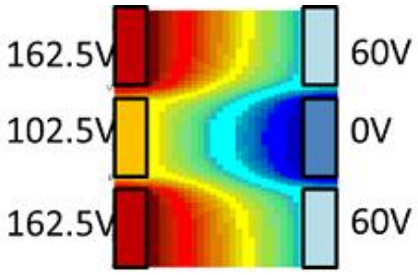

Figure 2.20 COMSOL simulation of potential inside a channel cross-section for electrodes in each layer being individually addressed.

As mentioned before, a curved channel with a potential applied in between can be used as an energy analyzer with the energy resolution dependent upon the channel width and the radius of curvature. If time-of-flight or magnetic actuation accompany the electrostatic actuation, the mass of the ion species could be determined as well. Recent years saw a drive towards miniaturizing mass spectrometers as a means to enhance their portability for fast, location-specific testing [34]. Commercially available hand-held spectrometers can weigh above 4kg [35] [36]. Micro-machined curved channels could reduce the cost and size of mass spectrometers if integrated with microelectronics, resulting in a spectrometer which can

fit into one's pocket.

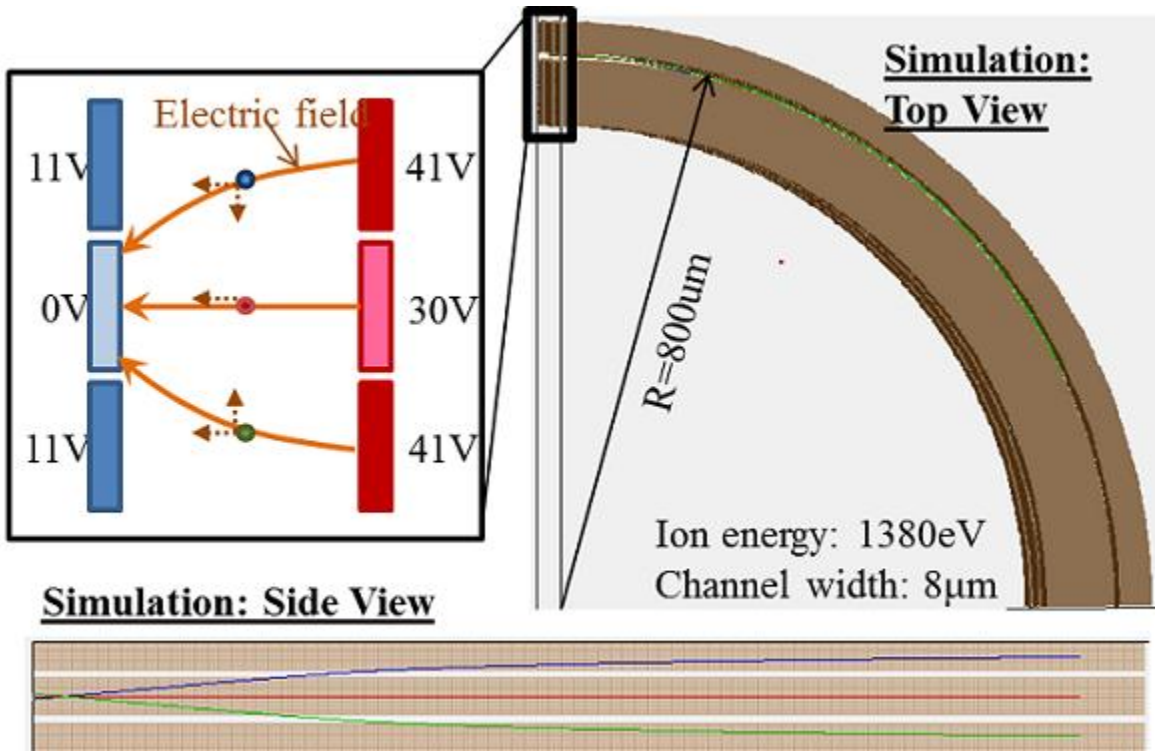

Figure 2.21 Simulation of out-of-plane focusing of ion beams by a 90° curve consisting of 3 layered side walls. Schematic of the electric field within channel cross-section is shown in inset. Side view of simulated particle trajectory propagating from right to left is shown at the bottom.

The demonstrated ability to maneuver charged particles in a circular path is the main method to reduce the size of charged particle accelerators without requiring the application of high voltages. Acceleration in turn, drives the particles to energy ranges for targeted applications, for which there are many below a couple of MeV. Figure 2.22 shows the radius of curvature that can be achieved by applying guiding voltages, for various particle beam energies below 2MeV. For applications involving relatively low energies (<100keV) such as the SEM (scanning electron microscopy), FIB (focused ion beams), and LIGA (lithography electroplating and molding), the actuating systems could in theory fit onto a 4" wafer, supported by 100V – 300V guiding voltages. Applications requiring >1MeV energy beams such as for PET (positron

emission tomography [37]) and PIXE (particle-induced x-ray emission), a suitcase-sized system would be possible.

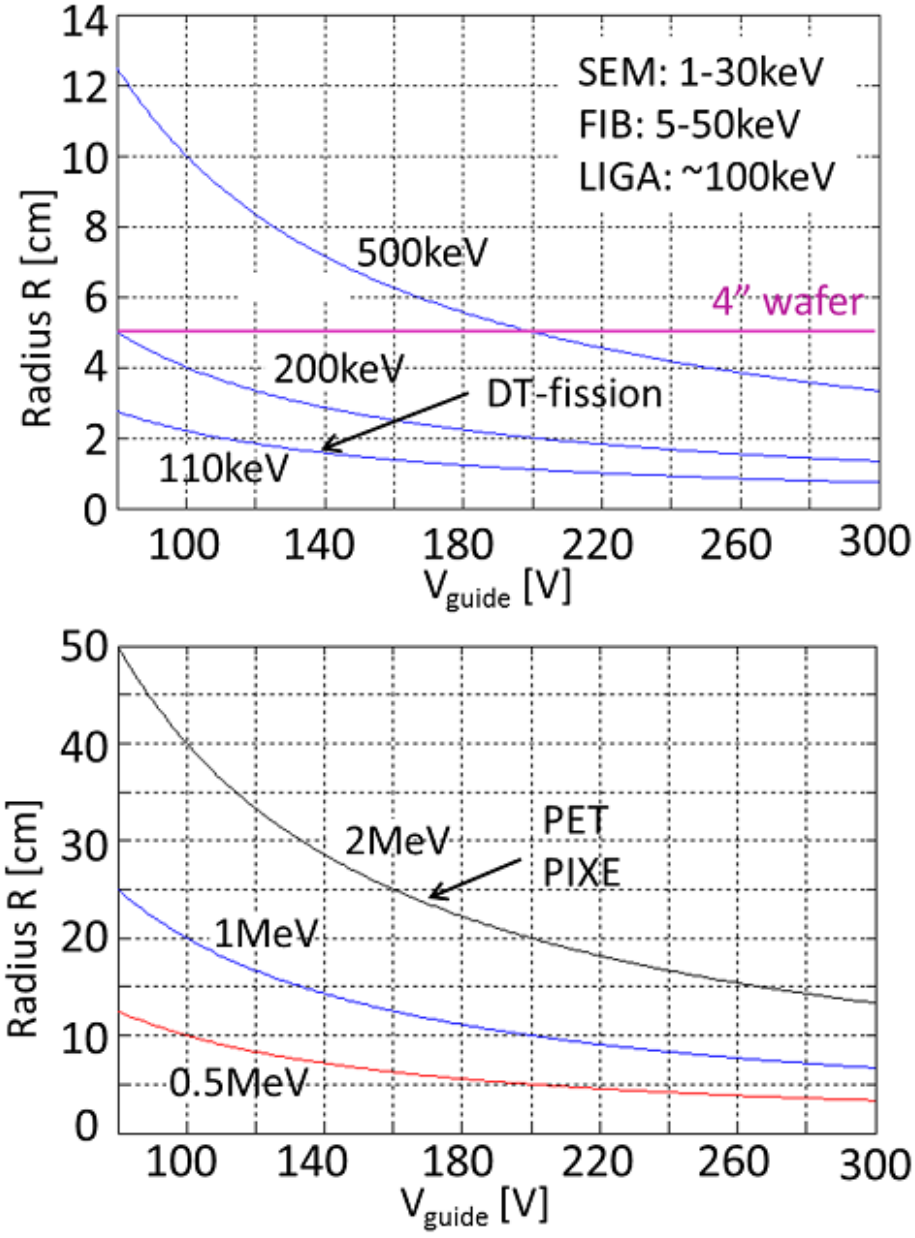

Figure 2.22 Radius of curvature dependence upon guiding voltage for various particle energies. Indicated are the typical energies used for different applications such as SEM imaging etc.

2.2. RF Linear Particle Acceleration

One of the essential components in the "toolbox" for building charged particle actuating systems are beam accelerators which target the energy range suitable for various applications. The size of accelerating systems scale up with the energy to be attained, and although football-field sized accelerators are necessary for GeV and TeV levels, tabletop sizes are appropriate for keV to lower MeV ranges. A vital part of this work is to further the miniaturization and portability of accelerators in the latter energy category, which may be achieved with electric actuation, dispensing with the use of heavy magnets. In this Chapter, after a brief historical background of the first accelerators, a linear accelerator (LINAC) design is discussed with some preliminary results. The current accelerator development for this project is still in its infancy, and a future direction to enhance the accelerating voltage will be suggested.

2.2.1. Accelerator Historical Background

In 1924 Ising put forth the idea of overcoming the voltage breakdown problem (for acceleration in one stage say, between two electrodes), by accelerating over many stages, each of which can be of lower potential. Ising's idea was to place a series of hollow cylinder electrodes in a straight line, separated by small gaps in between. This forms a so called "drift tube linear accelerator". A pulsed wave, produced by a spark plug discharge, was applied to each tube in turn, and must be timed correctly to the particles' path inside so an accelerating field is set up at each gap just as the particles are going through it. Wideröe was inspired by this concept (1927) and realized that if the drift tubes are driven by an oscillating potential, such that neighboring tubes are at voltages 180^0 out of phase, then the acceleration effect

would be the same (provided of course, that the particles are timed properly with the [potential variation). Wideröe built the first linear accelerator (LINAC) in 1927 (Aachen, Germany) as part of his Ph.D thesis, driving one drift tube between 2 grounded ones at 1MHZ at 25kV. Potassium ions were shown to gain a total of 50keV. This was the first demonstration of an accelerator with both input and output at ground and was still able to provide an energy boost that is twice that obtainable by a single gap. Sloan and Lawrence at Berkeley later in the early 30's constructed a 30 drift tube long accelerator.

Much of the limitation for linear accelerators was the need for high frequency generators in order to keep the length of the accelerator reasonable. In World War II, radio frequency, high power generator advancement was accelerated by the need for radar development. After the war, using the newly available RF oscillators, Alvarez built the first proton LINAC at the University of California Berkeley in 1946. Figure 2.23 shows the Alvarez cylindrical cavity accelerator which is driven at resonance such that the accelerating field is along the axis of the cylinder. Particles are accelerated along that axis and are shielded from by drift tubes at times when the field is acting in the opposite direction of particle motion. Driven at 200MHz, it was 12m long (1m in diameter), and accelerated protons up to 32MeV [38]. At the same time, an electron accelerator was being built at Stanford (SLAC). These two accelerators became the spring-board from which particle physics took off.

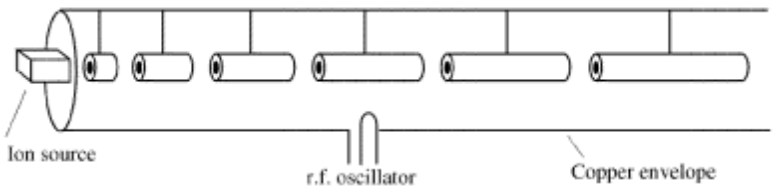

Figure 2.23 Alvarez's concept of the Linear Accelerator. Image taken from [39]

Previous table-top ion-accelerating devices have made the use of pyroelectric crystals [40] [41], and femtosecond lasers [42] to generate electrical forces on charged particles. Direct guidance of ions on the micron scale has been demonstrated on atom-chips which trap ions above the chips' surfaces but at very low energies [43] [44]. These chip-scale methods require high currents and heavy equipment e.g. lasers and low-temperature environments.

Acceleration using only electric actuation, implemented on the planar architecture in line with the main concept of this work, will greatly reduce the size of accelerators without the use of bulky lasers or magnets. The geometry of the linear RF accelerator [45] is suitable for integration into planar electrode structures.

2.2.2. Theory and Design Considerations

A traditional RF linear accelerator consists of a series of cylindrical drift tubes, aligned axially as shown in Figure 2.24 such that the charged particles travels along the axial length. When the drift tubes are driven alternatively at RF, such that neighboring tubes are π out of phase, a strong field will exist periodically in the gaps between the electrodes (when the neighboring electrodes are at their peak voltages of opposite polarity). If the charged particle is synchronized to the driving RF appropriately, it will enter a gap when the field

there is highest and is in the direction of its motion, in which case its energy will be boosted (Figure 2.25). While the particle is travelling within a drift tube electrode, it experiences no spatial change in potential in the axial direction, and hence no force along its direction of motion. Even though the potential of an electrode may be varying in time relative to its neighbor, the potential is uniform inside the electrode itself in the axial direction (ignoring any space-charge effects).

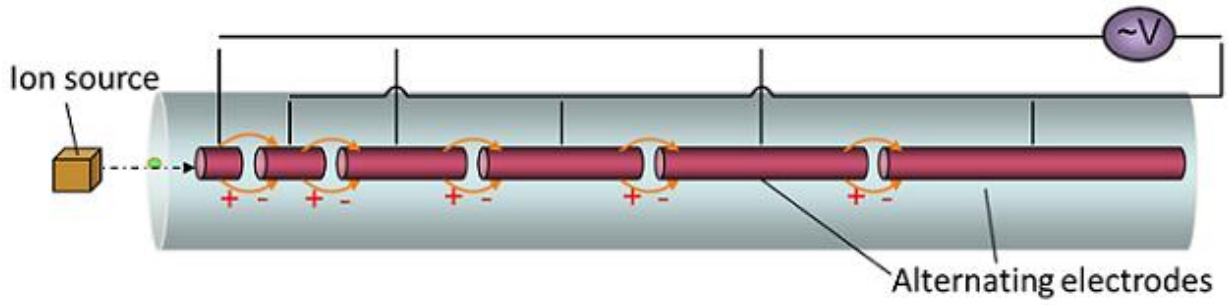

Figure 2.24 Traditional RF linear accelerator (LINAC) concept. Particle enters from the left and acceleration occurs across each gap.

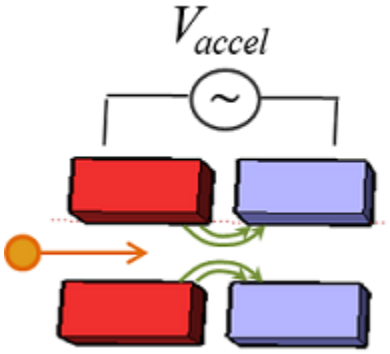

Figure 2.25 Illustration of one gap in a linear accelerator adapted into the planar, rectangular architecture. Driven at RF, the red pair is π out of phase with the blue pair – particle acceleration occurs within the gap.

For our work, instead of cylinders, the accelerating electrodes can be defined as rectangles patterned on a planar substrate (Figure 2.25, Figure 2.26). The principles of acceleration described above are still relevant, especially for particles near the channel center. There may be fringing effects due to the corners and edges of this rectangular geometry, but if the channel wall height-to-width ratio is high, beam losses could be minimized. Discussed briefly below are a few important design factors must be taken into consideration for the design of a linear RF acceleration.

i) *RF Electrode Lengths*

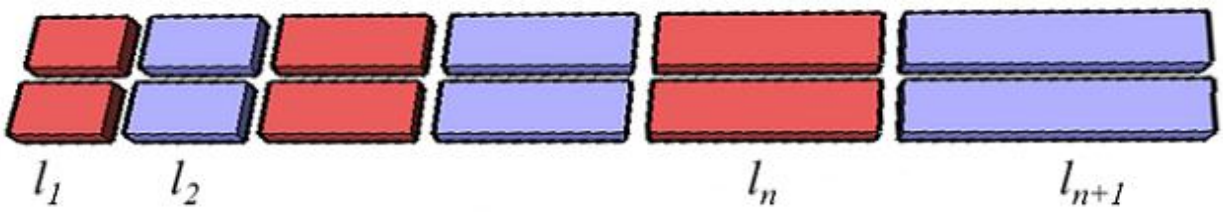

Figure 2.26 Illustration of consecutive increase in the electrode lengths in the LINAC

Each time a synchronized particle is accelerated across a gap, it attains a higher velocity in its direction of motion, and will travel a greater distance during the constant period (or half-period) of RF oscillation (since the frequency of the driving RF remains the same). The linear accelerator design then requires consecutive lengths to be increased as shown in Figure **2.26**. The lengths l of the electrode after the n^{th} acceleration should be designed to be:

$$\boldsymbol{l_{n+1} = \frac{v_{n+1}}{2f} = \frac{1}{2f}\sqrt{\frac{2q}{m}(V_0 + nV_{accel})}} \qquad (\mathbf{2.12})$$

where f is the driven RF frequency at the peak-to-peak (p-p) voltage V_{accel}, v is the velocity of particle, m the mass, q the charge, and V_0 the voltage equivalent of the particle's initial energy

before entering the accelerator. Note, the above calculation assumes a non-relativistic particle. Hence for a given particle beam energy and chosen RF frequency, there is an optimum electrode length series

ii) *Gap Length*

Another design concern is the gap size between the pairs of electrodes. If the gap is very large, during the time it takes for the particle to traverse that gap, the oscillating voltage may have changed substantially so that the energy gained by the particle is lower than if there was a constant DC voltage. This effect is called the transit-time effect [45].

Let the electric field in the axial direction across the gap be:

$$\mathbf{E_z(r = 0, z, t) = E(0, z)\cos[\omega t(z) + \phi]} \qquad (\mathbf{2.13})$$

where at time *t=0* the particle is at phase ϕ relative to the crest. For a particle crossing the gap of length *g*, the energy gained is:

$$\boldsymbol{\Delta U = q \int_{-g/2}^{g/2} E(0, z)\cos[\omega t(z) + \phi]dz} \qquad (\mathbf{2.14})$$

If the p-p voltage is

$$\boldsymbol{V_0 = \int_{-g/2}^{g/2} E(0, z)dz} \qquad (\mathbf{2.15})$$

then the energy gain can written as:

$$\boldsymbol{\Delta U = qV_0 T\cos\phi} \qquad (\mathbf{2.16})$$

where the time-transit factor *T*, given that electric field is an even function about the middle of the gap is:

$$\boldsymbol{T = \frac{\int_{-g/2}^{g/2} E(0,z)\cos[\omega t(z)]dz}{V_0}} \qquad (\mathbf{2.17})$$

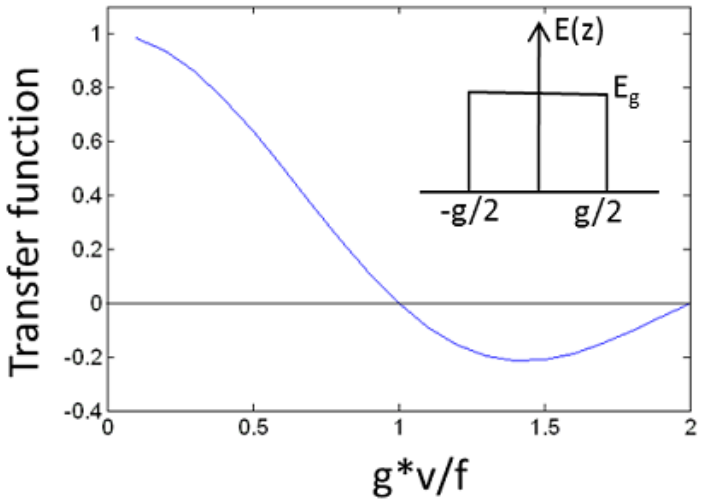

Figure 2.27 Plot of the time-transit factor T as a function of $\boldsymbol{gv/f}$ for a square-wave electric field profile within the gap of length g.

Much of the physics is hidden within the transit-factor which could be a complicated function. *T* determines the reduction in RF energy transferred to the particle, due to the time-varying nature of the field within the gap. If the gap field is approximated to be constant E_g within the gap and zero outside as shown in Figure 2.27 inset, then *T* can be written as:

$$\boldsymbol{T = \frac{\sin\left(\frac{\pi g}{\beta\lambda}\right)}{\frac{\pi g}{\beta\lambda}}} \qquad (\mathbf{2.18})$$

Here, $\beta = v/c$ and $\lambda = 2\pi c/\omega$. $\beta\lambda$ is the distance the particle travels in an RF period. Eqn.2.18 is plotted in Figure 2.27 as $g/\beta\lambda = gv/f$. It is clear that to maximize the transferred energy ΔU, *T=1*, which means that g should be zero. In practice then, *g* must be kept as low as possible, taking into account electrical breakdown and fabrication limitations.

iii) *Accelerated Energy's Robustness to Frequency Changes*

For a given initial beam energy and associated accelerator lengths, there is one resonance frequency for which the final accelerated energy is maximum. If the frequency is off-resonance, the final beam energy is lower than optimal, and this is reflected in the simulation result in Figure 2.28. (The electrode geometry in this example is similar to that which was later fabricated and tested).

Figure 2.28 shows that for this simulated example, the reduction in final energy is small if the frequency is varied a few MHz from resonance. Hence as a point of practicality, the LINAC is robust to changes of a few MHz in driven frequency, which is beneficial for device testing purposes.

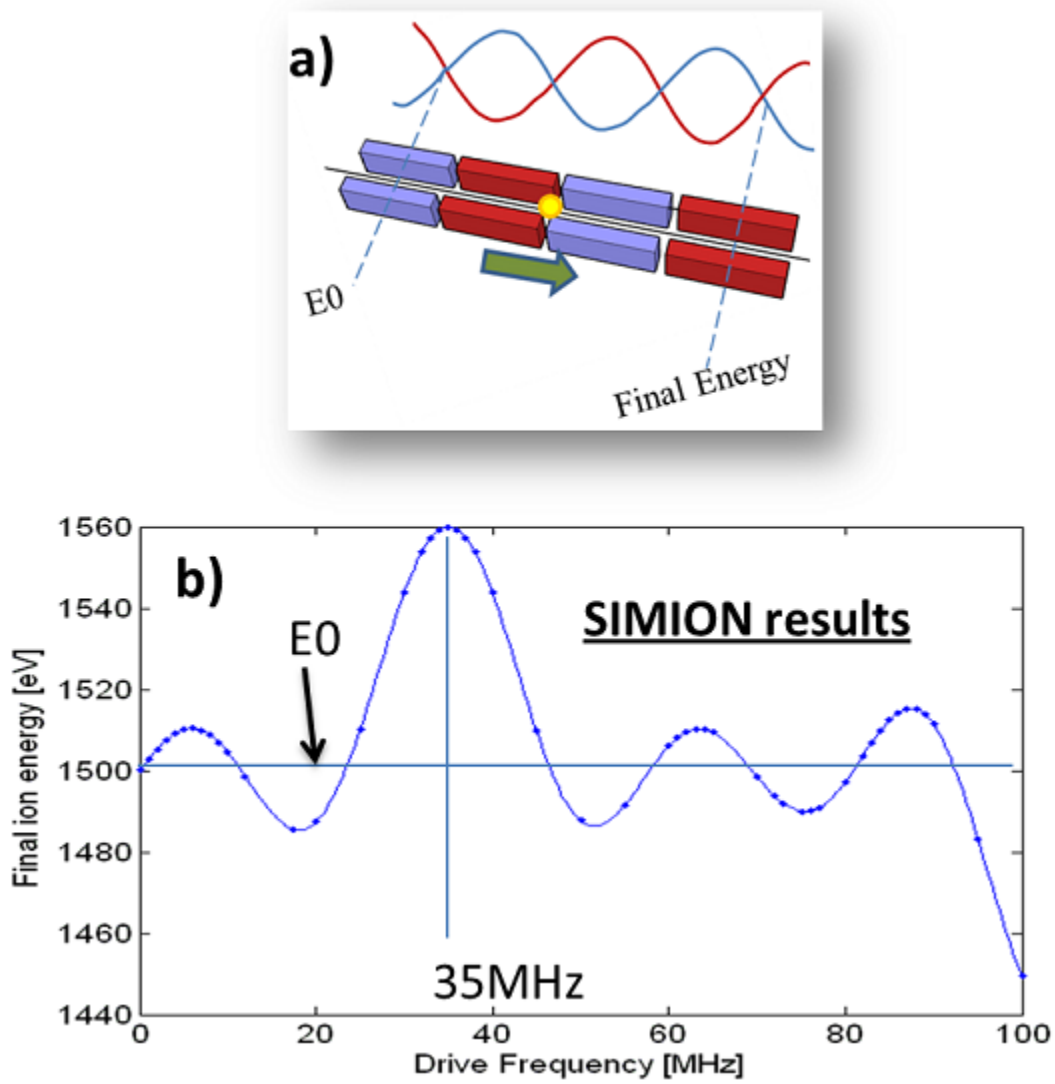

Figure 2.28 a) Illustration of a LINAC with four segment pairs that was simulated for particles with initial energy 1.5keV. The structure was designed for resonance frequency at 35MHz. b) shows the change in the final accelerated energy as the drive frequency moves away from resonance. The simulation is for a single particle that is synchronized to 35MHz for a maximum of 60eV acceleration – accelerator parameter was taken to be 20V p-p at each of the 3 gaps.

iv) Phase Considerations

From Eqn.2.16, the energy a particle gains across a gap is dependent on ϕ, its phase relative to the driving RF frequency. This is illustrated in Figure 2.29: simulation results of particles at various phases relative to the driving RF electrode oscillation, accelerated through a three-gap channel. The energy spread around the initial energy 1.5keV is clearly dependent upon the relative phase: the maximum total energy gain of 60eV, for which this accelerator was designed, occurs when the particle is in sync (phase zero); the particle is retarded by 60eV if it is 180° out of phase; and does not gain any energy when it is 90° out of phase.

Traditionally, most particle beams are pulsed or bunched before they pass through the LINAC and are synched to the RF, so that the deceleration case does not occur, and energy gain is maximized for the particle bunches. However in this work, we are limited to a continuous beam of charged particles and so consistent with Figure 2.29 we expect to measure a spread of energy around the initial energy E0, the data of which is shown in Section 2.2.4. In addition, our measuring setup does not yet have the timing resolution to differentiate particle bunching.

Simulations were made to estimate the energy spread profile of the continuous beam, taking into account the phase dependent effect described, for the above mentioned geometry. In addition, one needs to consider the energy spread of the initial beam entering the accelerator: it is not mono-energetic, but is assumed to have a Gaussian distribution. In order to take these two factors into account the following estimations were done: a range of initial input beam energies were weighted by the Gaussian distribution; for each of the energies the resulting final energy spread was found by varying the relative phase of the driving RF accelerator; the procedure was

repeated for a range of initial energies and the final energy was subsequently binned, weighted by the Gaussian weight.

The result of the energy distribution predicted in this fashion for an 3 gap accelerator driven at 35MHz 10V p-p is shown in Figure 2.32A. (In the figure, the absolute values of the counts on the y-axis are not significant – only their relative heights and general shape of the distribution is of interest). The figure indicates the expected spread in energy about the initial energy at the entrance. Furthermore, the spread is not uniform, but forms two peaks above and below the initial energy.

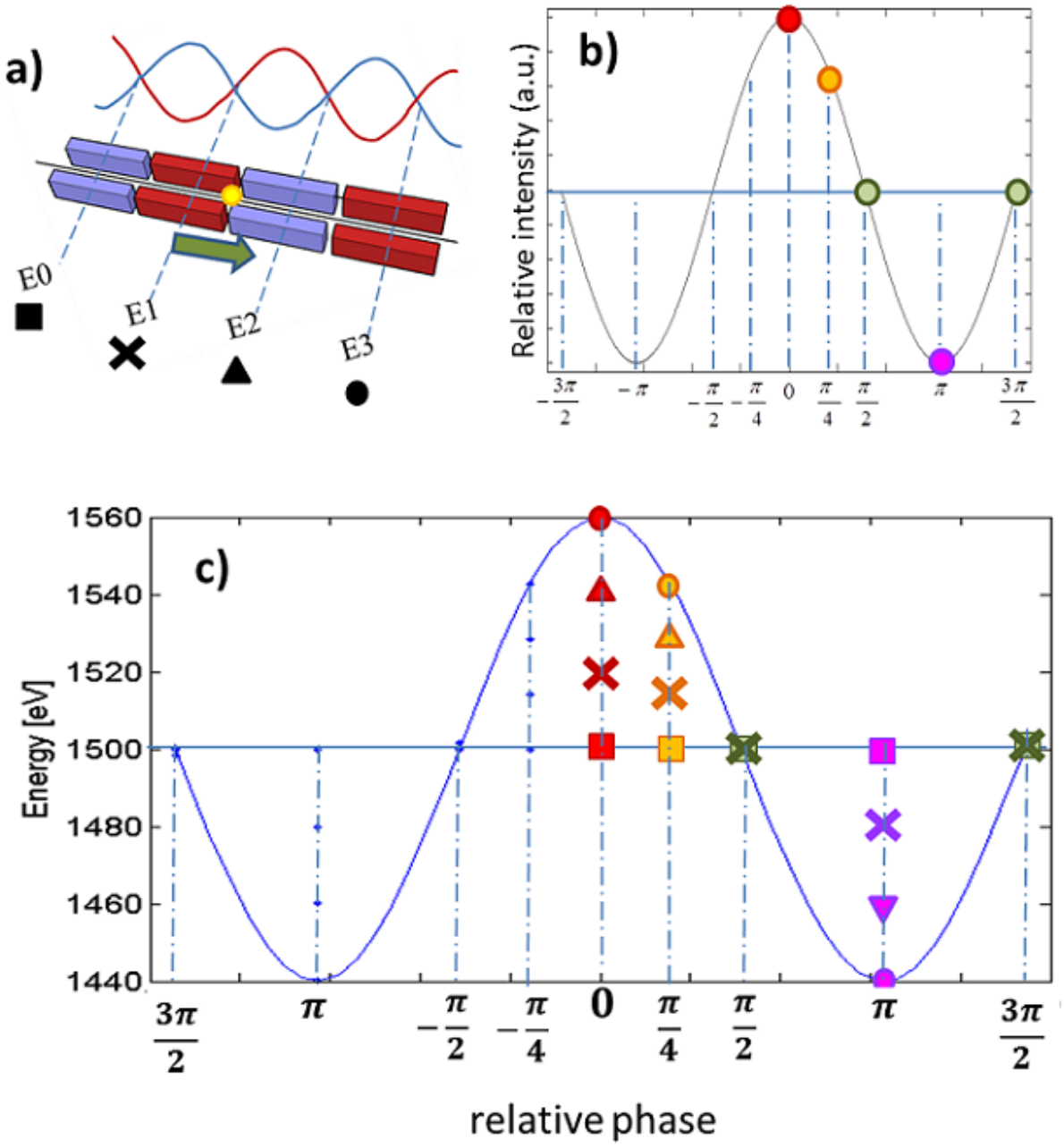

Figure 2.29 a) Illustration of simulation setup: particle enters with initial energy E0 from left. After each gap the energy is recorded as different point style, corresponding to the simulation result in c). The relative amount of acceleration of particles as a function of their relative phase to driving oscillation is shown in b). c) Simulation of the energy spread of particles with initial energy of 1.5keV: phase variation is sorted by color; particle energy along accelerator channel (at constant phase) is indicated by various point styles.

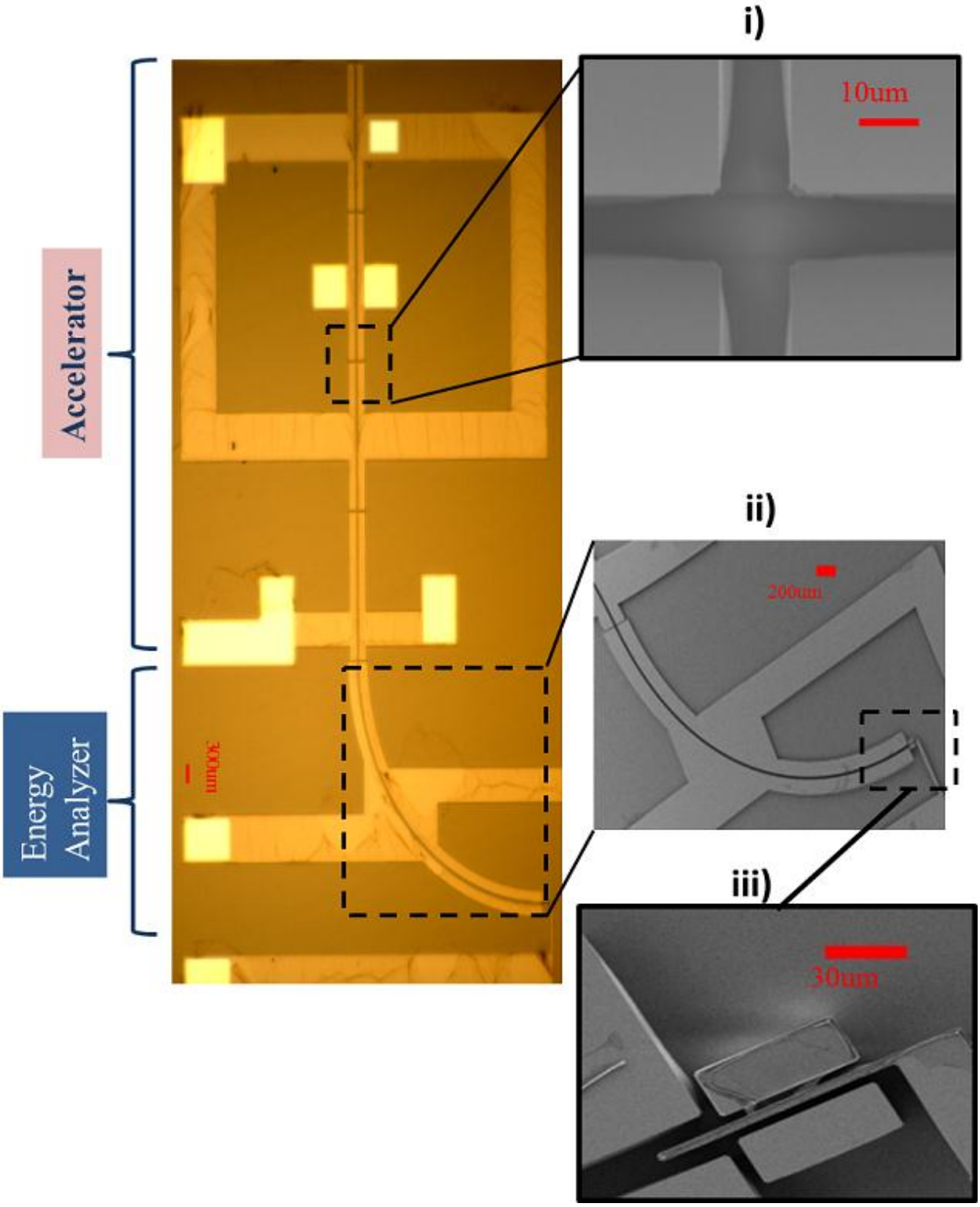

Figure 2.30 SOI implementation of a 4 segment linear accelerator with curved energy analyzer to determined final accelerated particle energy. Beam enters from the top. SEM images are shown of i) gap between accelerating electrodes, ii) curved energy analyzer, iii) particle detection electrode at the end of the curved channel.

2.2.3. Fabricated Device

The simulated geometry of a four-segment linear accelerator design in Figure 2.29 was implemented on SOI as shown in Figure 2.30. The gap between the accelerating electrodes is 10 μm, while the channel width is also 10 μm. The lengths of the segments are designed for a resonance frequency of 35MHz driven at peak-to-peak voltage of 10V, to garner a total energy gain of 30eV after passing through 3 gaps. Ar^+ ions of 1.5keV is injected into the accelerating channel. Upon exiting the channel, the ions passes through a 90° curved guide which acts as an energy analyzer to determine the energy of the particles after acceleration, by varying the potential difference between the curves and sensing the guided particles by an electrode positioned at the end of the channel.

2.2.4. Acceleration Results: Simulated and Measured

The Ar^+ beam was aligned into the channel with the procedure outlined in Section 2.1.4 for a curved guide. For alignment purposes, the RF acceleration is first switched off. Then the beam is swept along the top edge of the device just as in the procedure for guidance testing. The background signal is taken as the current signal detected when the guiding potential on the curved electrodes is zero. Subsequently a guiding voltage of 30.6V is turned on, and the current is again measured with relation to beam position. The difference between the two is plotted in Figure 2.31, which shows a clear peak where the beam was correctly positioned to enter the channel opening of the SOI device.

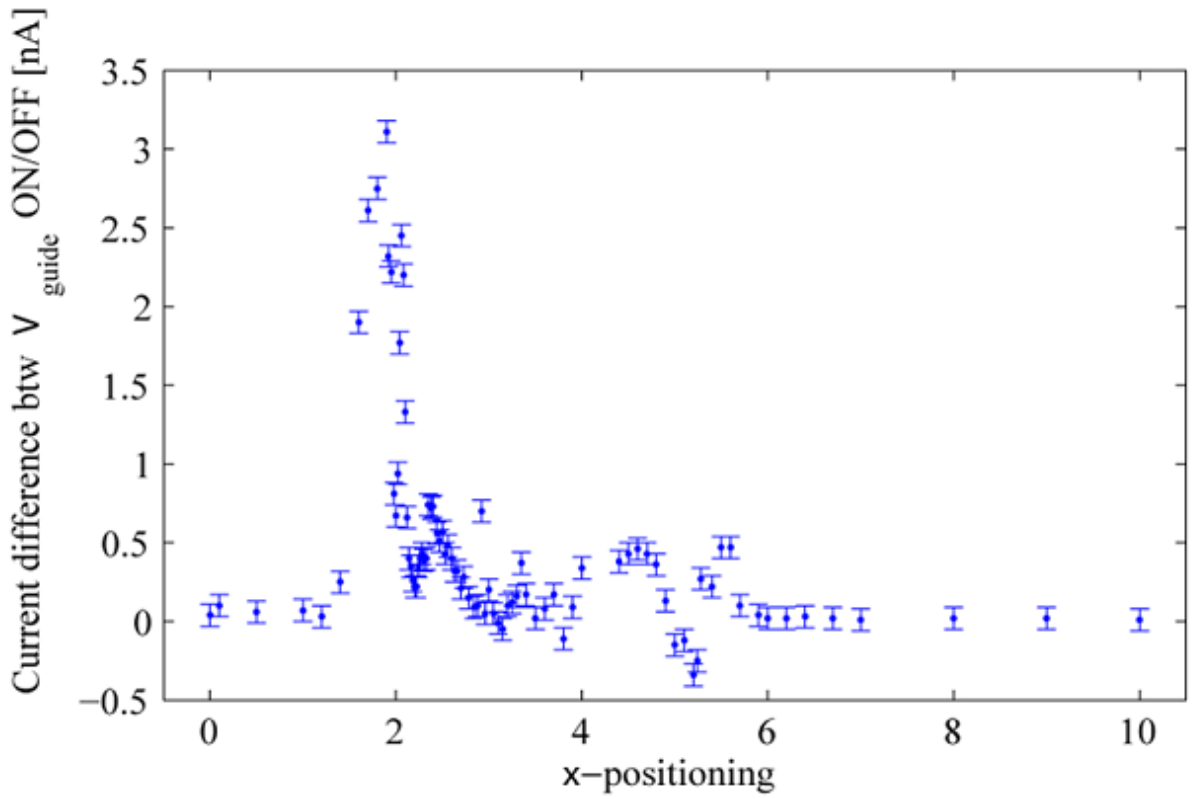

Figure 2.31 Alignment of the 1.5keV beam into the channel without acceleration. Beam current signal from the end detector shown in Figure 2.30 is plotted as a function of position along the device edge. The data plotted is after background subtraction. The current signal for the case when the guiding voltage V_{guide} is switched off, is subtracted from the case when the V_{guide} is switched on.

After the position of the channel opening is found, RF acceleration is ready to be tested. The RF signal is applied to the linear acceleration electrodes; the guiding voltages on the curved electrodes are swept; and the current on the end detector electrode is recorded. From the resulting energy distribution data, the distribution with no RF signal is subtracted, and the result is plotted in Figure 2.32B. A double peak distribution is shown which fits the simulation prediction: the range of the measured distribution is not far from that of the simulated and the middle of the spread is around the initial particle energy 1.5keV. This is strong evidence that some of the on-resonance particles were accelerated.

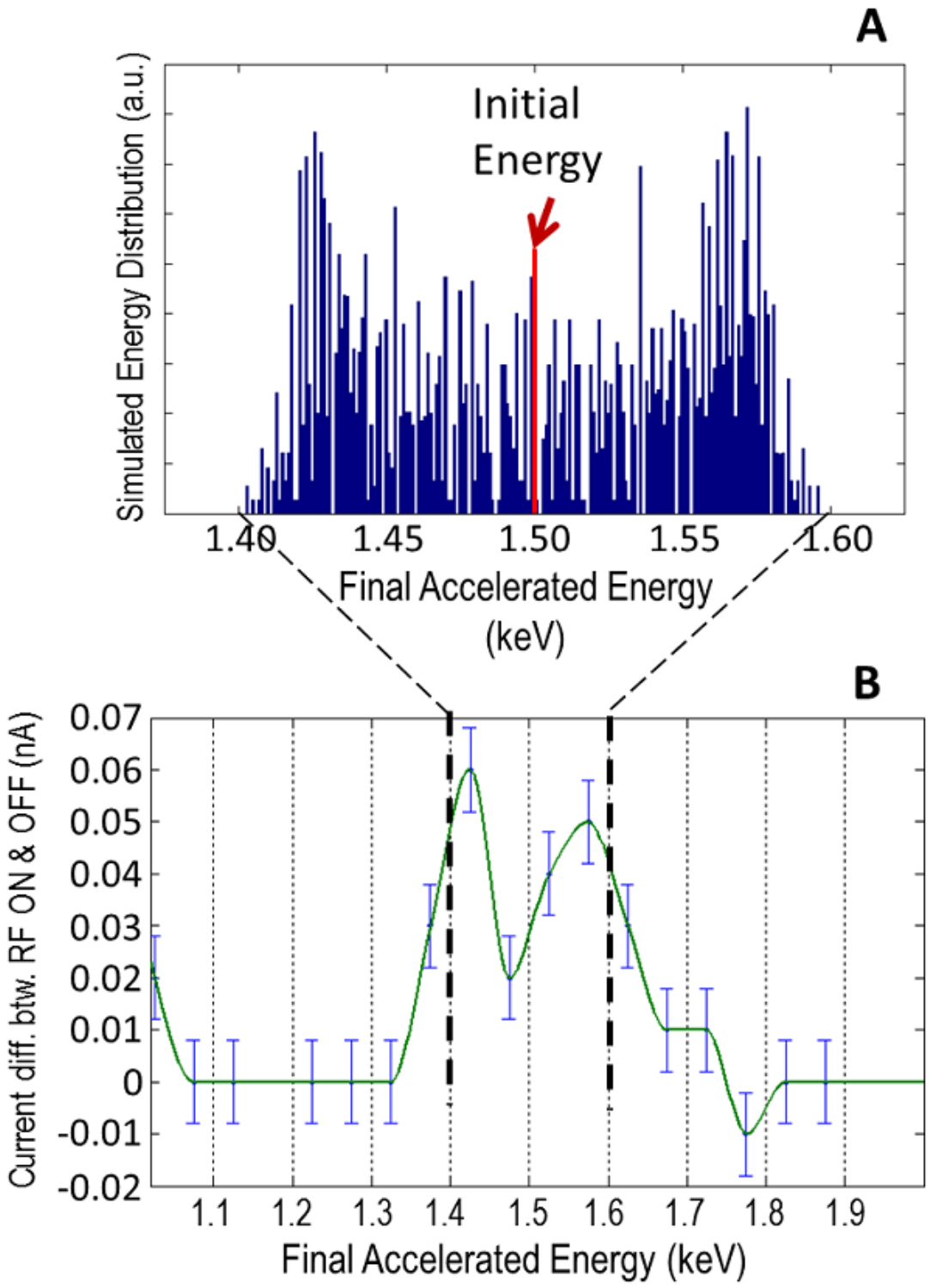

Figure 2.32 A) Simulated result of the predicted energy distribution of the final accelerated energy of argon particles, entering the accelerator with initial energy of Gaussian distribution around an average of 1.5keV. Geometry simulated is for device in Figure 2.30. B) Measured current signal data of final accelerated argon ion energy distribution.

As the accelerating structure was fabricated on SOI, the aspect ratio of the channel height to width is 2, and so the SNR is unfortunately very low. In addition, the beam traverses 11.7mm from the accelerator entrance to the detector electrode at the end of the channel without any refocusing, resulting in substantial beam current loss. A beam being accelerated in its direction of propagation in an RF field will experience a defocusing effect. Consider a cylindrical geometry with *z* as the direction of propagation and *r* the transverse dimension. The field varying in time will also mean that parts of the beam will experience a negative field gradient: $\frac{dE_z}{dz} < 0$. But since $\nabla \cdot \vec{E} = 0$ (neglecting space charge), then the transverse component of the field must have a positive gradient as:

$$\frac{\partial E_r}{\partial r} + \frac{\partial E_z}{\partial z} = 0$$

$$\text{or} \qquad \frac{\partial E_r}{\partial r} > 0$$

Therefore, some particles within the beam will experience an outward transverse force, defocusing the beam. It can be shown from [46] that for an accelerating field in the *z* propagation direction of $E_z(0,z) = -E_0 \sin(2\pi z/\lambda)$, the radial component of the electric field is

$$E_r(r,z) = \left(\frac{r}{2}\right)\left(\frac{2\pi}{\lambda}\right) E_0 \cos\left(\frac{2\pi z}{\lambda}\right) \tag{2.19}$$

Hence the further the charged particle is away from the axis (*r>0*) the greater will be its deflection. However, if the gap across which a particle is accelerated is small, its deflection due to E_r may also be small. For example, a 2keV electron would take about 7.6×10^{-12}sec to cross an accelerating gap with size $g = 200\mu m$. One may simply approximate $E_0 \approx V/g$ and for this example E_r is approximately constant with respect to z. If the driving RF is at *V= 300V* p-p, from Eqn.2.19, the deflection for a 2keV electron at position *r=100 μm* is about 90nm. This radial defocusing effect is most prevalent in low energy beams hence there should be refocusing

lenses to stabilize the beam after acceleration. The next chapter deals with the implementation of an electrostatic Einzel lens for beam focusing purposes, which could enhance accelerated beam flux, if integrated with the LINAC section.

Despite the large noise and low current signal, the fact that acceleration is still demonstrated, with matching simulations, is promising for further development. Some of the improvements for implementing a LINAC that would provide thousands of eV energy gain and still maintain a compact size with minimized beam loss, not only involve raising the aspect ratio of the acceleration channel and providing beam focusing, but also increasing the p-p voltages across the accelerating gaps. The next section will discuss the direction of future work in an attempt to boost the accelerating RF voltage.

2.2.5. Outlook: Ventures into RF Coplanar Resonator-Based LINAC

In order to implement small features for miniaturized accelerating components, the driving RF frequency must be high, especially for electrons which reach relativistic speeds in the keV range: for example, at 100keV electron speed is 0.55*c*; at 200keV it is at 0.7*c*; at 500keV it travels at 0.86*c*; and at 1MeV its speed is at 0.94*c*. Considering these speeds, the frequency applied to the electrodes of the linear accelerator (LINAC) should be on the order of GHz and above, if one wishes to keep the total length of the LINAC on the order of centimeters. Furthermore, if the p-p voltage across each gap is high, then the number of accelerating stages can be lowered, reducing in turn the overall LINAC length. In the simplistic capacitor model, the RF power needed is proportional to CV^2f, for capacitance *C*, p-p voltage V and frequency *f*. However, the amount of power that can be provided by a RF

source and amplifier combination is limited. Using a commercial 30W amplifier [Model number], we observed p-p voltages of only up to around 10V at 35MHz.

One avenue of development that could be approached to enhance the p-p voltage oscillations is to realize a co-planar waveguide resonator with high Q (e.g. 50 - 100), and tap off the potential at the peak positions, as illustrated in Figure 2.33. Since we wish to keep the resonator consistent with the planar architecture of the entire device, the coplanar strip resonator is a good choice for integrated resonant cavities. This is in contrast to the bulk 3D microwave resonator structures used in conventional LINAC structures [ref].

Quality factors of 100-300 are possible with higher Q's for ceramic PC-boards. The peak voltage in a waveguide can be written as

$$V_{peak} = Q\sqrt{50 * \sqrt{2}P_{ave}}$$

where Q is the resonator quality factor, P_{ave} is the average power and 50-ohms is the characteristic waveguide impedance. Assuming a Q of 200, from an impedance matched 10Watt source with 50-ohms impedance, a peak voltage of 5319 Volts can in principle be achieved. This voltage is still below the breakdown voltages, described in Section 4.4. In fact the breakdown voltages at higher frequencies are in general higher due to lower probability of avalanche creation during the short high electric field durations.

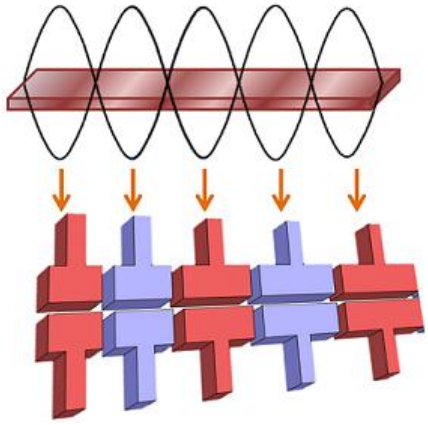

Figure 2.33 Illustration of using coplanar strip resonator voltage oscillations to facilitate the accelerating voltage across the gaps of the linear accelerator.

Using a RF simulator Sonnet Software [46], we designed a RF coplanar strip resonator with dimensions to accommodate an accelerator driven at about one GHz to electrons with initial energy of 2keV. Given that the points of high voltage (or charge concentration) on the resonator are desired to be positioned close to the accelerating electrodes of fixed separations, and that the charge concentration pattern on the resonator is dependent on the frequency, a meandering comb-shaped resonator structure was devised. The Sonnet simulation for this design is shown in Figure 2.34. The comb structure was designed such that at 950MHz, the inner fingers of the comb all exhibit high charge density compared to the outer fingers so that, having the accelerating structure placed in the middle of the comb, the acceleration electrodes lay in close proximity to the inner fingers – the fabricated device is shown in Figure 2.35.

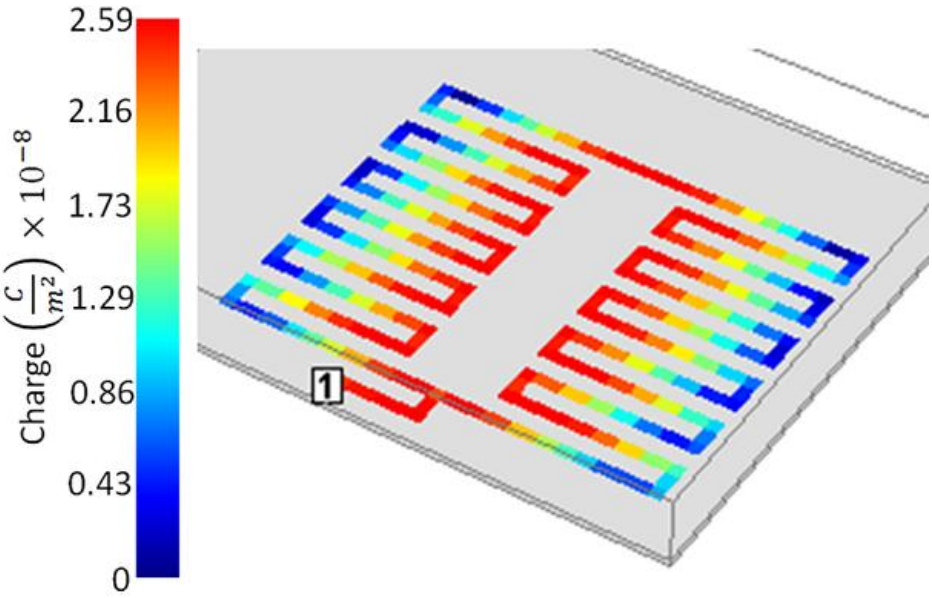

Figure 2.34 Sonnet simulation result for a comb-shaped coplanar strip resonator (copper on FR4) is shown with the charge density depicted in color. The port through which the RF signal is applied is marked at "1". 950MHz is applied.

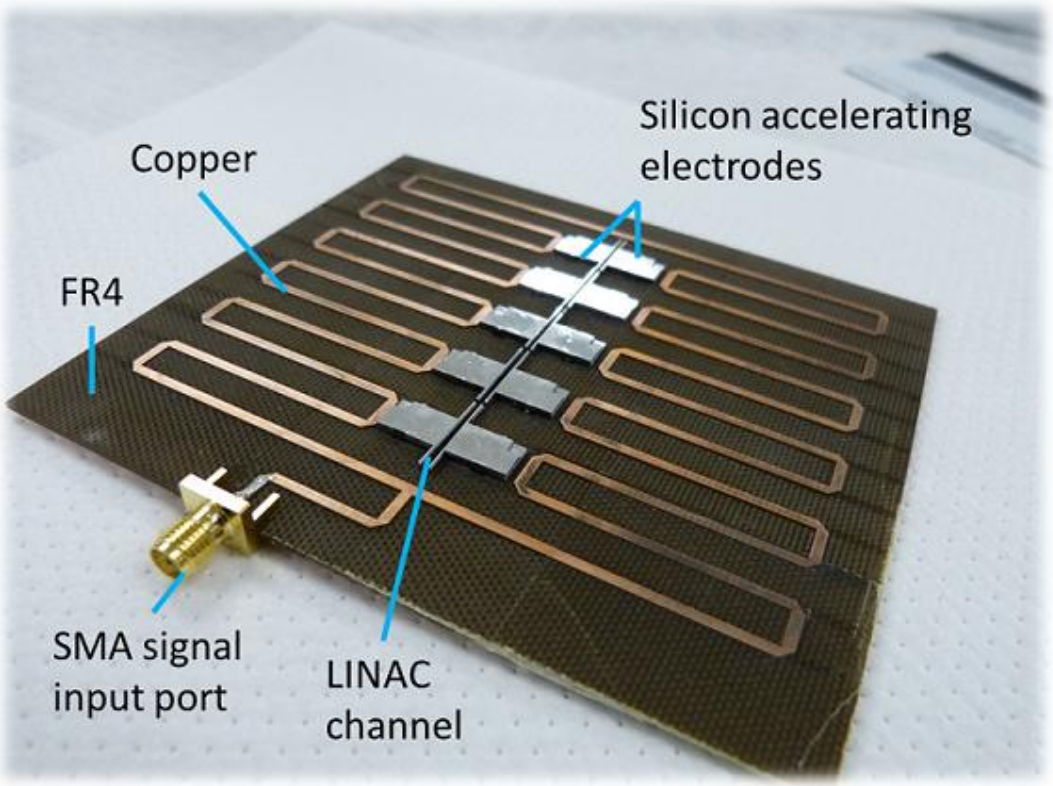

Figure 2.35 Photo of assembled device of Si LINAC on top of PCB coplanar resonator.

As shown in Figure 2.35, PCB with etched copper provides the platform for the coplanar strip resonator, while the accelerator itself is fabricated with doped silicon, and the entire device is assembled via the fabrication process detailed in Section 3.4. The metal layer on the back-plane of the PCB is grounded, and a SMA connector provides the RF port. The inner fingers of the comb are accessed via wire-bonds by the accelerating electrodes. The simulation of the LINAC section (Figure 2.36) indicates the expected energy gain along the channel for an electron entering the accelerator with 2keV, using the given design parameters.

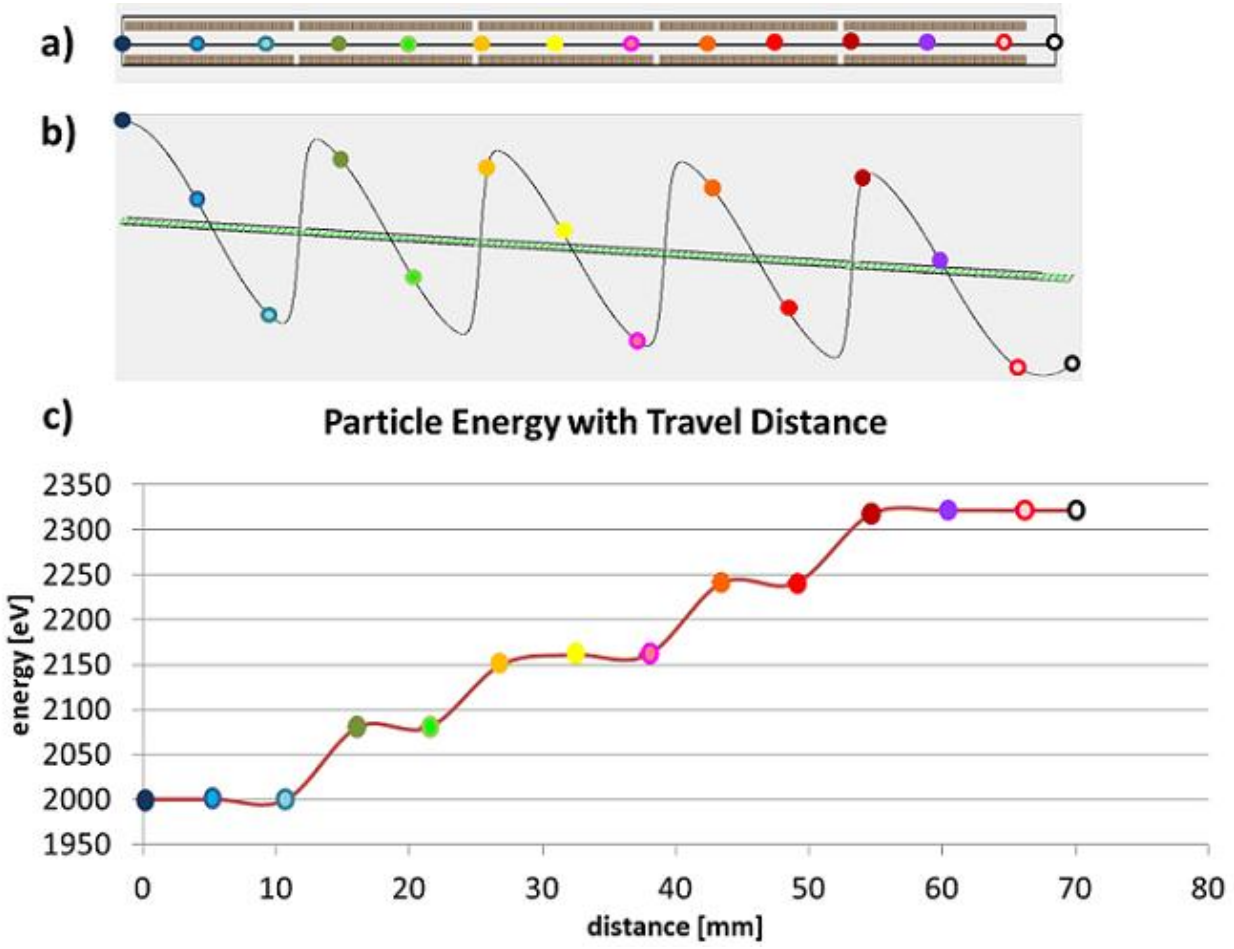

Figure 2.36 Simulation of accelerator fabricated and shown in Figure 2.35. a) Simulation geometry and the positions of the electron indicated in colored spots. b) the potential as experienced by the electron for a 75V p-p driving voltage. c) The increase in electron energy as a function of its position along the accelerator channel.

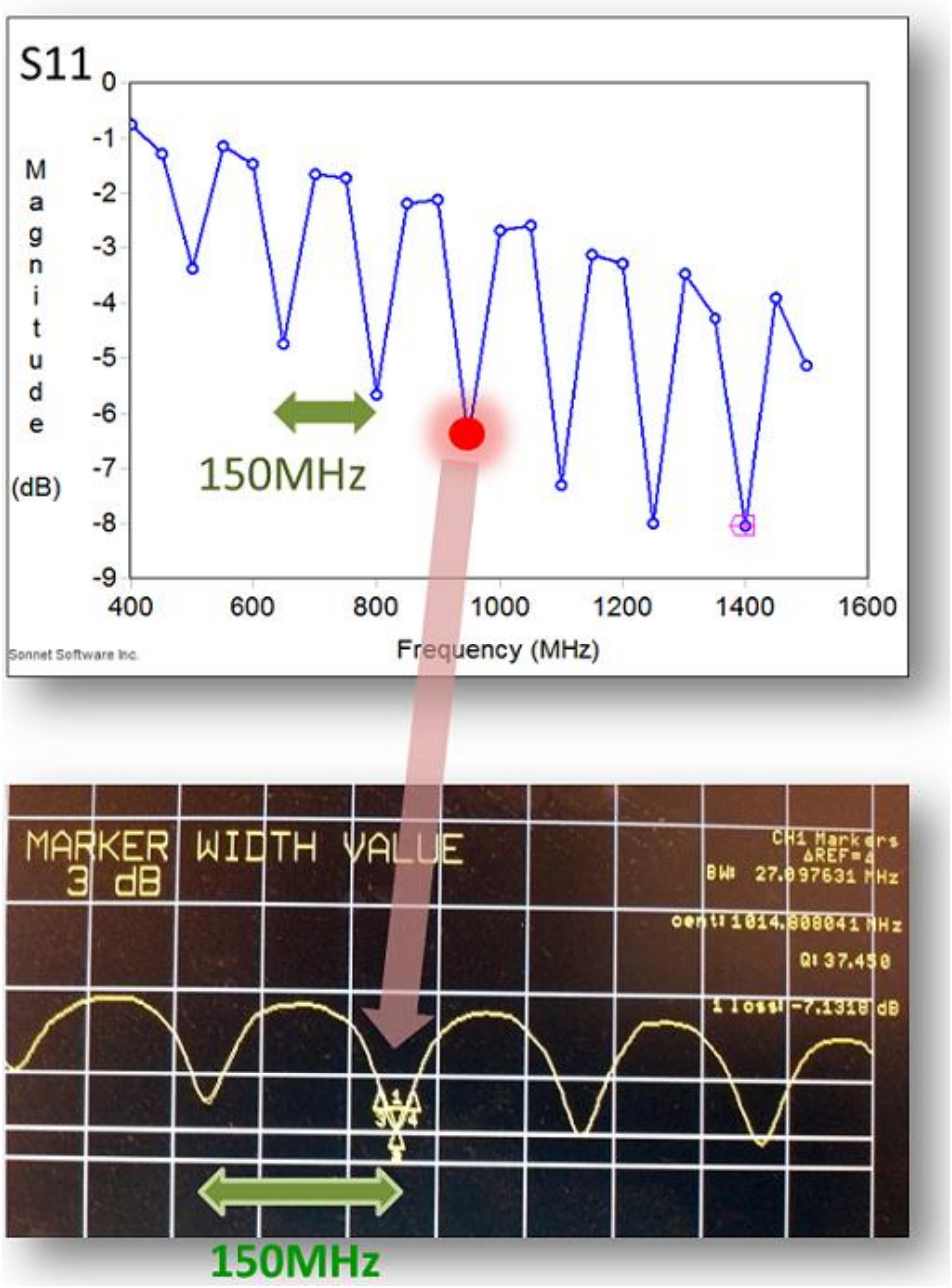

Figure 2.37 Sonnet simulation of the S11 response of the comb resonator in dB is shown on top. The measured S11 response is shown on the bottom.

The S11 response of the coplanar comb resonator on PCB is shown in Figure 2.37, which compares the simulated response with the measured one. Although the dipping peaks in the measured response are all slightly shifted (by 65MHz) compared to the simulation response (e.g

simulation predicted a peak at 0.95GHz, while the measured response indicates a peak at 1.014GHz), the frequency spacing of 150MHz between the peaks remain the same. The measured Q at 1.0139GHz is 37.4 (and a bandwidth of 27MHz), with the S11 at -7.28dBm. The reflection co-efficient Γ is then 0.432 from the relation: $S11(\text{dBm}) = 20log_{10}|\Gamma|$. This high reflection coefficient value indicates that almost half the input power is lost due to impedance mismatching. The measured impedance (*R-iX*) is *R=22.5Ω*, and *X=16.5F*.

A needle probe was used as a rough first order measurement of the oscillating voltage sustained on the copper strip surface. The probe ground is connected to the resonator ground. Signal detected by the probe is read into an oscilloscope, and the probe point can be moved to any position on the strip resonator. Probe measurements can test two factors of importance to the comb-resonator design: i) the positional variations of the relative p-p voltages, and ii) the relative phase at the neighboring inner fingers. Figure 2.38 shows that in this respect the probe measurements of the voltage behavior matches the simulated phase profiles.

i) Moving outwards along a finger, from the tip of inner finger to that of the outer one, the measured p-p voltages fall from to less than 14% the value (of the inner tip). See Figure 2.38b). It should be emphasized that the probing measurement taken in this fashion is not an absolute measurement of the voltages on the strip, since the RF coupling between the strip and the probe is not ideal. Instead, the relative voltage oscillation intensities measured are of significance and is supported by the simulation at 1.014GHz.

ii) Consecutive inner fingers are π out of phase with each other in terms of the RF voltages they sustain. A demonstration of such a measurement is shown in Figure 2.38c) in which two neighboring inner finger tips are probes simultaneously, and the resultant

oscilloscope trace displays the phase difference. Since consecutive finger tips feed into the corresponding acceleration electrodes, the π phase difference is essential to maximize the p-p voltages across accelerating gaps.

The demonstrated behaviors i) and ii) for the comb design are very promising for resonator facilitated linear accelerators on a planar geometry. The development of the RF accelerator is a work in progress, and engineering challenges include the impedance matching of the transmission lines, devices and resonators to maximize the power delivered to the particle beam. The fabrication procedure described in Section 3.4 will ensure higher channel aspect ratios to reduce beam current losses. The demonstration of acceleration on SOI and the possibility for low power (low current), resonator-enhanced accelerating voltages paves the way for the miniaturization of RF LINACs.

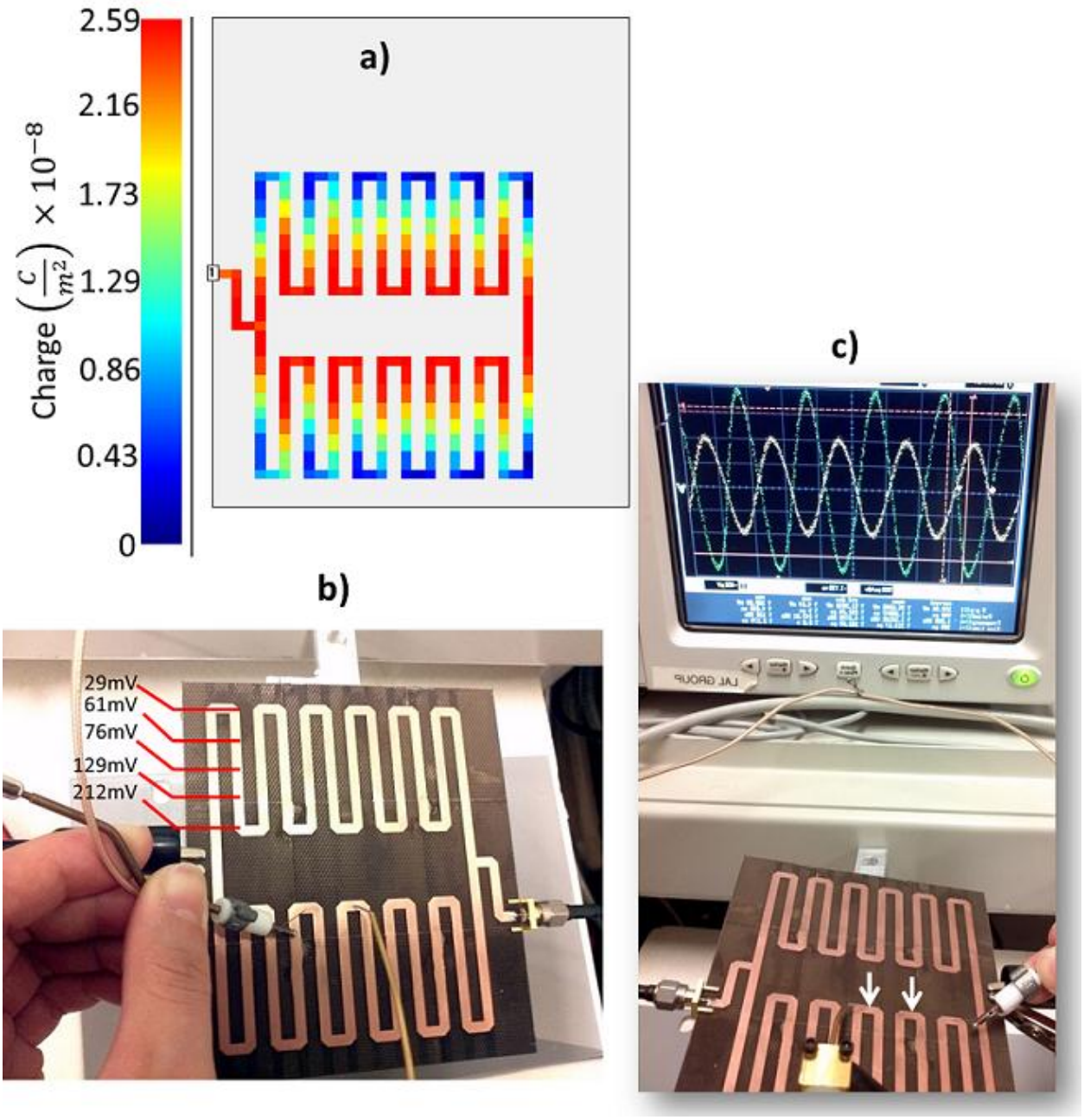

Figure 2.38 a) Sonnet simulation of charge density on the comb resonator. b) Needle probe measurement of the p-p voltage at various points along the comb finger as indicated in red. The probe measurement values shown indicate relative voltage magnitude, not absolute magnitude. c) Probing two inner fingers simultaneously, the voltage oscillations are displayed on the scope, indicating the two neighboring fingers are 180° out of phase.

3. MULTI-LAYER ELECTRODE STRUCTURE FOR EINZEL LENS ELECTRON BEAM FOCUSING

The ability to transport a beam of charged particles is essential in many fields that include nuclear collisions for atomic physics, x-ray generation for crystallography of molecules, biological scanning (radiographs, tomography, fluorescence) and radiotherapy, materials imaging with e-beam such as scanning electron microscope (SEM), transmission electron microscope (TEM), scanning tunneling microscope (STM), surface imaging with an ion beam (FIB) [47], and ion beam cancer therapy [48] [49] [50]. Hence beam transportation or "beam optics" has been extensively studied for decades [10], [51], [52], [53], [54], [55].

The aim of charged particle guidance is to minimize flux loses as the beam traverses different actuating components of the system. Hence the focusing of the beam (periodically) along its path is essential, as naturally most elements induce beam divergence. Focusing can be achieved using magnetic or electrical forces. While magnetic focusing is suitable for high energy beams, for lower energy applications such as SEM, electrostatic focusing is often more cost effective and compact. In fact, the electric fields are on the order of 10^6V/m in micro-scale gaps allowing for small focal lengths compared to macro-size devices, a key advantage of scaling. Einzel lenses are common electrostatic focusing structures that have been implemented in many of the above mentioned applications. In addition, electrodes are easier to integrate into the planar beam-system architecture. Hence this work exclusively deals with focusing with electrostatic lenses.

The scope of beam optics has a long history and too extensive to be covered in detail in this chapter. Section 3.1 briefly touches upon some relevant theoretical points to establish an intuitive understanding. However, analytical solutions to most beam dynamics problems are not tractable – numerical solutions are almost always relied upon: simulation results are illustrated in Section 3.3 to highlight a few focusing lens design points. The main emphasis of the work described in this chapter is to demonstrate electrostatic focusing of the Einzel lens on a Si micro-machined planar structure. The fabrication process developed and shown in Section 3.3, is important in its effort to miniaturize beam focusing systems by providing high aspect ratio, 3-layer multi-electrode structures. In principle, this fabrication process can enable a multitude of other actuating structures e.g. electrical quadrupoles and hexapoles for out-of-plane particle motion control. The testing setup is described in Section 3.2. The 3-layer Si structure is demonstrated for an Einzel lens device, the tested result of which is shown in Section 3.4.

3.1. Introduction to Theory of Transverse Beam Expansion

In reality there is really no such thing as a perfectly collimated beam: a beam of particles will expand as they propagate, even for neutral particles like photons and neutrons. The most obvious reason is that in practice, the particles emitted from a particle source, a point or a sheet source, will initially have a directional distribution in addition to an energy distribution.

In the charged particle case, particles are usually then extracted from the source region by a high electric field, which will define their general direction of propagation. In the case of charged particles, the electrostatic repulsion between same-charge particles will lead to a

continuous expansion of the beam. The next section explores beam space charge effects via the paraxial equation.

3.1.1. Paraxial Approximation & Transverse Expansion due to Space Charge

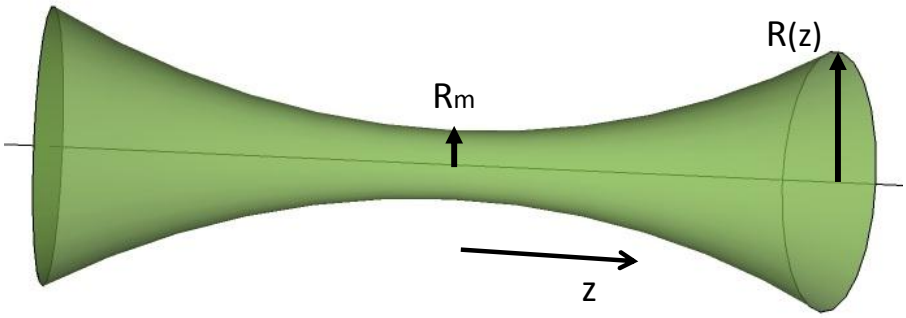

Figure 3.39 Charged particle beam propagation described by paraxial equation.

A beam in drift space is commonly described by the paraxial equation which solves for the beam envelope shape or axial radius *R*, considering focusing and expansion effects on the beam [24], [10]:

$$R'' = -\left(\frac{\phi'}{2\phi}\right)R' - \left(\frac{\phi''}{4\phi}\right)R - \left(\frac{qB_z(0,z)^2}{8m_0\phi}\right)R + \frac{\epsilon^2}{R^3} + \left(\frac{q\psi_0^2}{8\pi^2 m_0\phi}\right)\frac{1}{R^3} + \frac{K}{R} \tag{3.12}$$

The approximation assumes that the particle trajectory varies over long distances and makes small angle orbits to the axis of motion. The first 3 terms are focusing terms: the 1st is associated with acceleration, the 2nd with electrostatic focusing and the 3rd with magnetic focusing (which is not relevant to this work). The last 3 terms indicate defocusing effects. The 4th is due to emittance (ϵ) expansion due to non-parallel (non-laminar) flow of the

particles (applicable also to charge-neutral particles). The 5th is due to expansion in an axial magnetic field, which we will ignore, as we did not apply magnetic fields in our structures. In zero magnetic-field, the expansion terms are $\frac{\epsilon^2}{R^3} + \frac{K}{R}$. The 6th term is dependent on the generalized perveance parameter *K* which relates to the magnitude of space-charge effects in the beam, which only depends on the beam current, beam energy and particle mass:

$$K = \frac{qI_0}{2\pi\varepsilon_0 m(\beta\gamma c)^3} \tag{3.13}$$

The complete paraxial equation, in the general case, can only be solved numerically. Commercial software such as Opera [56] takes such space charge effects into account. As a first order approximation for charged particles of a drifting beam, one can assume laminar flow (no emittance) and only consider the *K* effect. This type of rough estimation is useful for beam setup in experiments. For a drifting beam with no external forces acting upon it (first 3 terms ignored) the differential equation becomes:

$$\frac{d^2R}{dz^2} = \frac{K}{R} \tag{3.14}$$

The solution is of the form:

$$R(z) = \sqrt{2K}\left(\frac{\chi}{F(\chi)}\right)z \tag{3.15}$$

Here, *z* is the distance from the neck of the beam. Let R_m be the radius of the beam at the waist. Then χ and $F(\chi)$ are defined as:

$$\chi = \frac{R(z)}{R_m} \qquad \text{where} \quad F(\chi) = \int_1^{\chi} \frac{dy}{\sqrt{\ln(y)}}$$

[24] gives tables of values for $F(\chi)$ and χ. From Eqn. 3.3, it can be shown that,

$$\frac{dR}{dz} = \sqrt{2Kln(\chi)} \tag{3.16}$$

$$z = \frac{R_m}{\sqrt{2K}} F(\chi) \tag{3.17}$$

To demonstrate how the above theory is used to estimate beam geometry for the device testing setup, consider a 1μA beam of 2keV electrons in the present setup to for device testing. The perveance is then 1.69×10^{-7}. From an initial aperture of 200μm or r_m=100μm, to estimate the beam diameter after 30cm of drift, Eqn. 3.6 can be used to find that $F(\chi)$ =1.74 and the corresponding $\chi \approx 1.7$. Then the beam radius is approximately 170μm after 30cm of space-charge expansion.

3.1.2. Introduction to Beam Optics for Electrostatic Einzel Lens Focusing

The physics of charged particle bending in an electric field region is often compared to that of a light beam passing through one medium to another. Just as a ray of light will bend when encountering a change in the index of refraction, a charged particle's trajectory will change between 2 regions of differing potentials V_1 and V_2 depending on its angle (α) of incidence to the normal of the equipotential surfaces there [57]:

$$\sqrt{V_1}sin\alpha_1 = \sqrt{V_2}sin\alpha_2 \tag{3.18}$$

One immediately notes the similarity to Snell's Law, and the refractive index is replaced by the square root of the potential, or particle energy. Thus this analogy is reflected in terms such as charged particle optics and equivalent lens with corresponding focal lengths, principle planes, objects and images. However, unlike light optics where the change in refraction index between two different media is often abrupt, the change in potential varies continuously across electrostatic regions in space. Hence the electrostatic lens acts as a thick lens. The difference between a thin lens approximation (used in much of light optics) and the thin lens is that the former defines the focal lengths from the plane perpendicular to the axis through the middle of the lens (*M*), whereas the latter defines focal lengths from principle planes which could be on either side of *M*. For a detailed description, see [57], [54], [58]

Lensing effects occur in the aperture between two electric potential regions as shown in Figure 3.40. This example is for a field that is accelerating. Crossing the aperture, the beam will experience both a focusing and defocusing effect. At first there is a focusing effect due to the downward component of the electric field as the beam enters the gap – a focusing effect. As it exits the gap, the electric field will have an upward component causing a defocusing effect, but the defocusing is weaker in this case than the focusing one because in the latter case, the beam is closer to the central axis, and the field is weaker there. Hence the overall effect is that of a focusing one (for the accelerating field). The opposite is true for a field that is decelerating.

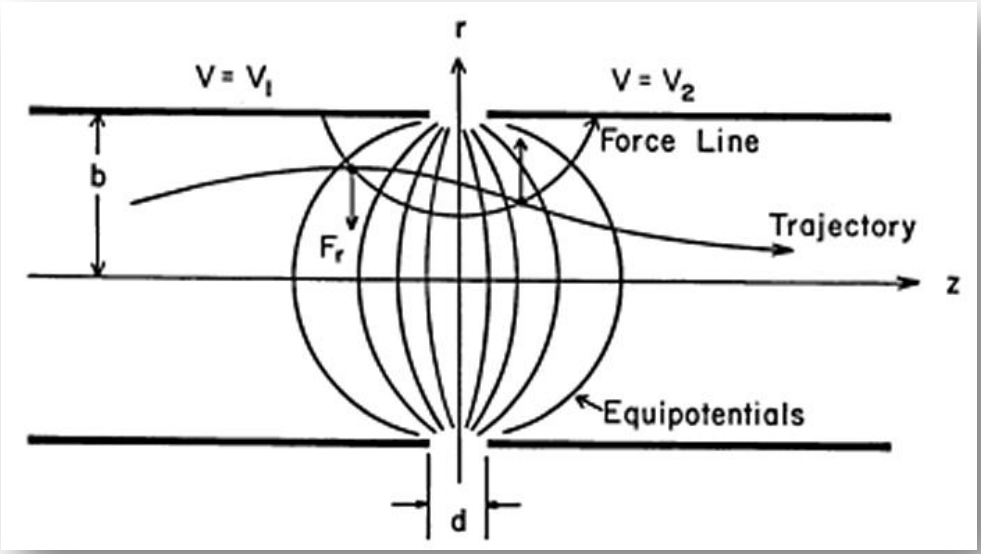

Figure 3.40 Trajectory of a charged particle through one electric lens aperture between regions of potential V_1 and V_2. Image is taken from [10].

A particle beam can be tracked in terms of its position *r* from the central axis of a guiding channel and *r'*, the derivative of *r* with respect to *z* which is the direction of propagation. Just as in light optics, the effect of an aperture, like the one above, on *r* and *r'* can be mathematically characterized by the matrix $\widetilde{M}$ such that:

$$\begin{pmatrix} r_{out} \\ r'_{out} \end{pmatrix} = \widetilde{M} \begin{pmatrix} r_{in} \\ r'_{in} \end{pmatrix} \tag{3.19}$$

Subsequent apertures and lensing regions can be modeled as consecutive matrix operations:

$$\begin{pmatrix} r_{out} \\ r'_{out} \end{pmatrix} = \cdots \widetilde{M}_3 \widetilde{M}_2 \widetilde{M}_1 \begin{pmatrix} r_{in} \\ r'_{in} \end{pmatrix}$$

See [10] for more details on $\widetilde{M}$ and its relation to focal lengths and particle energies.

It can be shown from the paraxial equations, that the focal lengths of the simple aperture lens such as that in Figure 3.40 are dependent upon the potentials V_1 and V_2 as [10] [57]:

$$\frac{f_1}{f_2} = \left(\frac{V_1}{V_2}\right)^{1/2} \tag{3.20}$$

An Einzel lens is two aperture lenses back to back. It consists of 3-electrode pairs: the middle electrode is held at a constant potential (V_{Einzel}) relative to the outer electrodes shown in Figure 3.41. The beam particles enter and leave the Einzel setup with the same energy since the two sets of electrodes on either side of central V_{Einzel} electrodes are at the same potential, which is convenient for beam device design purposes. From Eqn.3.9 it can be seen that since $V_1 = V_2$, so that $f_1 = f_2$.

Traditional Einzel lenses consist of cylindrical electrode segments which have the advantage of having azimuthal symmetry. However in the planar architecture, which this work is concerned with, the Einzel lens segments are rectangular stacked electrodes. For particles in the middle of the channel formed by the electrodes, away from the outer fringing fields, simulations for this geometry for the lensing action and particle trajectories can be relied upon.

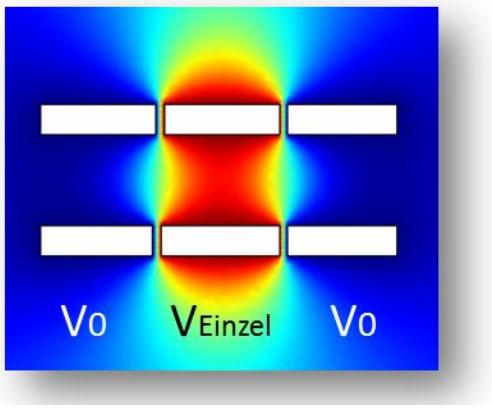

Figure 3.41 COMSOL simulation of Einzel lens showing electric potentials in color.

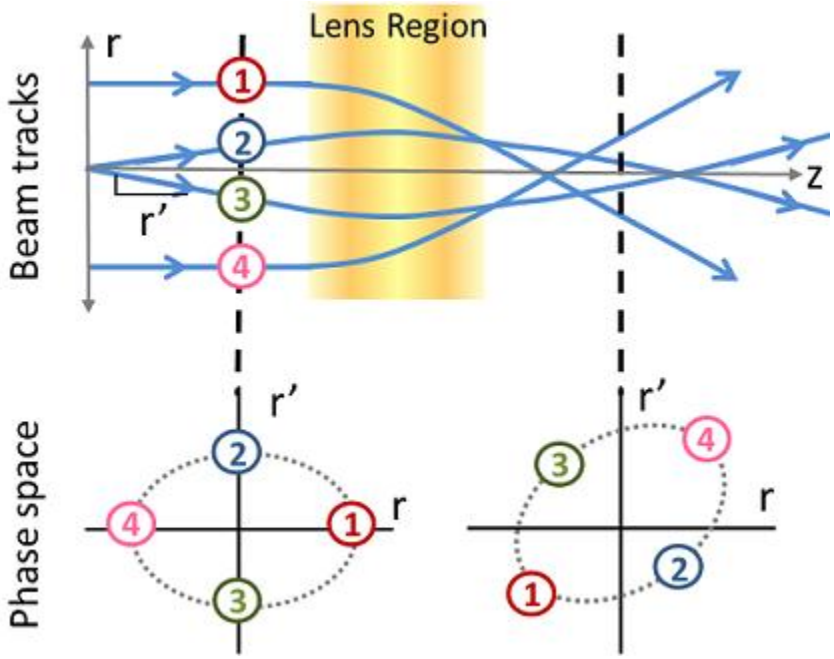

Figure 3.42 Illustration of the effect of electrostatic lensing on beam trajectories, and the effect on particle phase space. Lenses change the shape of the phase space ellipse but the ellipse area (emittance) remains the same.

For any lensing system, the beam can be traced in terms of *r* and *r',* as shown in Figure 3.42. A plot of *r* and *r'* is the phase space of the beam. All particles in the beam should lie within the trace space area of the ellipse in phase space. The shape of the ellipse can change as shown in the figure, but the area should remain the same for a beam where there is no net acceleration. The *area* of the ellipse is associated with a beam parameter called emittance ϵ as: $\epsilon = \frac{Area}{\pi}$. Hence for an Einzel lens, where the particle energy at the entrance is the same as that at the output, the emittance should remain the same [10]. If however, there is net acceleration, the emittance may change. The envelope of a beam can then be traced with the corresponding phase-space ellipses, illustrated in Figure 3.43.

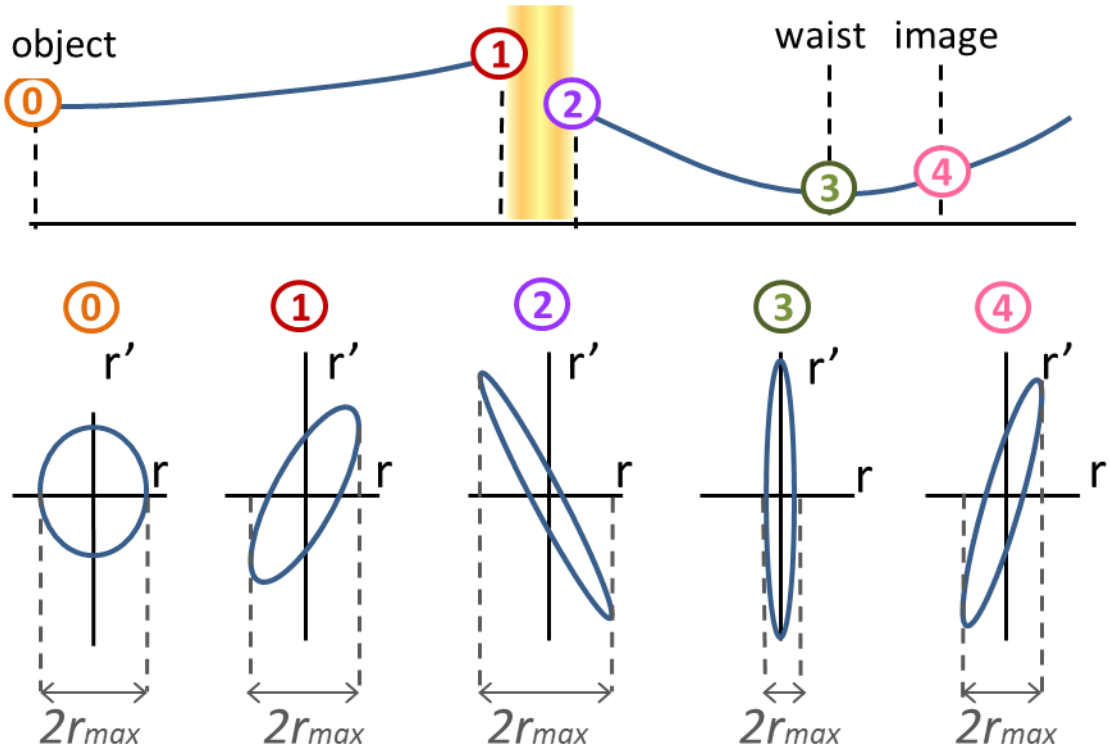

Figure 3.43 The beam envelope (top) is changed through an lens (yellow region). The phase space ellipses corresponding to the numbered envelope points, also changes (bottom). The ellipse of the image is not necessarily upright. Beam spot width is $2r_{max}$ in each case

Although it is important to have an intuitive theoretical understanding of beam envelope variations through lenses, in practice beam tracks are simulated in software such as SIMION [59] and Opera [60]. Simulations can better predict the effect near edges where the potential gradient is not smooth, as well as space charge effects. (SIMION does not take space charge into account). Figure 3.43 also illustrates the fact that a highly focused beam spot with small beam radius r_{max}, (at point number "3"), also exhibit high divergence or large r', whereas a larger beam spot may correspond to smaller divergence angle (at point number "0"). Simulations can aid in the prediction of the phase-space ellipses, such as points in between beam actuating components e.g. accelerator and lenses. In this way, simulations may assist in beam actuator systems design to control transverse beam expansion.

In this work, simulations of charged particle trajectories are solely implemented in SIMION software. Section 3.3 discusses some focusing simulation results for a cascaded Einzel lens. The methodology can be expanded to more complex systems.

3.2. Design Considerations

Using SIMION simulations, the focal strength behavior of the planar Einzel lens can be studied with respect to the electrode geometry and the voltages applied to them. Below are some basic characteristics for Einzel electrodes consisting of strip segments on a substrate (not cylindrical as in the traditional implementations):

i) The focal strength increases with V_{Einzel}, the potential on the middle pair of electrodes as compared to the outer ones. Figure 3.44a) shows that as V_{Einzel} increases, the focusing strength increases to engender a small beam spot waist (or r_{max}), while also evoking a greater divergence from that waist (higher r').

ii) The higher the ratio of the segment length to channel width ratio A/D, the greater the focusing strength as shown in Figure 3.44b). In other words, larger the gap size the weaker the focal strength and the longer the focal length.

iii) Since the lensing affect occurs at the gaps between two segment pairs, by cascading a series of Einzel lenses together (Figure 3.44c) the focal strength may be increased, but may also exacerbate aberrations.

For initial proof of concept of the planar Einzel lens, an 8-gap Einzel was chosen (instead of 2) to increase the focusing power, in order to alleviate the requirement on the amount of high voltage that is needed to be supplied as V_{Einzel} . Figure 3.45, Figure 3.46 and Figure 3.47 shows

the focusing trajectories of beams in the 8-gap electrostatic lens. The shape of the focused beam very much depends on the initial input beam phase-space characteristic. For clarity, ideal parallel and divergent particle tracks are shown separately: Figure 3.45 shows parallel beams, with no *r'*, only *r* values, entering the channel; in Figure 3.46 the beams all ideally start in the channel center, with only *r'* values in phase-space; in Figure 3.47 divergent beams are shown with different starting points along *r*. A cartoon of phase space illustrates that beams outside the phase-space ellipse is unstable – they are lost at the channel walls. Therefore one notes that the phase space ellipse and emittance are all dependent on electrode geometry and must be simulated for each design.

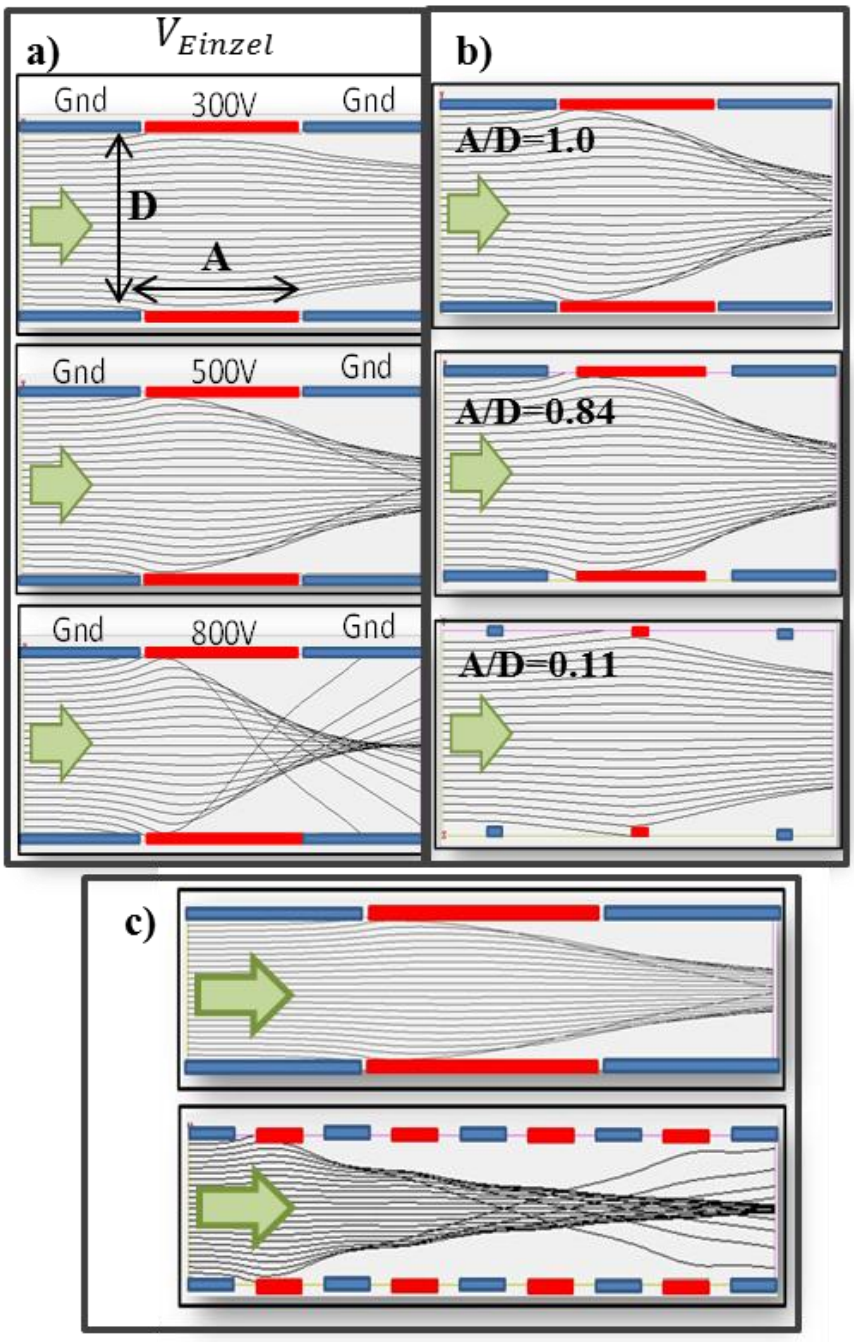

Figure 3.44 Design considerations: Electron beam tracking simulations in Einzel focusing entering from the left, for a) various V_{Einzel} for constant A/D=1; b) various Einzel A/D, constant V_{Einzel} = 500V; c) a comparison of 3 gaps versus 8 gaps over the same distance.

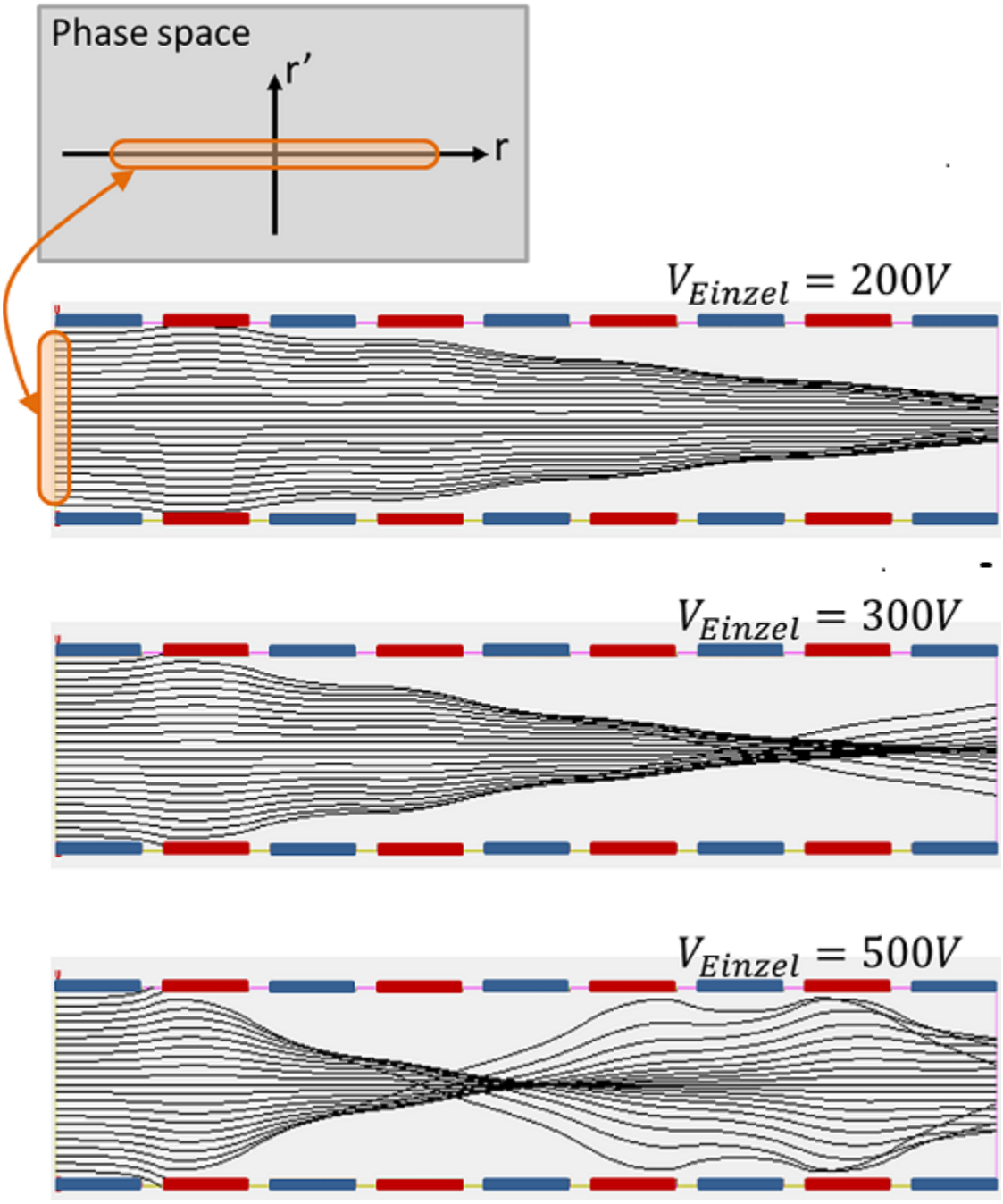

Figure 3.45 Focusing through an 8-gap Einzel structure for input particles with no initial divergence. In phase space (top), the particles all lie along x-axis. Focal powers increase with V_{Einzel} which also increase aberrations.

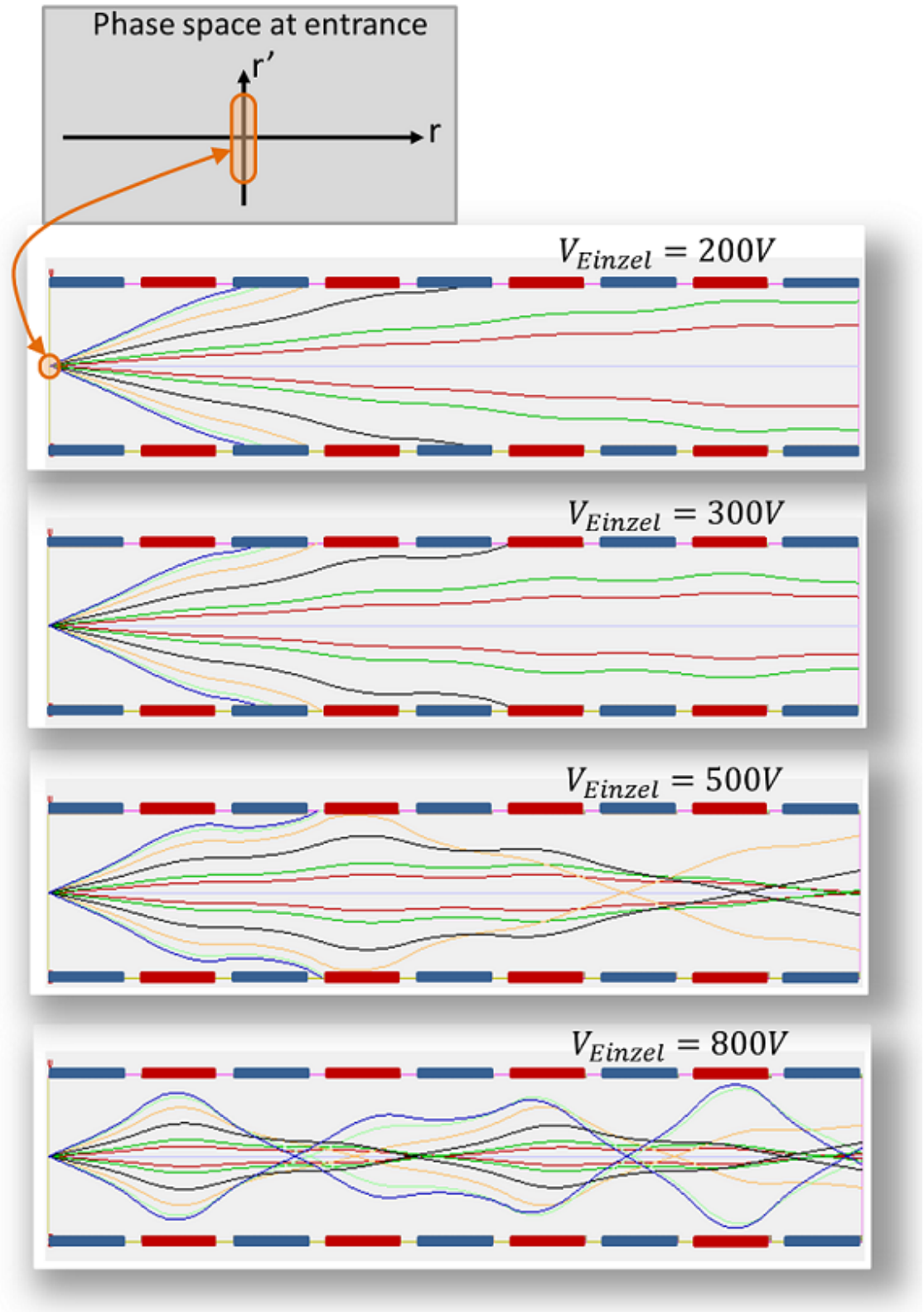

Figure 3.46 Focusing through an 8-gap Einzel structure for input particles all starting at the channel center, with various initial divergence. In phase space (top), the particles all lie along y-axis. Focal powers increase with V_{Einzel} which also increase aberrations.

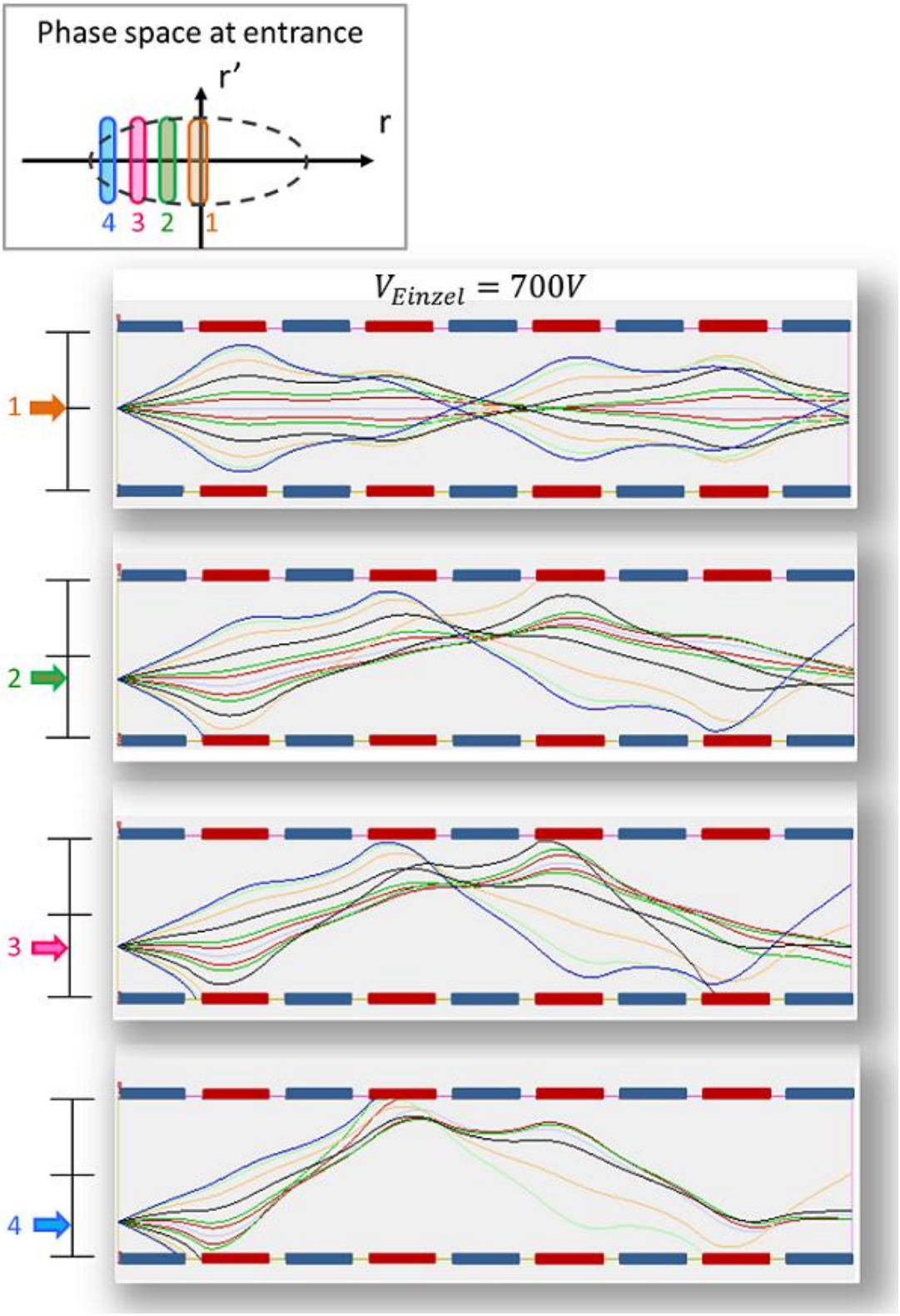

Figure 3.47 Particle trajectories through an 8-gap Einzel structure for input particles with various initial divergence all starting at the same point, which varies along the channel width. Corresponding phase-space for each case is color-coded. V_{Einzel} is the same in all cases.

An example of an Einzel design to be tested as a proof of concept is shown in Figure 3.48 with given dimensions. Gap sizes range from 0.5mm to 1 mm.

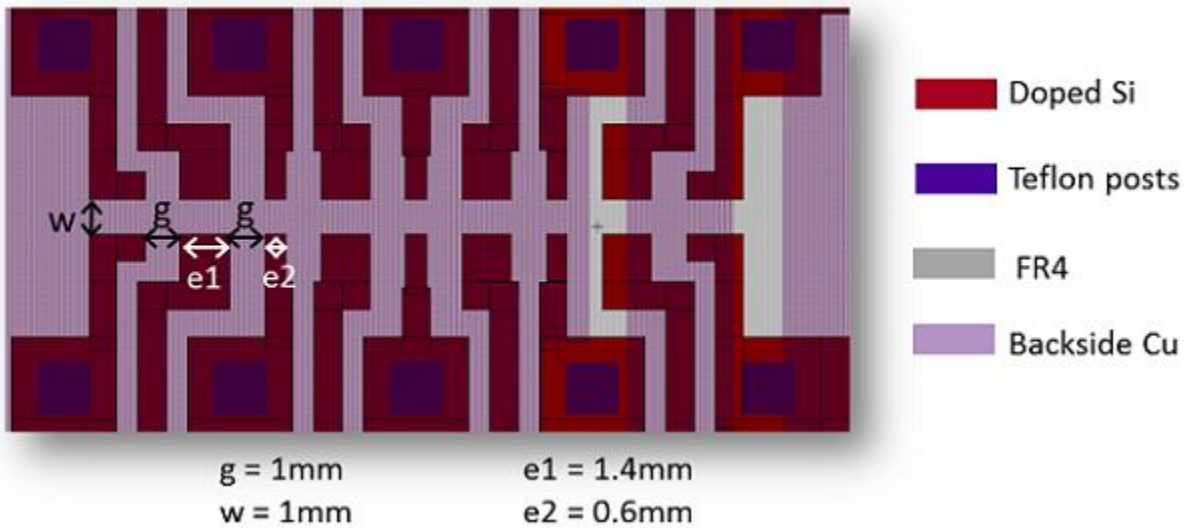

Figure 3.48 Example of 8-gap Einzel lens layout with given gap and electrode dimensions.

3.3. Testing Setup & Simulated Setup

3.3.1. Testing Setup

The testing setup for the Einzel lens is shown in Figure 3.49. The 3-layer stack Einzel lens, the DUT (device under test) that is adhered to a PC board, is electrically supplied through wirebonding to the board. Vacuum compatible wiring is soldered to the PCB and connects through vacuum feedthroughs. The PCB in turn is tightened down to a grounded Al holder, to be mounted onto a motorized x-y-z stage which can move with minimum step size of 50nm. The stage is used to align the sample with respect to electron beam that enters from the left in Figure 3.49. The beam's trajectory is therefore in-plane with the PCB substrate. A phosphor screen is placed 20cm from the front of the DUT. The beam is first focused onto the screen or

BeO disk by adjusting the electron gun, without applying V_{Einzel}. An image is captured by a camera from behind the screen (Figure 3.50). From the image, the beam diameter is extracted by counting the number of pixels above a cutoff brightness.

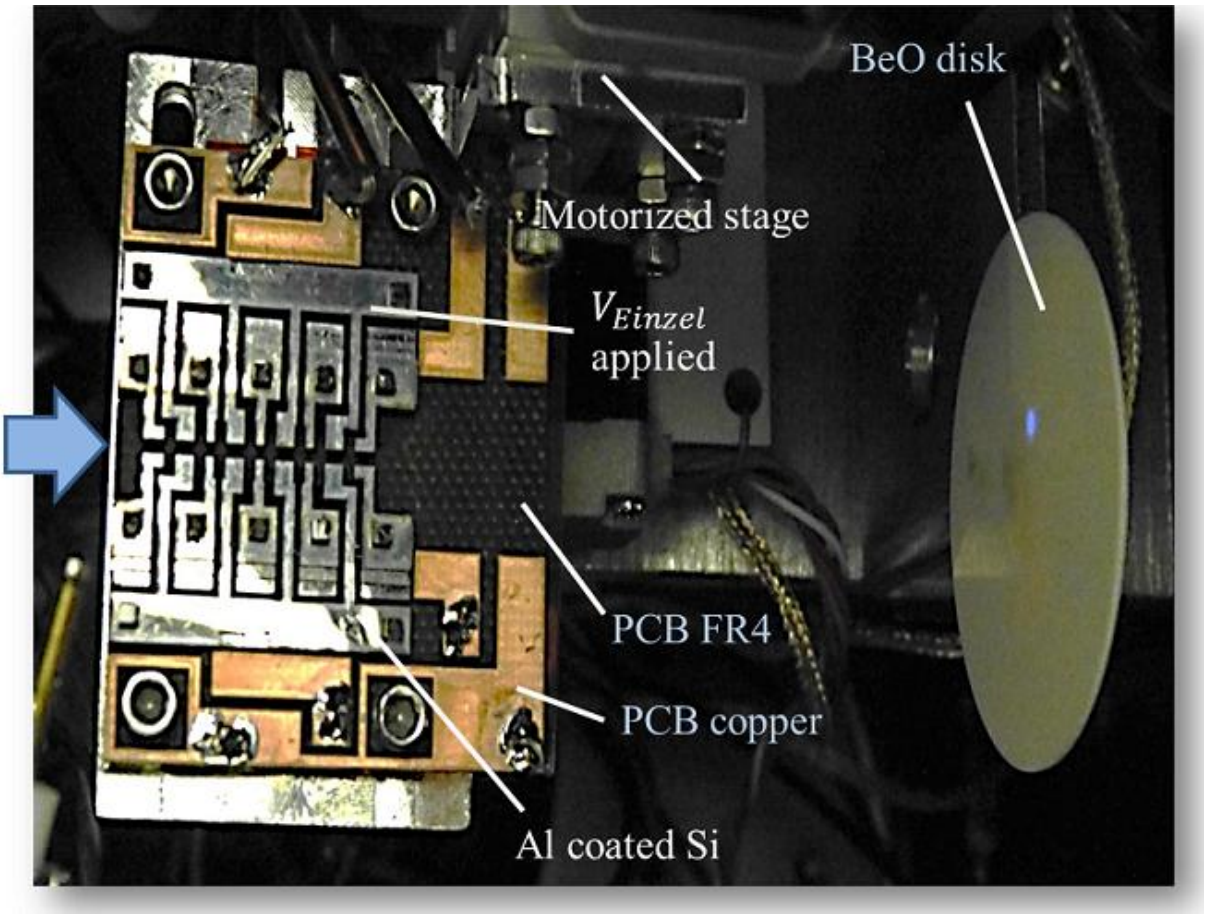

Figure 3.49 Photo of testing setup for 3 Si layer Einzel lens. Beam enters from the left, and after actuation, is detected optically on the fluorescent screen on the right. The chamber window (not shown) is situated behind the screen. A high sensitivity camera images the beam spot on the screen through the window. An example of such an image taken is shown in Figure 3.50.

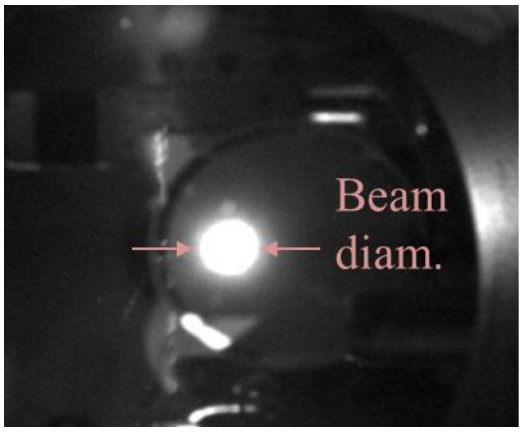

Figure 3.50 Fluorescent screen from setup in Figure 3.49 is imaged with high sensitivity camera from the back of screen through a vacuum chamber window.

When V_{Einzel} is turned on, the imaged beam spot will expand, as the focal length changes (see simulation tracking in Section 3.3.2). Hence the experimental data thus obtained is really a reverse focusing effect. However the defocusing behavior of the lens will still demonstrate its focusing capability.

SIMION simulation of the particle beam track will be shown in Section 3.3.2 for the above mentioned experimental setup geometry. Then in Section 3.5.2, the simulated result and width data of the imaged beam spots, with respect to V_{Einzel} will be compared for the defocusing effect – the smallest beam width occurs when V_{Einzel} =0, and grows as V_{Einzel} increases/decreases.

The beam is chosen to be focused to its smallest waist at V_{Einzel} =0 first, is due to the practical consideration of initially aligning the beam into the channel. In the course of experimentation, it was discovered that the electron beam caused a luminescence effect visible to the eye when it impinges on the FR4 dielectric of the PCB. There is also a faint luminescence when the beam collides with the Si structure of the DUT.

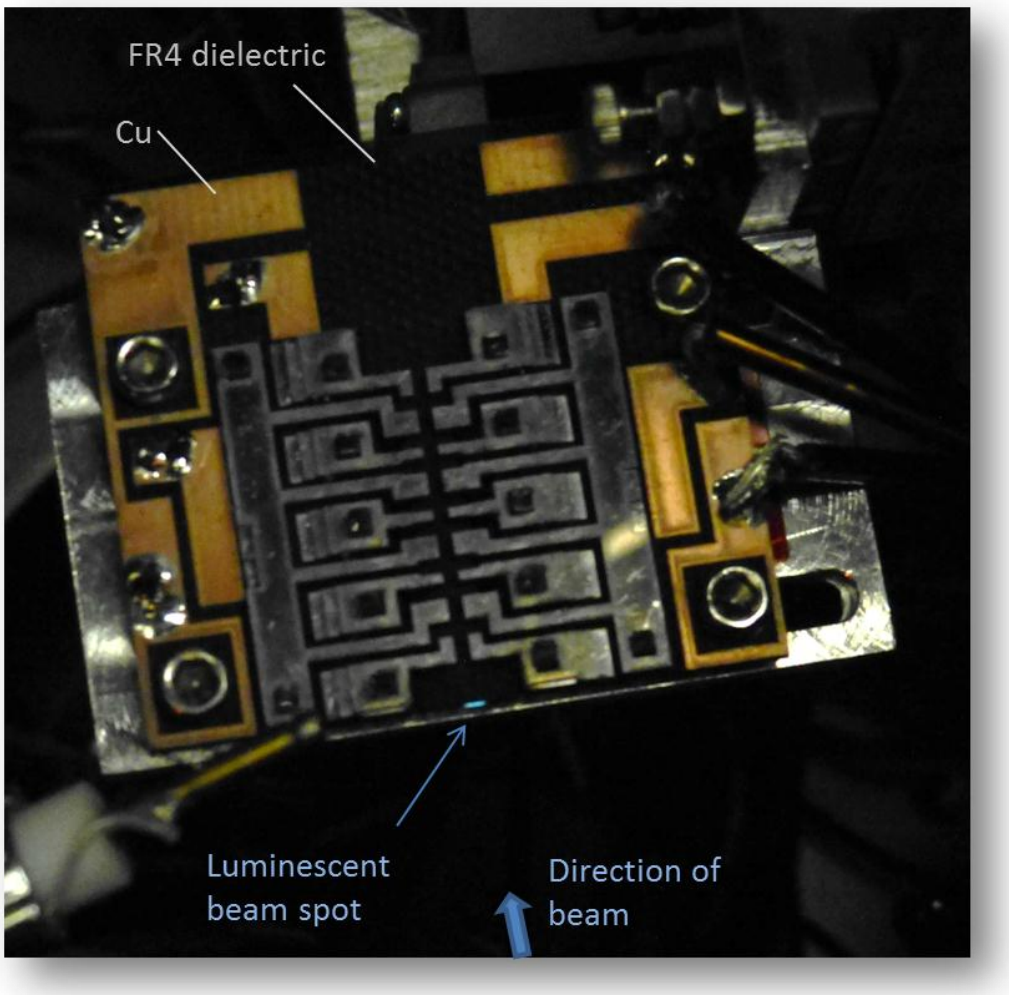

Figure 3.51 Under dark room conditions, a luminescent spot is visible by eye when the electron beam impinges onto the FR4 dielectric. The luminescence is fainter, but still visible when the beam impinges on Si.

No visual effect was observed when the beam targeted the PCB copper or the aluminium holder. Luminescence from the FR4 was noted to be the brightest. This optical phenomenon greatly facilitated the alignment of the invisible electron beam into the Einzel lens channel. If the beam was made to skim the surface of the FR4, the track was visible and hence helped to determine the beam tilt angle with respect to the substrate. The blue glow is thought to be a result of cathodoluminescence. (See Section 4.3).

3.3.2. Simulation of Actual Setup

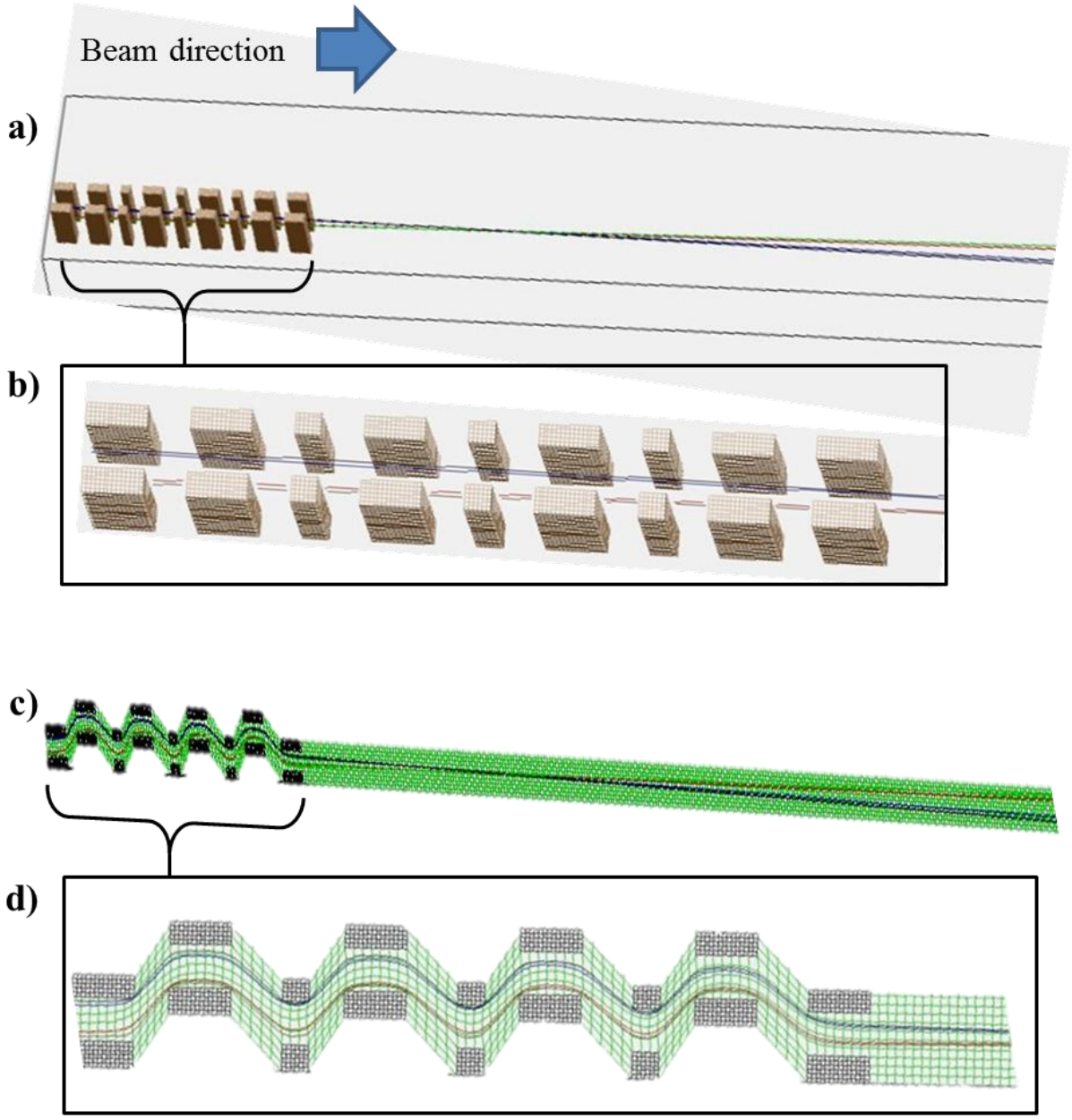

Figure 3.52 SIMION simulation work space (to scale): a) electrode geometry mimicing actual device and setup with screen placed 20cm from the front entrance of the electron column. b) Zoom-in of 8-gap Einzel lens with beams tracks propagating from left to right. c) Topological representation of electric potential for the geometry in a). This example shows potentials at V_{Einzel} = 300V. d) Zoom-in on the lensing section of c).

Figure 3.52 shows SIMION beam track simulations for the actual experimental geometry. The electrode geometry is as designed in Figure 3.48. It takes into account an initial convergence of the beam (at V_{Einzel}=0) due to focusing by the electron gun to the screen 20cm from Einzel entrance. The focal point is shifted as V_{Einzel} changes. Figure 3.53 plots the simulated change in focal distance as measured from the Einzel entrance, compared to focal length at V_{Einzel}=0.

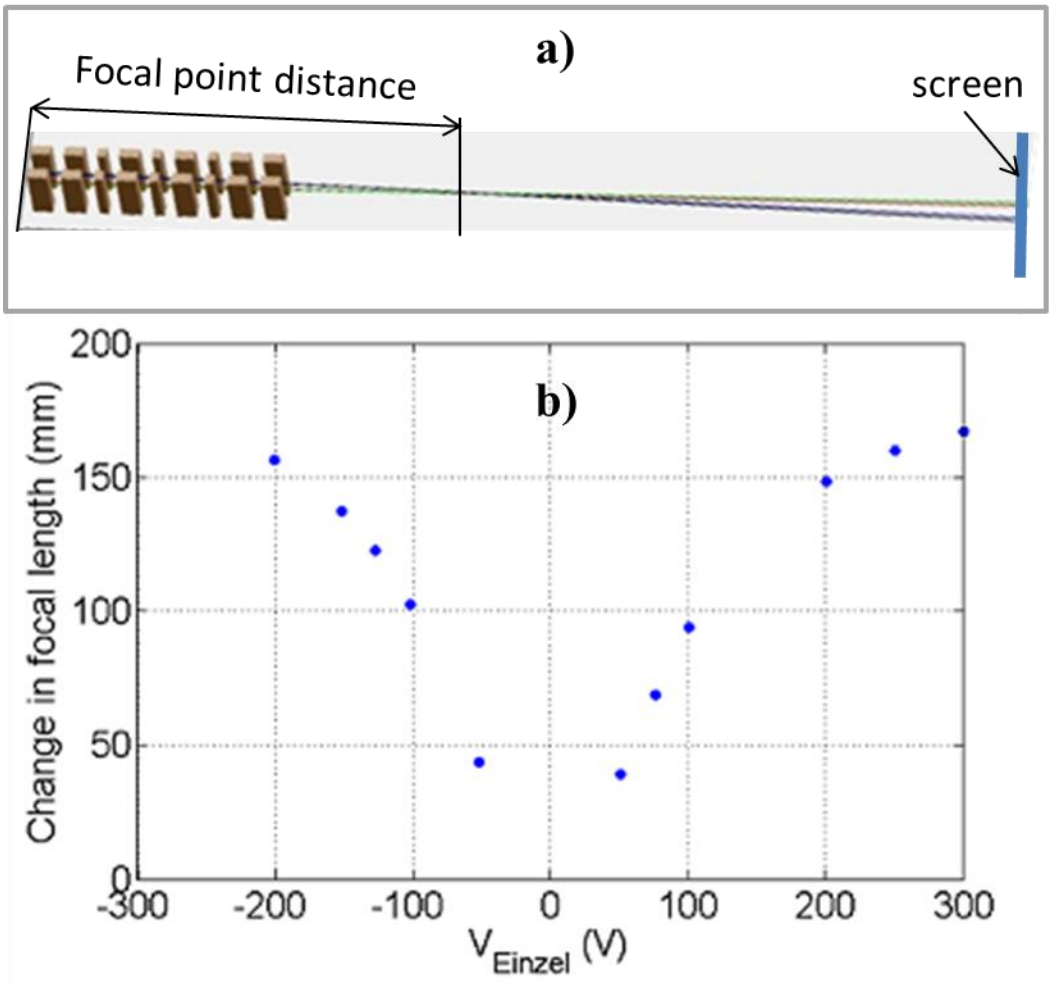

Figure 3.53 Simulation of actual Einzel and setup: a) Beam is focused and aimed at an imaginary screen 20cm away (V_{einzel} =300V); b) Focal distance change vs. V_{einzel} compared to V_{einzel}=0, measured from front of lens as shown in a).

3.4. Fabrication: 3 layer Si stacking & Laser cutting

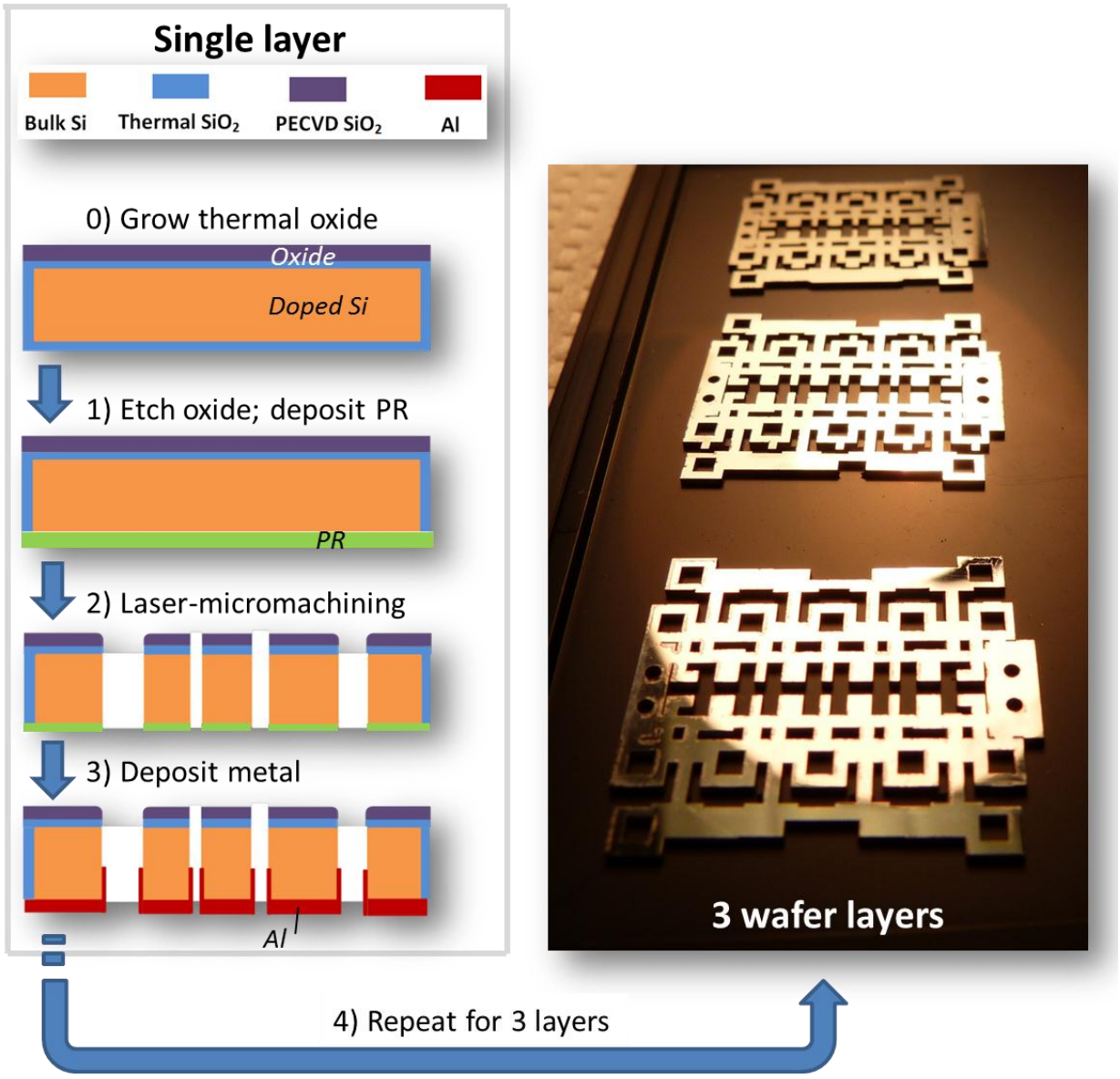

Figure 3.54 Process flow for single layer of doped Si. Photo on right shows 3 layers fabricated, which are similar expect for cut-out regions to allow for wire bonding access.

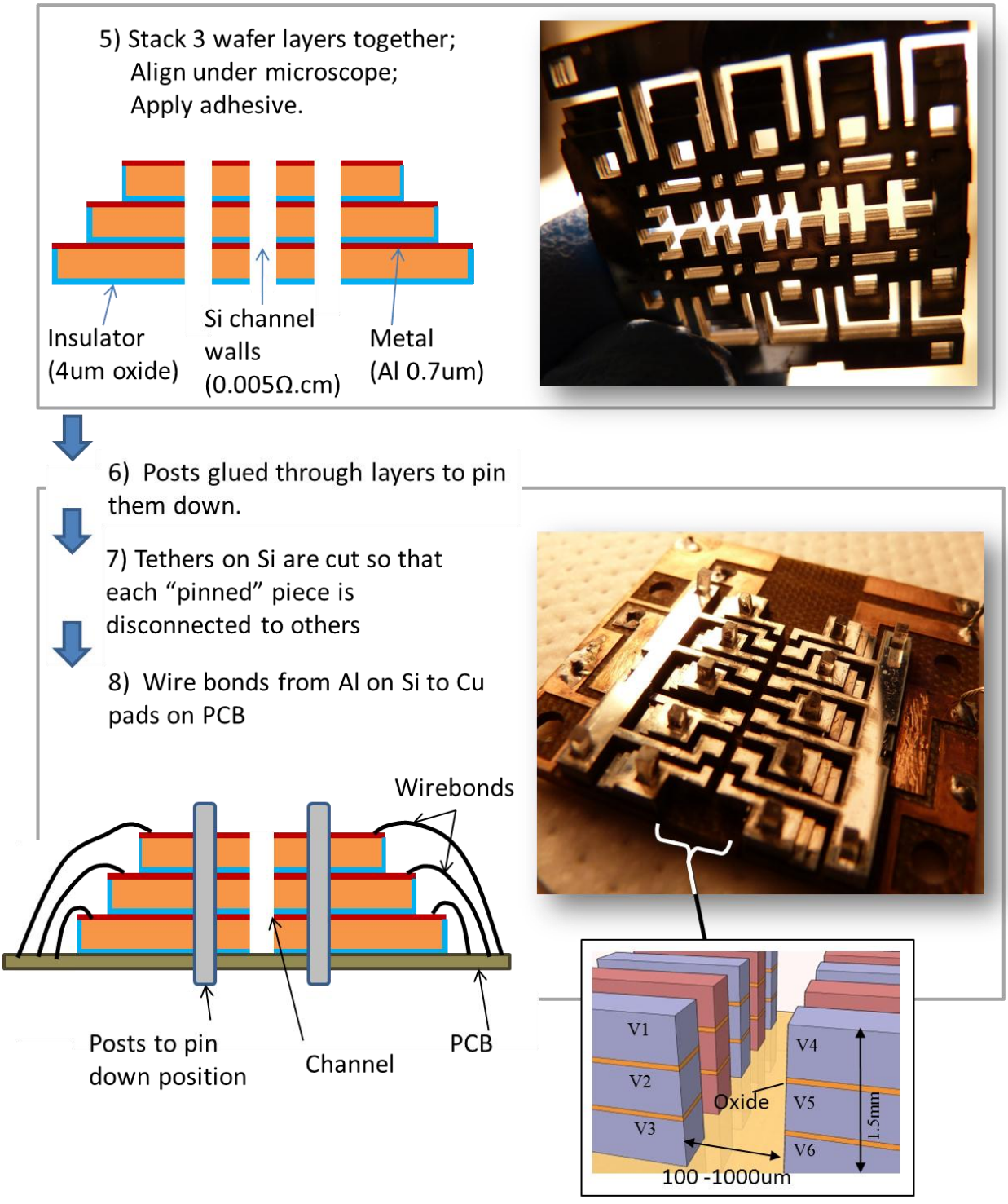

Figure 3.55 Assembly process of 3 patterned layers, and adhering to PCB.

The fabrication process for one layer of Si is illustrated in Figure 3.54(steps 0-3). The Einzel electrodes are patterned by laser cutting through the 0.5 mm thick wafer, with photoresist protection on top, using an LPKF ProtoLaser U laser machining tool (Section 4.7). Solid silicon tethers are left between the silicon islands to ensure relative alignment and ease of handling. Cleaning of the laser-created silicon dust is done using water cleaning. After cleaning, three layers are stacked together for high channel aspect ratio in step 4. In the assembly process (Figure 3.55) the stack is adhered to a bottom PCB layer (step 5). Insulating alumina posts are inserted and adhesively attached through all three silicon layers to help pin the stack to the PCB, before the tethers between electrodes are cut, so that each electrode is electrically insulated from the others (Figure 3.56). Wire bonds from the "steps" of the exposed lower layers are bonded to PCB for electrical contact.

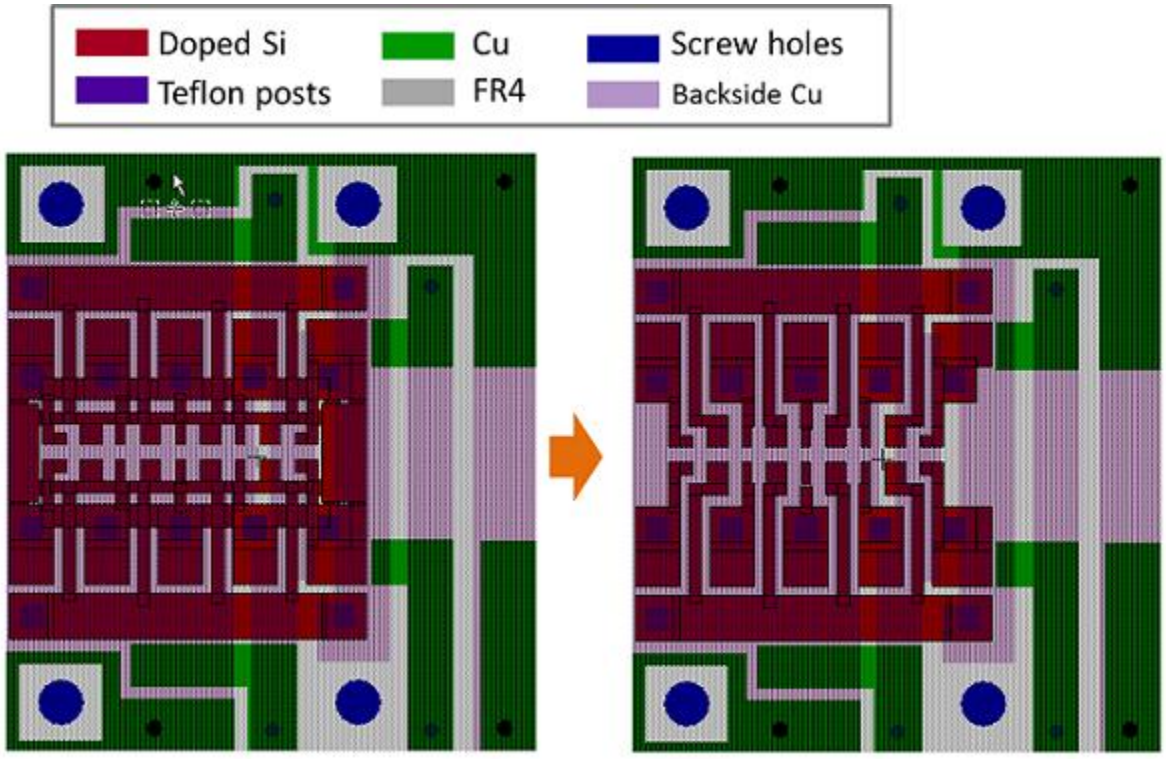

Figure 3.56 Tanner layout illustrating tether-cutting of Si (from left to right) on the PCB.

3.5. Fabricated Devices and Results

The final assembled device is shown in on the bottom right photo in Figure 3.55. A three layer Einzel lens with a channel width of 1mm, which can be made as small as 100µm if desired. As shown in the illustration, each of the layers of each electrode can be addressed independently. For this device, electrical breakdown occurred at 2.2kV in air, primarily at the sharp corners of the electrodes. In experimental vacuum of 10^{-5}-10^{-6}Torr, breakdown was not observed at 2.2kV, by which point we are equipment limited.

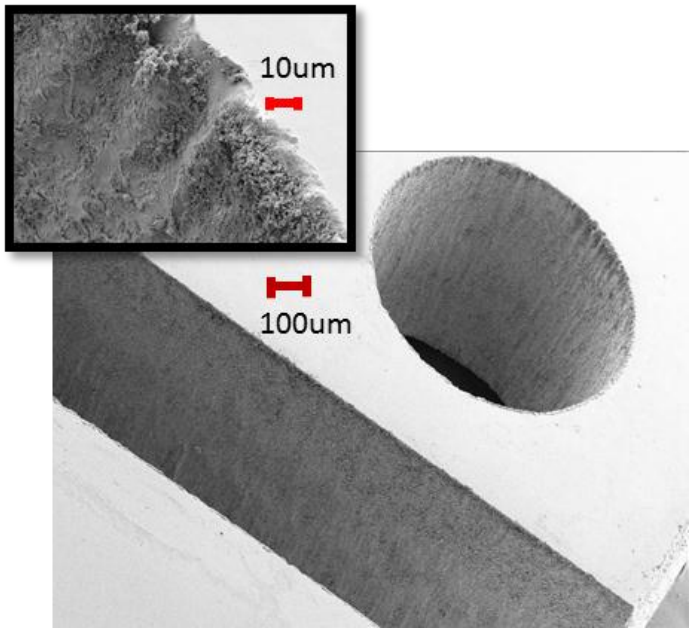

Figure 3.57 SEM images of laser-cut through-wafer Si features.

3.5.1. Surface Roughness

From the SEM pictures taken of the laser cut Si structure sidewalls (Figure 3.57), it can be seen that the surface roughness is on the order of 10 µm. For feature sizes on the order hundreds of microns, this roughness is approximately 1%.

3.5.2. Beam Spot Size Measurements

The simulation and experimental change in beam diameters for a screen 20 cm away from the lensing structure entrance are compared in Figure 3.58, where quadratic fits are applied. As expected the beam diameter is minimum at V_{Einzel} =0 since that is the focused spot from the electron gun: Figure 3.58 shows a reverse focusing effect. The fits only differ in a y-shift of about 1mm, mostly due to the fluorescence spot measured on the screen spreading over time. This fluorescent spot growth effect was observed for all cases. Despite this measurement artifact, the phosphor image data follows the simulated trend for this Einzel geometry.

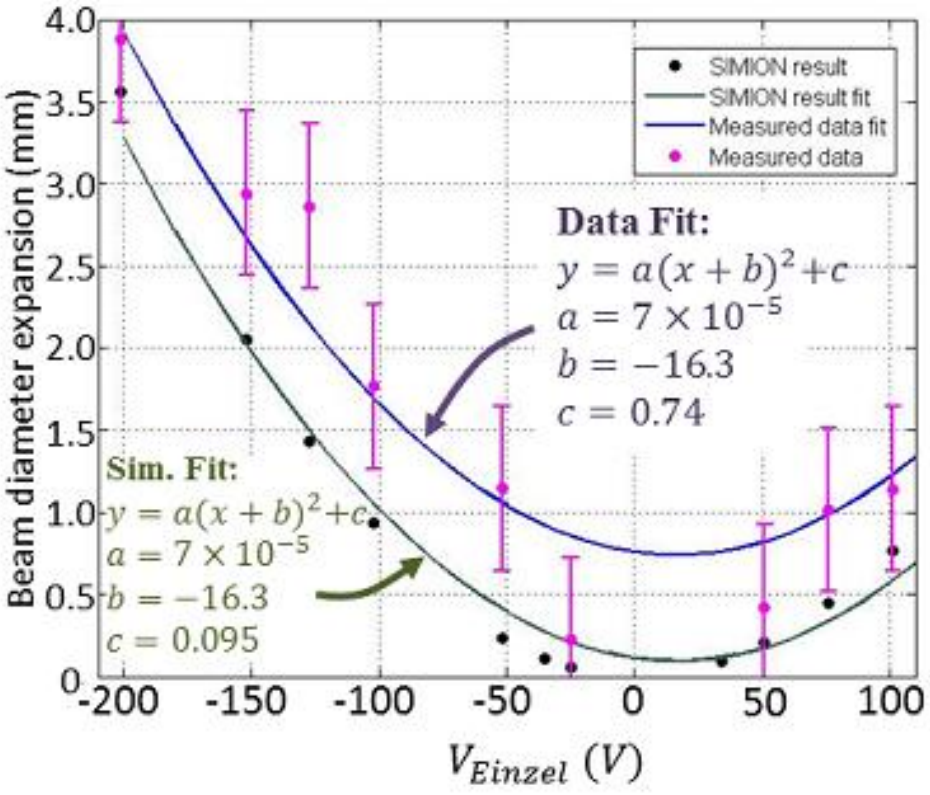

Figure 3.58 Simulated (black) and measured (purple) beam diameter expansion as a function of V_{Einzel} , with fitted curves which differ only in a vertical displacement constant. Simulated and measured fit data are shown with green and blue, respectively.

There may be substantial charge build-up on the phosphor screen from the electron beam in the non-conductive phosphorous material and the quartz plate on the back plane if it is not sufficiently grounded. The photon spot size captured by the camera may be larger than that of the actual electron beam spot. Upon impact into the phosphor material the electrons may suffer multiple collisions and be scattered or spread within the screen, causing the area of emitted light to be larger than the original electron beam spot. In addition, the emitted fluorescent light may experience diffraction within glass back plane which is of finite thickness, to cause the optical beam spot measurement to be greater than the actual electron beam.

3.6. Summary and Future Direction

The work described in this Chapter is preliminary proof of concept for the planar electrostatic lens. As multi-layer electric addressing of the electrodes is made possible, the next steps should include testing out-of-plane focusing. Presently the oxide thickness is 4μm, and since a high potential difference of up to hundreds of volts may be applied between layers, this oxide thickness should be made as thick as possible.

Characterization and optimization of the shape of the Einzel electrodes themselves should be explored. Figure 3.59 shows the effect of a wedge shape on the focusing power of the 3 segment lens, for an ideal parallel beam. The focusing power is taken in this case as directly related to $\frac{W_{in}}{W_{out}}$. The addition of the wedge is seen to diminish this parameter and hence shorten focal length. It is noted that a wedge that is opening up shows stronger focusing power than a

closing wedge. The distance of the beam from the electrodes as it passes through the gaps may greatly influence the resulting focal power and beam divergence. Optimization of the electrode shapes may therefore help reduce the total lens length and V_{Einzel} needed for a desired focal distance.

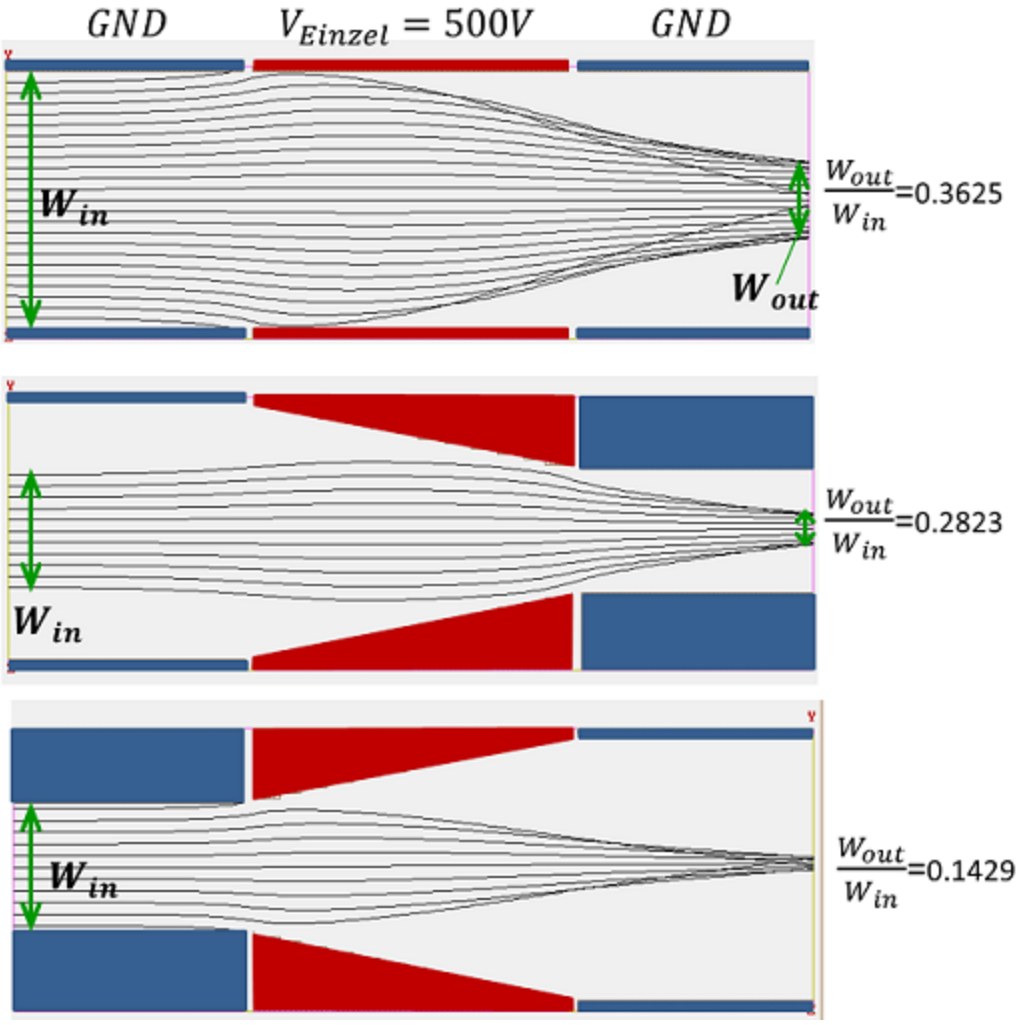

Figure 3.59 Effect of Einzel electrode shape on focal strength, measured by the ratio of entrance and exit beam diameters. In all cases the middle electrode s kept at 500V with respect to outer ones.

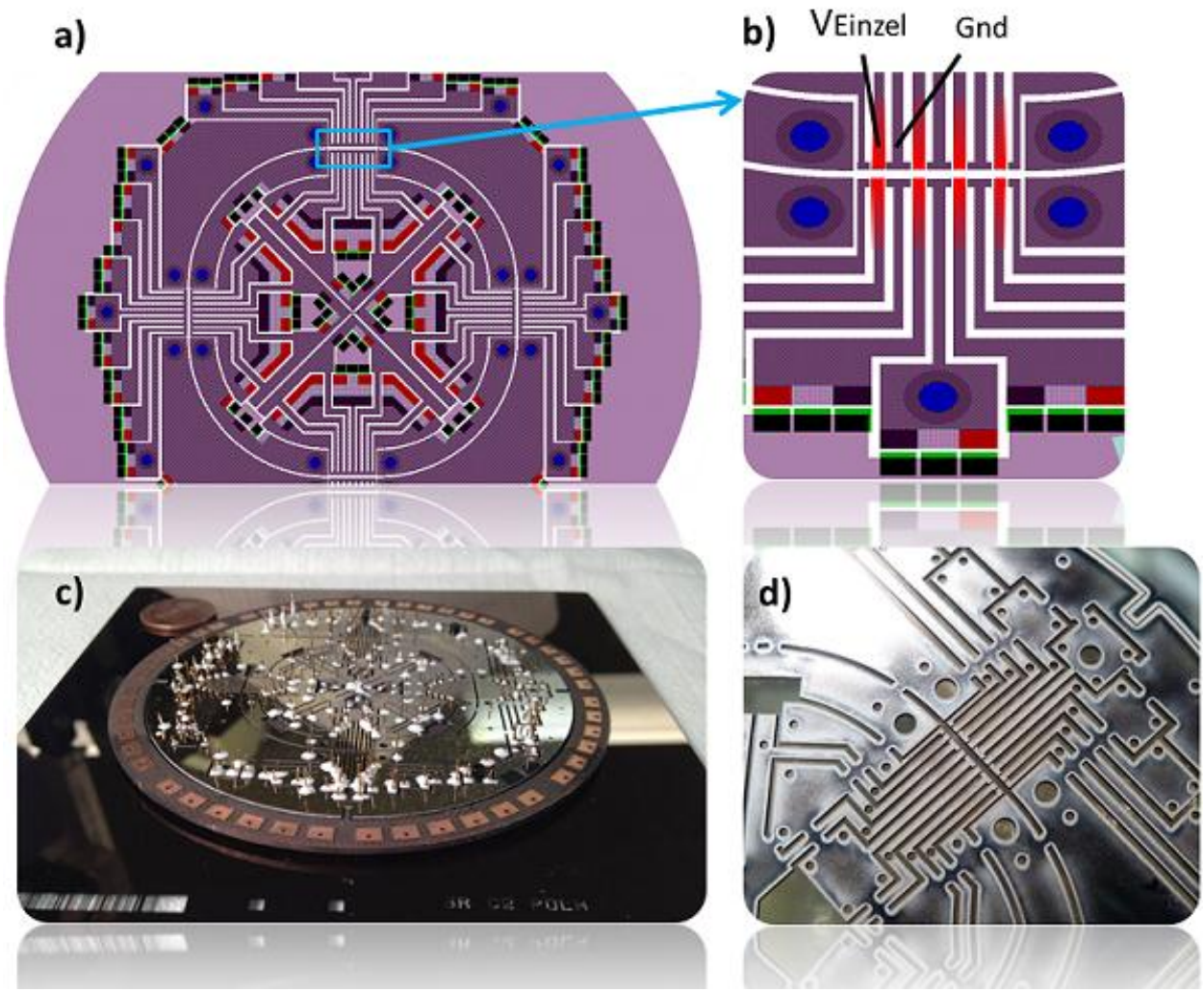

Figure 3.60 Development of a storage ring with Einzel lenses around the ring. a) A layout of storage ring with addressable Einzels, accessible via tiered regions (black, light purple, red); b) Layout zoom-in on Einzel segment; c) Photo of fabricated Si device assembled on PCB and adhered with alumina posts; actual device completes 270 degree curve to allow room for injection channel; d) Zoom in of photo on fabricated Einzel region before assembly (bottom layer Si device).

Eventually the goal is to integrate the Einzel into a whole beam actuating system. Figure 3.60 shows the preliminary efforts to incorporate four Einzel lens in a storage ring structure which aims to keep the beam in a circular path and minimizing flux loss. The layout is a top view of the 3 Si wafer layers, each accessible by cut-away regions as illustrated before in Figure

3.55a) and b), by wirebonding to Cu pads defined on the PCB. The first such fabricated Si whole wafer device, laser-cut, is shown in Figure 3.55 c) and d). The gap sizes range from 150 μm to 750 μm. The ring was designed to test 2keV electron beam curving for 270^0.

Using the simulations tools such as SIMION, the phase-space ellipse of the beam could be tracked throughout the beam actuating system (the concept as shown in Figure 3.5). In fact, the degree of focusing in practical terms, should be decided by the channel width of the component the beam would be passing through: too much focusing may result in a unnecessarily small beam waist, but a large diverging angle which may not be desired.

In summary, we developed a fabrication process for a micron-scale Einzel lens that allows electrical addressing of multiple layers for in-plane focusing of the electron beam. The device structure enables further size reduction for high density of electron or other charged particle beams. The projected beam currents are sufficient for applications such as electron lithography, SEM, and x-ray generation. The miniature Einzel lens is a building block that will help realize more complex integrated electron beam manipulating systems such as electron beam systems and accelerators for x-ray sources.

4. PRACTICAL ASPECTS OF MINIATURE CHARGED PARTICLE ACTUATOR TESTING

The experimental testing described here was accomplished on Ar ion beams to demonstrate the concept of beam actuation. We also actuated electron beams for the possible applications of x-ray generation and electron-beam lithography. This section describes both a "preliminary" testing setup for first experiments, as well as a newer setup with enhanced volume and testing capabilities. The author assembled both these setups from commercial components and custom designed units. Machine drawings of the metal pieces produced, and the chamber schematics with dimensions are shown in Appendix B.1.

4.1 Vacuum Chamber I

The first argon-beam experiments were carried out in a relatively smaller chamber that accommodated a vertically mounted ion gun, and a vacuum pumping station at the bottom (Figure 4.1). The setup is shown in Figure B.1.1 in Appendix B.

Argon gas (research grade) is fed into the NTI 1407 Ion Gun [61] which is capable of producing a beam diameter from 50μm to 100μm with the energy range of up to 5keV. A leak valve allows the gas to enter the ion gun chamber in controlled quantities, and the ionization chamber pressure is kept around 0.1 -1.0 mTorr, forming a plasma. The ionized Argon gas is primarily of the Ar^+ species, which are extracted from the ion gun into the vacuum chamber (Figure 4.2). The working distance, or the focal spot of the ion beam, can be adjusted to be up to 200mm [62], although a working distance of 80-100mm was used for this work. The ion gun is differentially pumped by a turbo pump (Pfeiffer Vacuum) to maintain a plasma and a UHV

section.

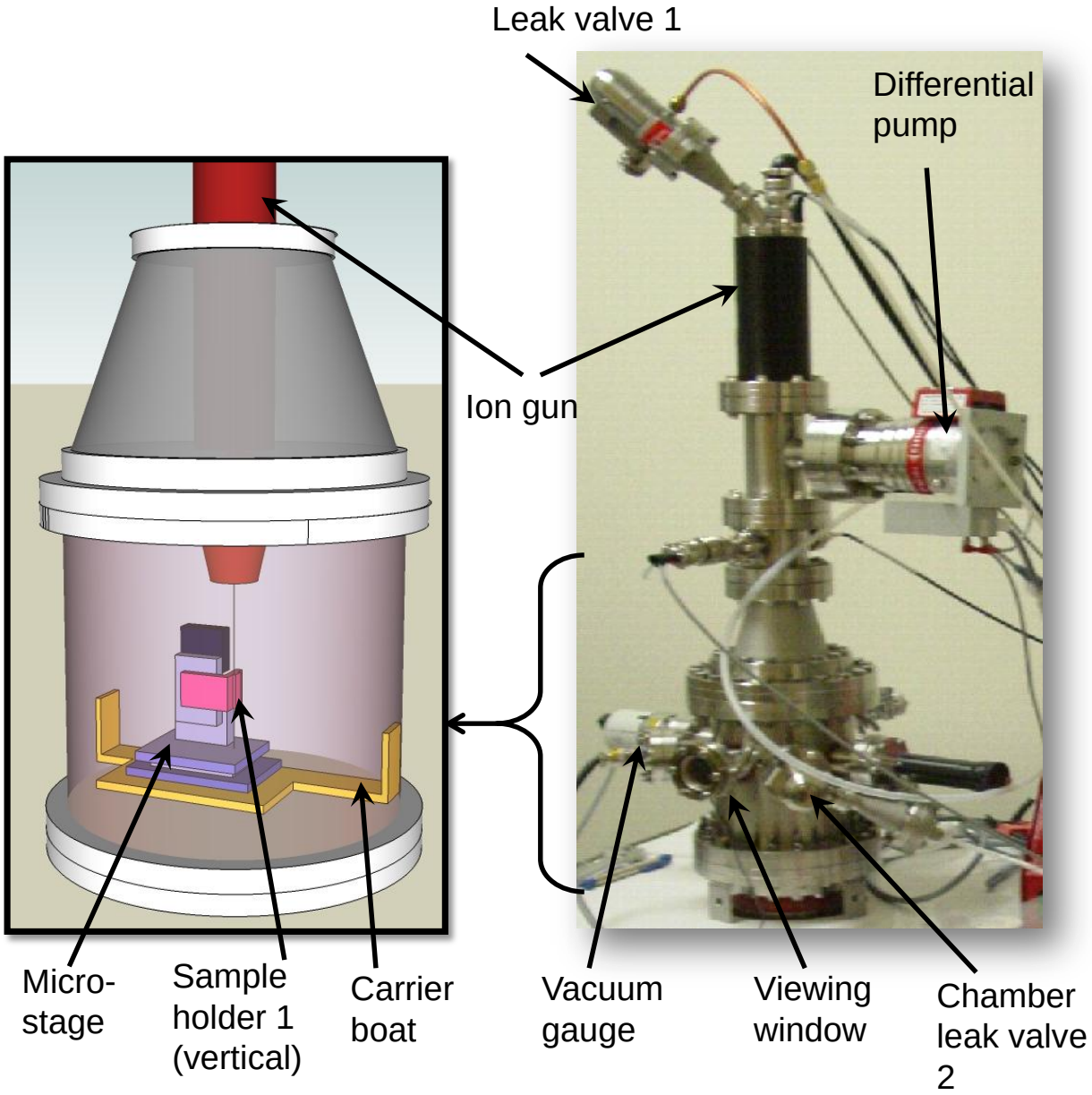

Figure 4.1 First vacuum chamber setup for Ar beam testing, provided by ion gun from the top. The sample is held by holder 1 vertically below beam and is positioned by moving stages. Stages are carried by machined "boat" piece. Vacuum pumping is done from below chamber. See Appendix B.1, for more details.

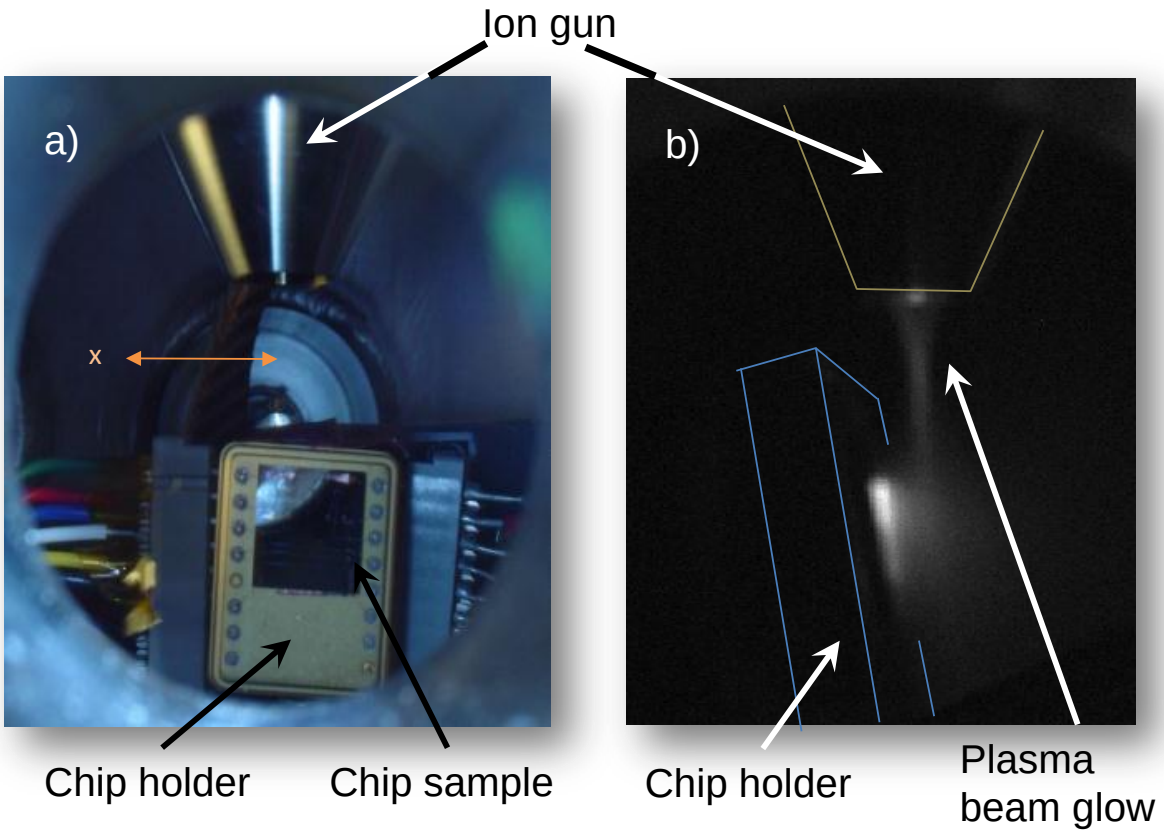

Figure 4.2 a) View through window on chamber wall. Sample under test is mounted vertically below ion gun nozzle, and can move in x,y,z. b) Ar ions ionize nitrogen gas in vacuum chamber producing a 'plasma' glow, which is captured with 2-photon sensitive Cascode camera. Beam current 3uA, at 1.577keV.

Measured data for the beam current output given adjusted emission current settings are shown in Figure B.2.1. Beam energy also affects the output current (Figure B.2.2): the higher the energy settings, the higher the current, because of the extraction voltage. In addition, the current can be controlled by adjusting the pressure (the amount of Ar gas) in the gun ionization chamber through the leak valve attached. Figure 2.3 shows the linear relationship between the leaked pressure into the gun and the output current.

The vacuum chamber itself sits atop an air-table for vibration isolation. The main vacuum pump is attached to the bottom of the chamber via a 6” flange. This arrangement

minimizes the pumping resistance and hence the orifice conductivity ($\propto d^3$) (see Sec. 2.3), and also minimizing the time taken to evacuate the chamber. During operation, the chamber pressure is kept at 1-5μTorr. A leak valve installed on the chamber allows a variation in chamber pressure. For the image taken in Figure 4.2b, the chamber was flooded with nitrogen gas to 0.1mTorr to induce the plasma glow which was imaged with 2-photon sensitive camera.

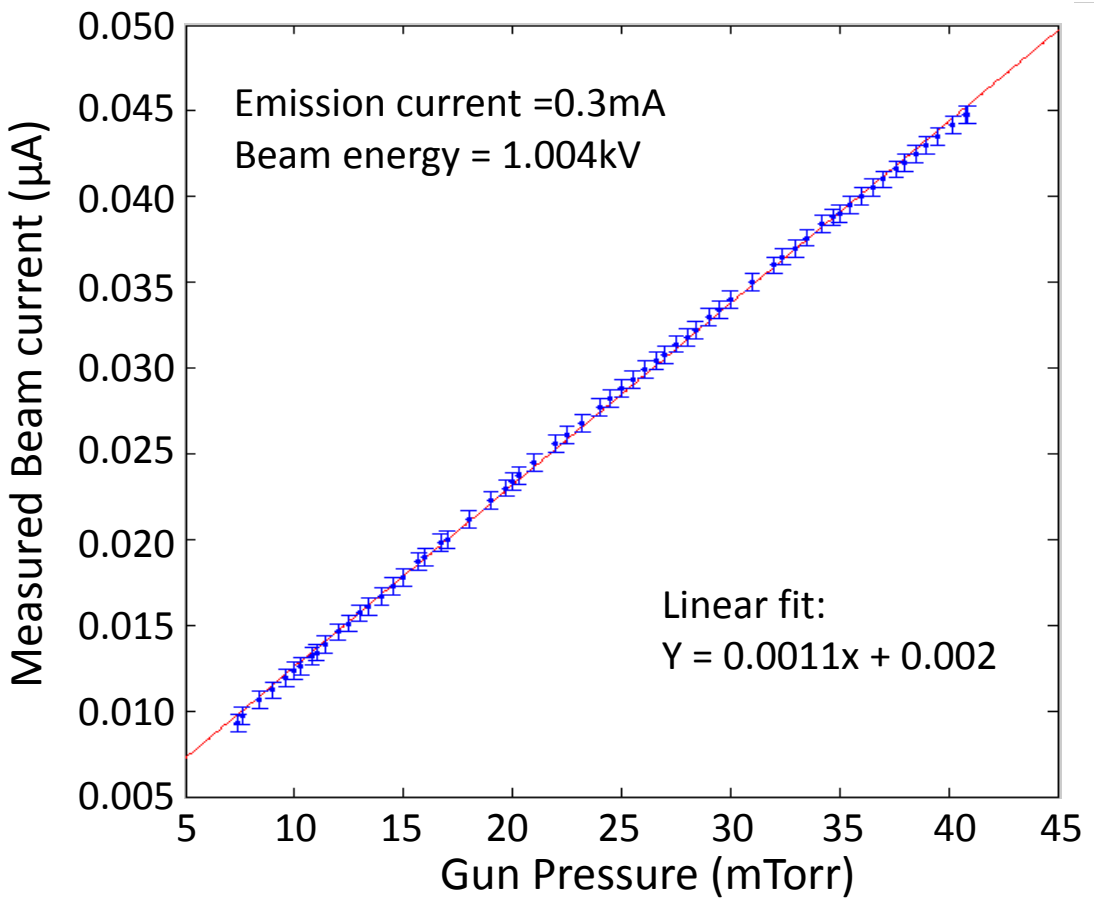

Figure 4.3 Output beam current as a function of the gas pressure within the gun's ionization chamber.

The micro-stage and sample-holding assembly allows the sample, which is held vertically (Figure 4.1, Figure 4.2a), to be moved in x, y, and z directions in order to align the beam into the

chip scale guiding structures. (See Appendix B.1, Figure B.1.2 and Figure B.1.3 for machining schematics). The micro-stages [63] can be controlled outside the chamber via Labview programs which were written to automate stage motion (e.g. in a raster-scan motion) and track stage position. See Appendix B.3 for Labview details. Hence the ion beam propagates parallel to the plane of the sample chip. Although there was no stage to adjust for the tilt, the ion gun steering optics could be used to compensate for beam tilt relative to the substrate plane.

Electrical signal access to the sample chip is achieved by wire bonding to pins on a chip holder. The pins of the holder are connected via soldered connectors to wires that lead out of the chamber through electrical feed-through flanges. The most frequently measured signal is the current from an electrode on the sample. This signal is read by the pico-amp sensitive Keithley 2400.

4.2 Vacuum System II

A great disadvantage of Vacuum System I was that the entire ion gun and vacuum top has to be lifted manually each time the inside of the chamber needed to be accessed e.g. during sample change. As devices became larger with higher electrical pin-counts, a greater demand for electrical feed-throughs and the need for a microscope-enhanced view of the sample, eventually drove the building of a new setup. As shown in Figure 4.4, the main improvements over the older setup are:

i) The size of the chamber is greatly increased to accommodate more components and to allow more electrical feed-throughs (the schematic details are shown in Figure 4.5).

ii) Microscope viewing of the sample from the top of the chamber to visually inspect the position of the probe tip on the sample surface.

iii) A needle probe, the tip of which can be lowered to/near the surface of the sample to measure the ion beam at that location. The current signal from this probe can then be used to electrically determine the beam current density at various positions for example along the channel structure on a device surface (Figure 4.6). The probe can also be used to profile the beam itself as shown in Figure 4.7. The needle probe aids in the alignment of the beam into the relevant channels by first locating the beam. Then the channel opening is brought to the probe point with probe and sample movements see through the optical microscope.

iv) One set of x-y-z stages with 50nm step resolution for sample movement, and another set to support probe movement so that the sample and probe can move independently to each other.

v) The vacuum gauge was changed from a magnetic-based "cold" gauge to a thermal gauge, because the magnetic field from the former was sufficient to cause several degrees of deflection of the charged particle beam (at 2keV).

vi) In addition to the ion gun source, an electron gun (Kimball Physics) was also installed.

The vacuum is again pumped from the bottom of the chamber to ensure maximum pumping speed.

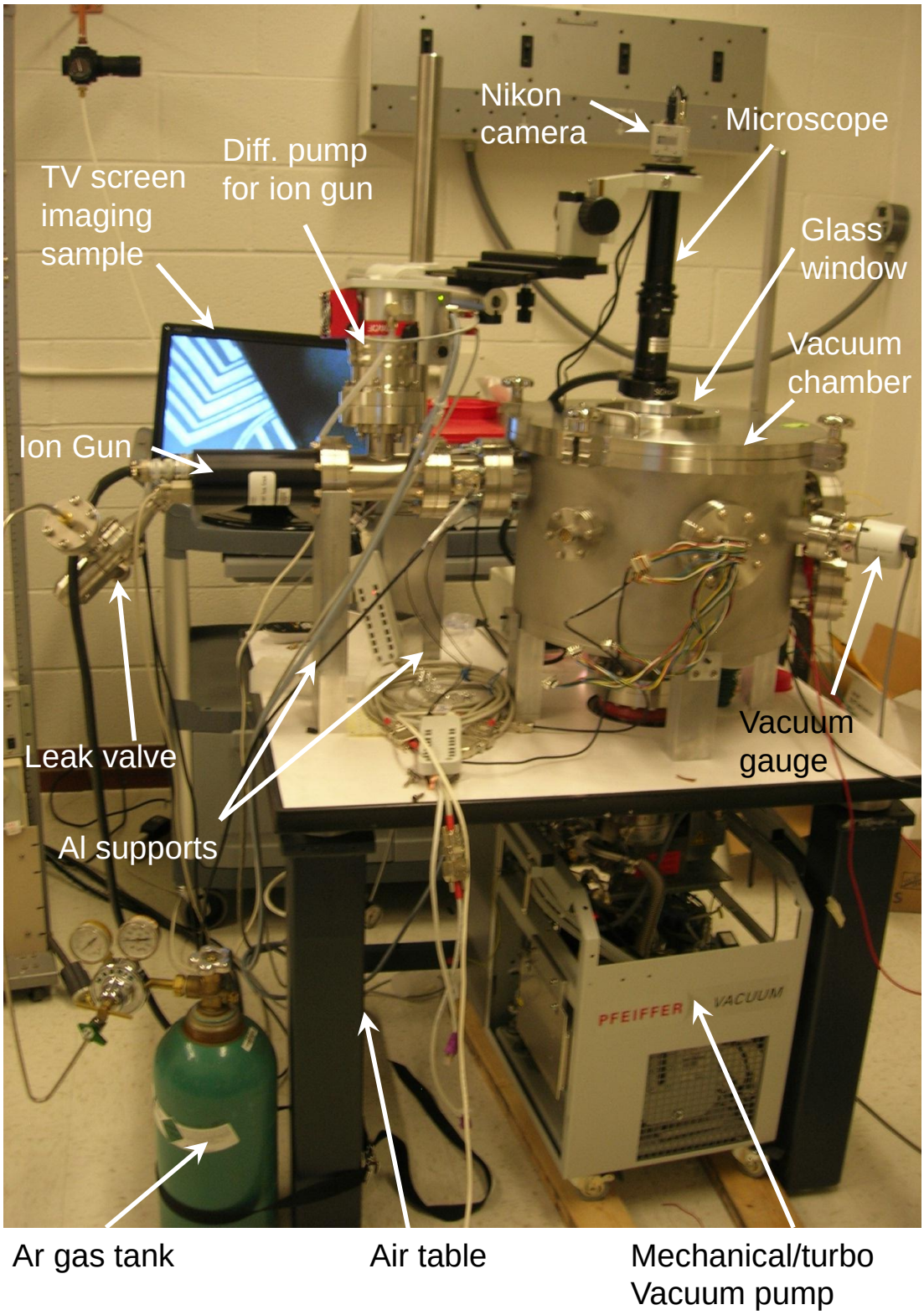

Figure 4.4 View of new setup with microscope viewing from chamber top, a chamber lid, two sets of microstages, and larger chamber space to provide more electrical feed-through flanges.

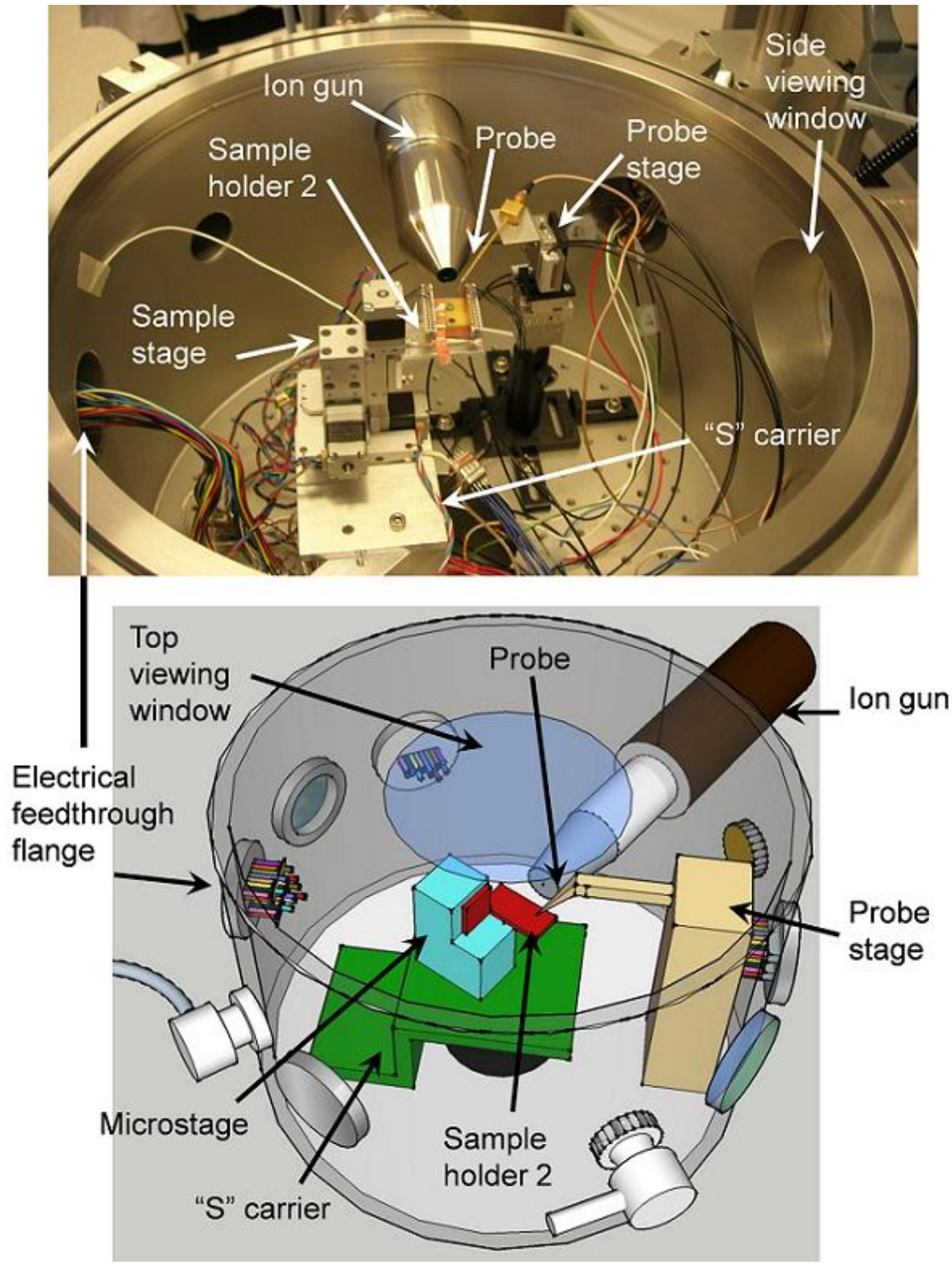

Figure 4.5 Chamber interior showing the components contained within: TOP is actual setup; BOTTOM shows the schematic. Main components include the sample stage and holder, probe stage and probe, top and side viewing ports.

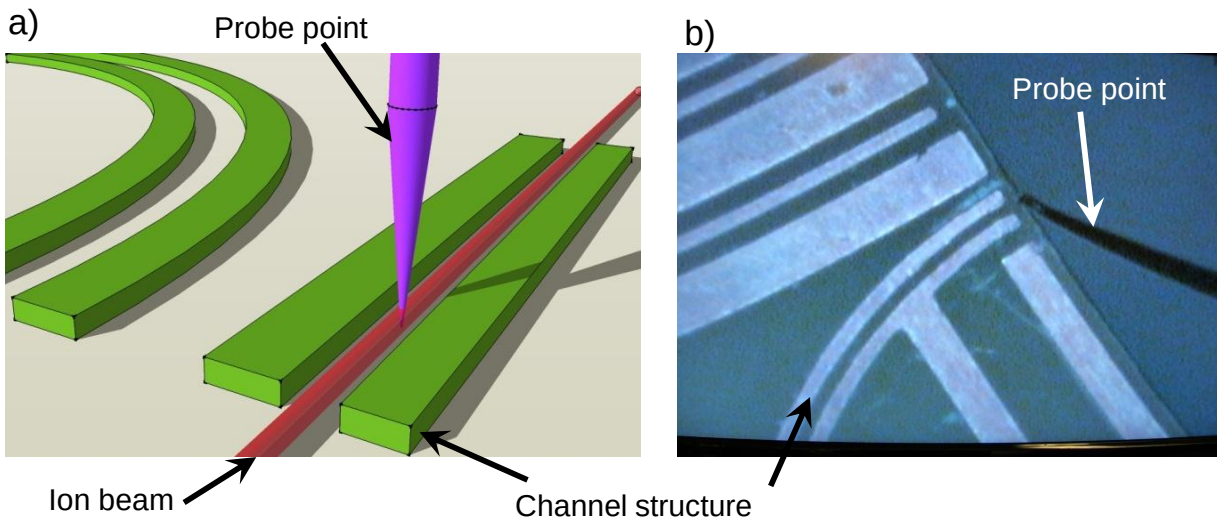

Figure 4.6 Needle probe sampling ion beam that is moving through a channel structure on a device shown in schematic in a) and shown as microscope snapshot in b) - the probe samples the beam current near the entrance of the channel structure for device alignment.

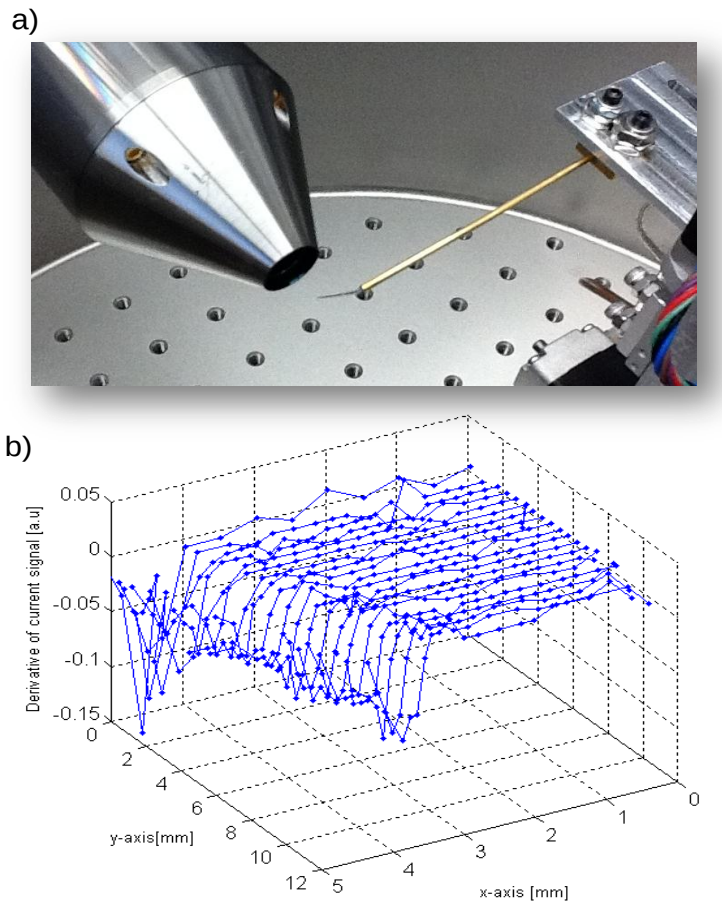

Figure 4.7 a) Image of probe sampling charged beam from ion source. The motorized stage was rastered in plane and resultant current signal is plotted in b).

4.3 Visual Alignment

In the case of Ar ions, the beam cannot be easily detected visually – even using a high sensitivity camera, the beam glow as shown in Figure **4.2**b) is only evident in higher pressures of 10^{-4} Torr. The glow itself is not a precise indicator of position, hence the position of the channel orifice is found by either scanning across the top edge of the device, or by the use of a probe needle – in both cases the beam is electrically detected.

However, with electron beams visual alignment is possible. Figure **4.8** shows a photo of the device under test in the vacuum chamber at 4μTorr. The spot where the electron beam impinges upon the FR4 dielectric material, a blue luminescent flow is visible to the naked eye. A weaker glow is produced when the electron beam targets silicon. This optical effect conveniently provides a visual marker for the alignment of the electron beam into the device channel.

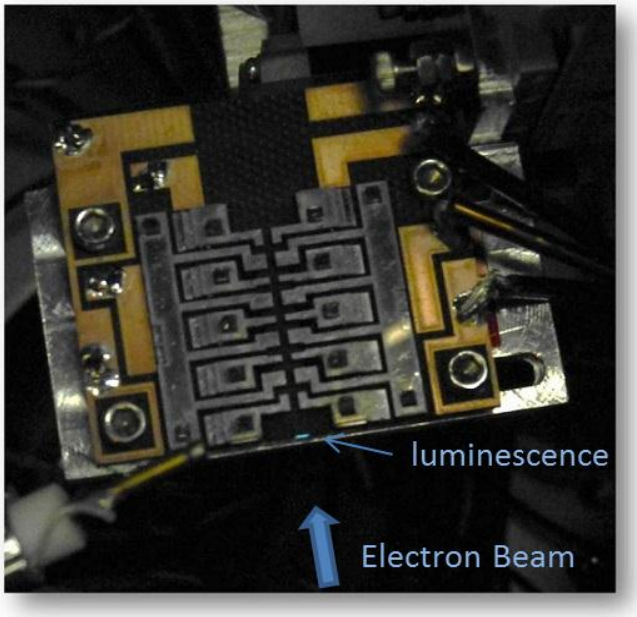

Figure 4.8 Electron beam on bombarding FR4 material of PCB during device testing results in a blue luminescent glow, visible by eye.

The luminescence may be a type of cathodoluminescence which occurs when impurities inside dielectrics creates energy levels in the band gap between the valence and conduction bands. When electrons relax from the conduction band to the valence band, they may go through those intermediate energy levels and the frequency of the photons emitted would be lower than that of a direct conduction-to-valence band transition. The emitted photons at these lower frequencies may lie in the visible spectrum. For materials such as silicon, the cathodoluminescence are shown to exhibit high spectrum counts for wavelengths which lie between 375nm to 480nm [64]. This would agree with the experimental observation that a bluish glow is seen from the electron beam impacting silicon.

4.4 Electric Breakdown

The setting up of a clean vacuum is essential of course not only for the generation of the charged particle beams but also to maximize the electrical breakdown voltage between electrodes in the micron-scale. In this way, the electric field density within the channel formed by the electrodes could be intensified, thus allowing stronger actuation effects on the charged particles. Of concern then, is the electric breakdown within the channels which determines the limit of field strength. The channel width may vary from tens to hundreds of microns.

Traditionally electric breakdown in gas has been attributed to the Townsend avalanche theory [65] [66] [67] which suggests that free electrons within the gas can be accelerated by the external strong electric field may have enough energy that when in collision with a neutral atom, may cause ionization of the neutral atom, thus ejecting other electrons. These in turn could cause further ionization and result in an avalanche effect, leading to a path of low electrical resistance

causing high currents to flow. The voltage required for breakdown increases with pressure because as the number of particles increases, the rate of electron collision and trajectory randomization increases. Within their mean free path (~0.5μm in air), the electrons will experience many collisions which reduce the chances of them having sufficient energy for ionization. Electrons that are not moving along field path will not be accelerated fully. Direction randomization then means that the field strength needed for the electron to reach the energy required for ionization must be higher than before, hence the increase of breakdown voltage with pressure. The Paschen curve, like Figure 4.9 (black line), are usually quoted for atmospheric conditions and indicate a minimum breakdown voltage of 327V for about 7.5um or 0.57cm-Torr (p·d product) at 1Atm [68]. Even at this high pressure, the E-field is 4.4×10^7V/m (44V/μm), which clearly illustrates the advantage of scaling the electrode structures down to the micron size. Ions and electrons of low energies will experience a greater actuation force with this E-field force than in magnetic fields.

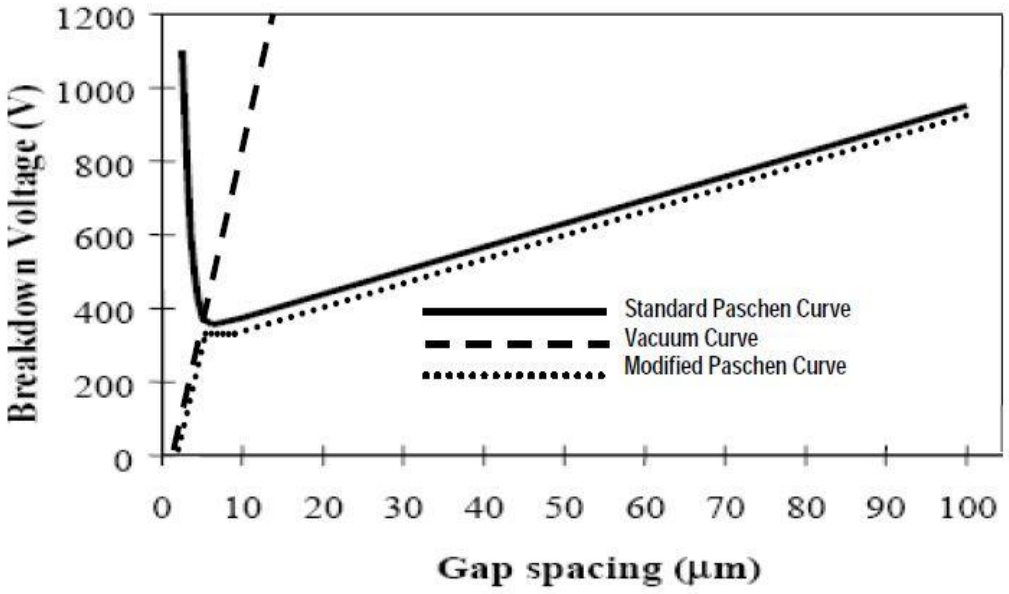

Figure 4.9 Paschen curve (solid line) and modified Paschen curve for spacing in atmospheric air. Plot taken from [69].

We are primarily operating at pressures of 10^{-5}-10^{-6}Torr at hundreds of microns, so the $p \cdot d$ product is around 10^{-7}cm-Torr which is much lower than the dipping point. Although the original Paschen curve seems to suggest a drastic increase in breakdown voltage below the dipping point, in reality this is not the case, as Townsend avalanching is not the only effect that will cause leakage currents. In a strong field, electrons can be pulled from the surface of the conductor [70], by field emission [71] and will be dependent on surface roughness since field density is increased at sharp edges. A large field emission current can also cause localized heating of the conductor and may result in some vaporization of the material, to be spread across the gap causing unwanted conduction [69]. Hence the modified Paschen curve (Figure 4.9 dotted line) is an attempt to adjust for field emission effects for low $p \cdot d$ products. In tests done in our setup, breakdown, accompanied with sparking occurred between silicon electrodes 1mm apart at 2.37kV in air. Sparking was not seen for the >100 μm gaps that were used in vacuum (10^{-5}-10^{-6}Torr) up to 2.2kV. Other experimental results [72] indicate a breakdown voltage of about 2.5kV for a gap of 20μm (125V/ μm) at 30mTorr (Figure 4.10). [73] reports breakdown voltages of 8000V between a 500μm gap at 10^{-3}Pa (7.5 μTorr), and of 1700V at 0.1Pa (0.75milli-Torr). We anticipate similar breakdown voltages at these pressures.

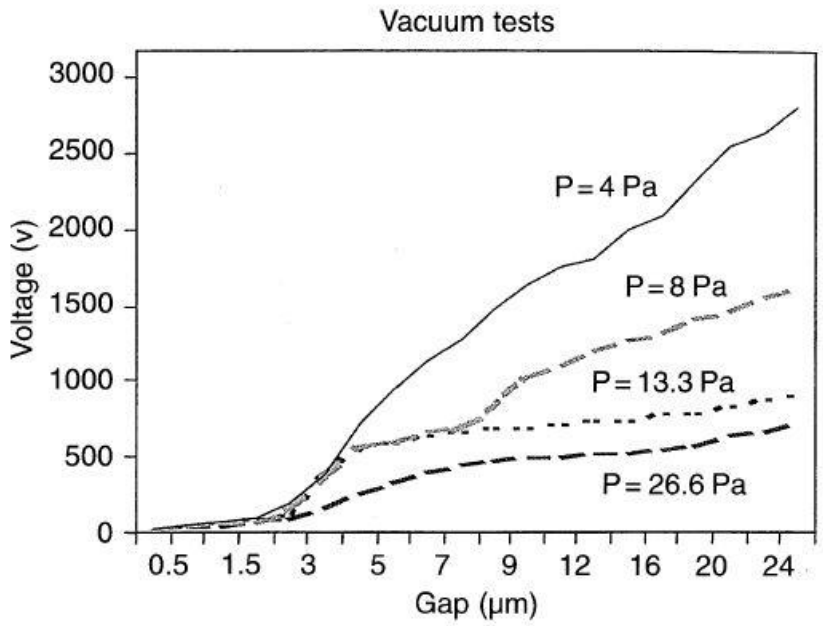

Figure 4.10 Experimental data from [72] for breakdown voltage of small gaps at semi-vacuum conditions.

4.5 Vacuum Considerations

The ion gun normally operates at 10^{-3} – 10^{-4}Torr, and the electron gun (and most electron-microscopy) operates at 10^{-4} – 10^{-6} Torr. These are considered medium to high vacuum conditions. To give some perspective, Northern Lights (at altitudes of 50km to 200km above sea-level) occur at these pressures in the upper atmosphere [74]. It is desirable to minimize the time needed to pump out the vacuum chamber. Here some basic gas flow theory is introduced to elucidate the chamber design choices that were made.

Let us consider the particle beam of current *I* traversing through a gas of density *n* per unit volume. This beam will undergo collisions with the gas particles and the current attenuated

by the collisions goes as $\boldsymbol{dI = -I\sigma n dx}$, where *dx* is the thickness of the gas the beam penetrates, and σ is the so-called cross-section which can be understood to be the area inside which the reaction of interest (e.g. collisions) would take place. The target thickness *dx* that is penetrated is $\boldsymbol{dx = v \cdot dt}$ for a beam velocity *v*. The solution to the beam current is an exponential decay:

$$\boldsymbol{I = I_0 e^{-x/\lambda} = I_0 e^{-t/\tau}} \qquad (\mathbf{4}.21)$$

where λ is the mean free path and τ is the mean particle life-time (before collision). τ is highly dependent on σ: $\boldsymbol{\tau = \frac{1}{v\sigma n}}$. The cross-section is representative of the various processes by which the beam could be lost, namely the elastic and inelastic interactions between the beam particles and the residual gas particles. Very little energy is lost by the projectile particle in the former case, while in the latter case the energy loss may be substantial. Elastic processes include single and multiple Coulomb scattering (involving Rutherford scattering cross-section), while inelastic processes include Bremstrahlung, ionization energy loss, electron capture and loss processes, and nuclear processes. The total cross-section should reflect these processes by summing up the individual cross-sections: $\boldsymbol{\sigma_{TOT} = \sigma_{Brem} + \sigma_{ionization} + \sigma_{Coulomb} + \cdots}$ The references for theoretical derivations of the cross-sections are [75] [76]. As an example, for electrons the mean free path is 50mm at 1mTorr, and 50m at 1μTorr [77].

Of interest in terms of pumping speed is the gas flow, which can be generally grouped into 2 types:

a) *Viscous flow* at high pressures when the gas behaves like a homogeneous fluid and the mean free path is smaller than the chamber dimensions. Intermolecular interactions are

higher than particle-wall interactions. This type of laminar flow can be impeded by turbulence and drag forces at the walls.

b) *Molecular flow* at low pressures in which the mean free path is larger than container dimensions and the particles behave like billiard balls. The intermolecular interactions are less than the particle-wall ones.

The transition between these two regimes is approximates at 1mTorr [74].

The pumping speed at any given point is $S = \frac{dV}{dt}$, that is volume/time. The throughput at any given point is defined to be: $Q = P \cdot S$, which is equivalent to the number of particles passing through per time, at a given temperature. For a conductor that transmits the gas e.g. a vacuum tube, the throughput passing through it is: $Q = C(P_1 - P_2)$, where *C* is the conductance analogous to Ohm's law in electric circuitry, and the gas is flowing from regions of pressure P_1 to P_2. Just as for electric conductors, if the gaseous conductors are connected in series, the conductances add up as: $\frac{1}{C} = \frac{1}{C_1} + \frac{1}{C_2} + \cdots$ The units for *S* and *C* are the same [m^3/s].

Hence for a system with pump at speed S_p, through a tube with *C*, the overall net evacuation speed S_{net} is [77]:

$$\frac{\mathbf{1}}{\boldsymbol{S_{net}}} = \frac{\mathbf{1}}{\boldsymbol{S_p}} + \frac{\mathbf{1}}{\boldsymbol{C}} \qquad (\mathbf{4}.22)$$

In viscous flow regime, the conductance of a circular tube with diameter D and length L is:

$$C_{vis} = \frac{\pi D^4}{128 \cdot \eta \cdot L} \cdot \bar{P}$$

where η is the gas viscosity and $\bar{P}$ is the average pressure.

In molecular flow regime, the conductance is:

$$\boldsymbol{C_{mol} = \frac{v \cdot \pi \cdot D^3}{12 \cdot L}} \qquad (\mathbf{4}.23)$$

The pump down time is inversely proportional to pump speed: $t = \frac{V}{S_{net}} ln\left(\frac{P_1}{P_2}\right)$, for a volume *V*. To minimize pump-down time, or to maximize S_{net} , the conductance of the connecting tubes must be maximized as seen from Eqn.2.1, as the pumping speed in practice remains constant. Since most of the time will be spent pumping in the molecular flow regime, Eqn. 2.2 indicates that the tube diameter needs to be maximized and the length minimized. For this work, the vacuum tube is reduced to the length of the rubber connector that connects the chamber to the pump which hangs off of it. The diameter of the pumping opening is about 6" which is the orifice size of the pump itself.

For higher pumping efficiency, we had a two-stage pumping system: at high pressures >1mTorr, a rotary vane pump is used as a roughing pump, then a turbo-pump kicks in for lower pressures down to micro-Torr. Venting is done through the pumping system automatically [74].

4.6 Outgassing

A brief mention must be made for the outgassing of materials in vacuum as it determines the level of vacuum achievable, especially below 10^{-5}Torr. Outgassing is the release of gases

desorbed from surfaces as pressure decreases. Surfaces absorb particles from air, especially CO_2 and water, which is released into the chamber at low pressures. In addition there is vaporization of surface materials, diffusion and permeation of gases through the chamber walls as well as internal and external leaks from flanges and trapped air pockets e.g. inside screw holes [1]. Rough and porous surfaces absorb more than smooth polished ones. In the table below are outgassing rates taken from [1] to compare some commonly used materials.

Table 2 Comparison of outgassing rates of common chamber materials from [a] **[1]** and [b] **[2]**.

Material	**Outgassing rate (10^{-7} W/m^2)**
Aluminum [a]	84.0
Stainless steel (mech. polished) [a]	22.8
Copper (mech. polished) [a]	46.7
Copper (fresh) [a]	533.0
Pyrex (1 month in air) [a]	15.5
Plexiglas [a]	961x10^6
Teflon [a]	8.7 x10^6
FR4 [b] (bake-out 150^{0}C)	6.1
Alumina [b] (bake-out 150^{0}C)	3.1
Epoxy-acrylic [b] (bake-out 150^{0}C)	28
Epoxy-glass fiber [b] (bake-out 150^{0}C)	20

It is noted then, that while Al, mechanically polished stainless steel and some ceramics such as alumina, are adequate vacuum material, polymers (plastics and rubbers) should not be used inside the chamber. If the chamber and the components inside can be baked out in vacuum for >30min at say, 150^{0}C, the residual gases trapped inside bulk pores can be removed, resulting in a higher vacuum when the chamber returns to room temperature.

On a practical note, components are cleansed with acetone and IPA to reduce the amount of organics e.g. finger-print oils, machine-lubricants and soldering flux that may have accumulated during handling. The chamber should be kept at vacuum whenever not in use, to minimize the water vapor in air to build up inside the chamber volume.

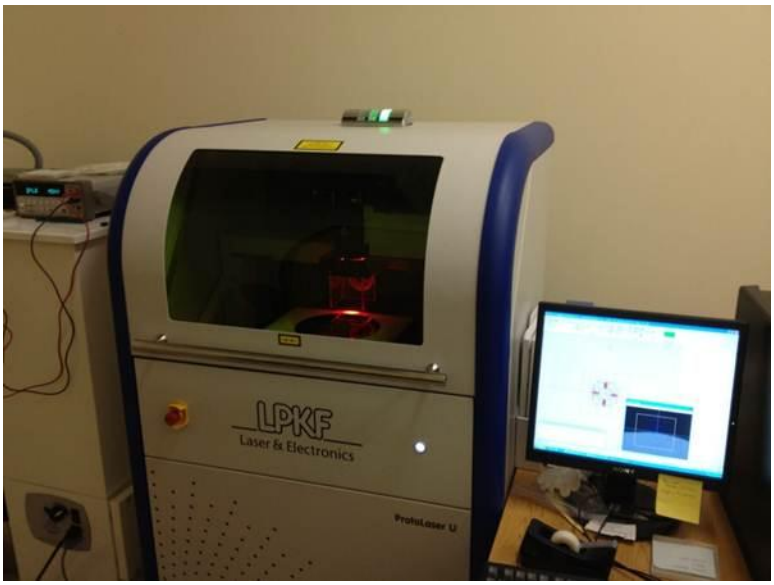

Figure 4.11 Photo of UV laser for micromachining of Si and PCB. Photo taken by Serhan Ardanuç

4.7 UV Laser

An UV laser [78] (LPKF ProtoLaser U) with 355nm wavelength, was used to micro-machine the silicon (through wafer etch) with a beam width of 25µm. (See Figure 4.11). The sample to be cut sits atop a high precision stage of 9”x12”. The etch rate is 19.7µm per cut repeat on silicon as shown in Figure 4.12. Laser micro-machining was used for the process described in Section 3.4.

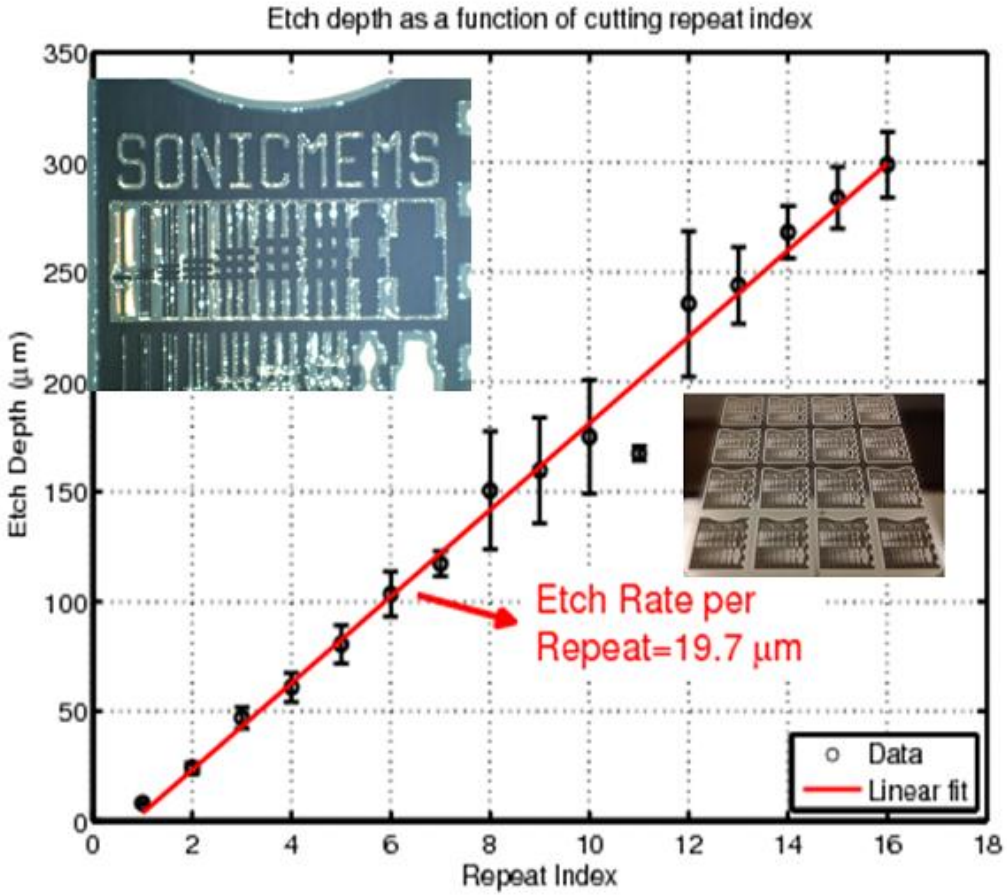

Figure 4.12 Etch depth data as a function of the number of laser cut repeats. Insets show the some patterns written for etch depth measurement. Data taken by Serhan Ardanuç.

Appendix A

A.1

Longitudinal Transport Limits for Laminar Beam: Derivation

For completeness, the electric and magnetic fields generated by a laminar beam in the simple cylindrical model will be shown here. All derivations are also given in (Reiser, 1994).

Let assume a beam to be of a cylindrical geometry with radius *a*, and propagating through an infinite tube of radius *b*. Let the variation in beam radius be small along *z*, the direction of propagation so that electric and magnetic z-components can be neglected. The beam density is assumed to be uniform. The beam is in a steady state situation.

Applying Gauss's law $\int E \cdot dS = \int \frac{\rho}{\varepsilon} dV$, the radial electric field is:

$$\boldsymbol{E_r = \frac{\rho_0 r}{2\varepsilon_0} = \frac{Ir}{2\pi\varepsilon_0 a^2 v}} \qquad \text{for } \boldsymbol{r \le a} \qquad (A.1.24)$$

$$\boldsymbol{E_r = \frac{I}{2\pi\varepsilon_0 r v}} \qquad \text{for } \boldsymbol{r > a} \qquad (A.1.25)$$

From the Ampere's Law $\int B \cdot dl = \mu_0 \int J \cdot dS$, the magnetic field in the θ direction is:

$$\boldsymbol{B_\theta = \mu_0 \frac{Ir}{2\pi a^2}} \qquad \text{for } \boldsymbol{r \le a} \qquad (A.1.26)$$

$$\boldsymbol{B_\theta = \mu_0 \frac{I}{2\pi r}} \qquad \text{for } \boldsymbol{r > a} \qquad (A.1.27)$$

By integrating Eqn. A.1.24 and A.1.25, the potential distribution, assuming $V = 0$ at $r = b$, is:

$$V(r) = V_s\left(1 + 2\ln\left(\frac{b}{a}\right) - \frac{r^2}{a^2}\right) \qquad \text{for } r \le a \qquad (A.1.5)$$

$$V(r) = 2V_s \ln\frac{b}{r} \qquad \text{for } a \le r \le b \qquad (A.1.6)$$

where

$$V_s = \frac{\rho a^2}{4\varepsilon_0} = \frac{I}{4\pi\varepsilon_0\beta c} \tag{A.1.7}$$

Hence the peak potential occurs at *r=0*:

$$V(0) = V_0 = V_s\left(1 + 2\ln\frac{b}{a}\right) \tag{A.1.8}$$

Particles entering the drift tube have kinetic energy $(\gamma - 1)mc^2$. For particles on the axis, in order to compensate for the gain in potential energy, the kinetic energy is reduced by qV_0 so that: $\gamma(0)mc^2=\gamma mc^2$-$qV_0$. The particle is stopped when all its kinetic energy is converted to potential energy, and the current limit is reached:

$$(\gamma - 1)mc^2=qV_0 \tag{A. 1.9}$$

Eqns. A.1.8 and A.1.9 gives the current limit as:

$$I_L = I_0\frac{\left(\gamma^{2/3} - 1\right)^{3/2}}{1 + 2ln(b/a)} \tag{A.1.10}$$

where

$$I_0 = \frac{4\pi\varepsilon_0 mc^3}{q} \tag{A.1.11}$$

A.2

Child Limit Derivation

Consider a gap between two plane electrodes (a diode) of gap distance *d* and potential difference V_0. The question is how much current can flow within the gap from one electrode to the other as shown in Figure A.1.

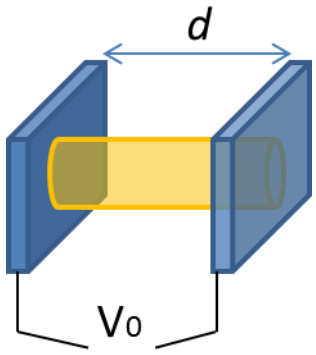

Figure 44.13 Illustration of the geometry of concern in the Child current limit.

Let x denote the direction of beam propagation with one electrode situated at *x=0* and the other at *x=d*. The potential is $\phi = 0$ at *x=0*, and $\phi = V_0$ at *x=d* (See Figure 1.8a). The steady state solution for the potential can be found by considering the Poisson's equation, the continuity equation and the equation of motion for a particle with charge Zq where Z is the ionization state:

$$\nabla^2\phi = \frac{d^2\phi}{dx^2} = -\frac{\rho}{\varepsilon_0} \qquad \text{(Poisson's equation)} \qquad \text{(A.2.1)}$$

$$J_x = \rho\dot{x} = \text{const} \qquad \text{(continuity)} \qquad \text{(A.2.2)}$$

$$\frac{m}{2}\dot{x}^2 = Zq\phi(x) \qquad \text{(equation of motion)} \qquad \text{(A.2.3)}$$

Substituting for $\dot{x}$ from Eqn. A.2.3 into A.2.2, and then for ρ from Eqn. A.2.2 into A.2.1 the latter becomes

$$\frac{d^2\phi}{dx^2} = \frac{J}{\varepsilon_0\sqrt{\frac{2Zq}{m}\phi}} \tag{A.2.4}$$

Multiply both sides by $d\phi/dx$, and the left side becomes an exact differential of $\frac{1}{2}\left(\frac{d\phi}{dx}\right)^2$ so that after integration we have

$$\left(\frac{d\phi}{dx}\right)^2 = \frac{4J}{\varepsilon_0\sqrt{\frac{2Zq}{m}}}\phi^{1/2} + C \tag{A.2.5}$$

Now considering the boundary condition $\phi = 0$ at *x=0*, and let $\frac{d\phi}{dx}(x = 0) = 0$, then *C=0*. Integrating again we find,

$$\frac{4}{3}\phi^{3/4} = 2\left(\frac{J}{\varepsilon_0}\right)^{1/2}\left(\frac{2Zq}{m}\right)^{-1/4} x$$

and noting that $\phi = V_0$ at *x=d*, we have

$$\phi(x) = V_0\left(\frac{x}{d}\right)^{4/3} \tag{A.2.6}$$

and

$$J = \frac{4\varepsilon_0}{9}\sqrt{\frac{2Zq}{m}}\frac{V_0^{\frac{3}{2}}}{d^2} \tag{A.2.7}$$

We note here from Eqn. A.2.6 and Figure 1.8a) that for electrons the negative charge lowers the potential along *x* in the gap. The current limit in Eqn. A.2.7 can be increased either by increasing the voltage across the gap or by decreasing the gap size. The Child limit result is important for ion and electron sources. The current density limit for electrons is about 43 times that for protons. The current limits in [A/m^2] for electrons and protons respectively are:

$$J_{electrons} = 2.33 \times 10^{-6} \cdot \frac{V_0^{\frac{3}{2}}}{d^2} \tag{A.2.8}$$

$$J_{protons} = 5.44 \times 10^{-8} \cdot \sqrt{\frac{Z}{A}} \frac{V_0^{\frac{3}{2}}}{d^2} \tag{A.2.9}$$

Where Z is the ionization state of the ion and A is the atomic number.

If the potential of the first electrode plate is not zero, as shown in Figure 1.8b) then the boundary condition will be: $\phi(x = 0) = \phi_1$ and $\phi(x = d) = \phi_2 = \phi_1 + V_0$. The potential inside the gap becomes bow-shaped and particles can still traverse the gap even if the electric field at the entrance is opposite to its direction of motion since the particles will enter the gap with some kinetic energy. In order to cross the potential "hump", the particle must sacrifice its kinetic energy. The limit for current occurs when the peak potential of the bow-shape reaches zero as shown in Figure 1.8b) where we will call the corresponding position in *x* is d_p. At this point an increase in current will raise the potential such that any particle entering the gap will be reflected. Hence $\phi(x = d_p) = 0$, and $\frac{d\phi(x=d_p)}{dx} = 0$. The Poisson equation can be integrated on both sides of d_p, leading to the expression:

$$\frac{4}{3}\left[(-\phi_1)^{3/4} + (-\phi_2)^{3/4}\right] = \sqrt{\frac{4J}{\varepsilon_0\sqrt{\frac{2Zq}{m}}}}\, d \tag{A.2.10}$$

From the above the current limit can be found to be:

$$J = \frac{4\varepsilon_0}{9}\sqrt{\frac{2Zq}{m}}\frac{V_0^{\frac{3}{2}}}{d^2} G(\rho) \tag{A.2.11}$$

This differs from Eqn.A.2.7 by a correction factor:

$$G(\rho) = \chi^{3/2}\left[\left(1 - \frac{1}{\chi}\right)^{3/4} + 1\right]^2 \tag{A.2.12}$$

for which,

$$\chi = \frac{\phi_2}{\phi_2 - \phi_1}$$

Figure A.2 shows the enhancement factor $G(\rho)$ to the standard Child limit, and reduces to Eqn.A.2.7 when the electrode at the entrance is zero ($\chi = 1$). The figure indicates that the current limit increases rapidly (space-charge drops) as particles are accelerated. As an example, in an post-acceleration gap that doubles the energy of the particle ($\chi = 1$) is 7.2 times the current limit for the standard Child limit.

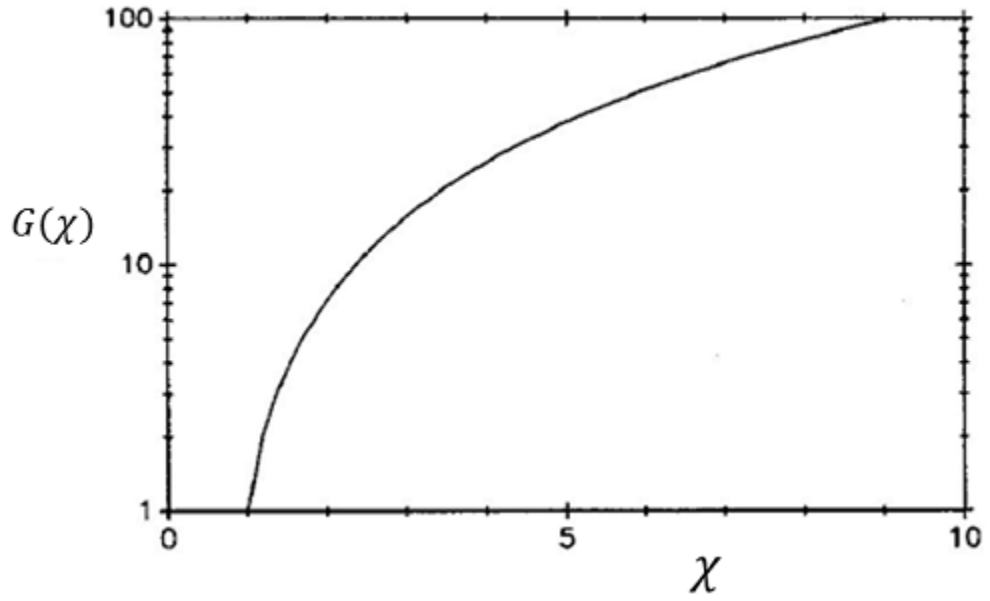

Figure A.14 Correction factor for the Child limit for Eqn. A.2.11. Plot taken from **[79]**.

A.3
Limit of Current Emitted from Source

Thermionic emission, that is "boiling off" of electrons from heated cathodes e.g. filaments, is the most commonly method used. For emission to occur, electrons must gain at least a kinetic energy of $\epsilon_F + \Phi_W$, where ϵ_F is the Fermi level of the metal and Φ_W is the work function. In metals typically Φ_W is 2-5eV [25]. The emission current density is related then to the temperature of the cathode by the Richardson-Dushman equation [25], [10]:

$$J_{thermionic} = AT^2 e^{-q\Phi_W/k_B T} \tag{A.3.1}$$

where

$$A = \frac{4\pi q m k_B^2}{h^3} = 1.2 \times 10^6 \ A\, m^{-2} K^{-2}$$

For example, tungsten with $\Phi_W = 4.5eV$, operating at 2500K ($k_B T \sim 0.2eV$) will be limited to a current density of $0.5\ \mathrm{A}/cm^2$ [10]. Dispenser cathodes of barium or strontium oxides buried in porous tungsten, can achieve higher current densities of $10 - 20\ \mathrm{A}/cm^2$. For these, $\Phi_W = 1.6eV$, and operating temperature is 1400K ($k_B T \sim 0.12eV$).

Field emission, on the other hand is more complicated to calculate: the shape of the cathode greatly changes the electric field responsible for the emission. Here, it would suffice to point out that the effect is caused by quantum mechanical tunneling of the conduction band electrons through the metal surface barrier:

$$V_{barrier} = -\frac{q^2}{4z} - qE_{field}z \tag{A.3.2}$$

where E_{field} is the electric field in z direction. [25] and [80] shows that if $U_z = \frac{p_z^2}{2m} + V_{barrier}$ is the electron energy in z-direction incident on the barrier, then the current density is:

$$J_{Field} = \int_{-\infty}^{\infty} qn(U_z)P(U_z)dU_z \qquad (A.3.3)$$

where $n(U_z)$ is the electron flux into the barrier, and $P(U_z)$ is the probability of penetration. $n(U_z)$ is assumed to follow Fermi-Dirac statistics for a gas of free electrons. $P(U_z)$ can be derived from WKB approximation assuming a 1D potential and is where the complication of the integral in Eqn.A.3.3 comes from. The result is the Fowler-Nordheim formula [81] which will be stated here for completeness:

$$J_{Field} = 1.54 \times 10^{-6} \frac{E_{field}^2}{t^2(y)\Phi_w} \cdot exp\left(-6.83 \times 10^7 \times \frac{\Phi_w^{\frac{2}{3}}}{E_{field}} \vartheta(y)\right) \qquad (A.3.4)$$

where:

$$y = \frac{\sqrt{q^3 E_{field}}}{\Phi_w}, \qquad t(y) = \vartheta(y) - \frac{2}{3} y \frac{d\vartheta}{dy}$$

$$\vartheta(y) = \sqrt{\frac{1+\sqrt{1-y^2}}{2}} \cdot \left\{E(k) - \left[1 - \sqrt{1-y^2}\right] K(k)\right\}$$

such that $E(k)$ and $K(k)$ are complete elliptic integrals of the first and second kinds, and

$$k^2 = \frac{2(1-y^2)^{\frac{1}{2}}}{1+(1-y^2)^{\frac{1}{2}}}$$

$\vartheta(y)$ and y are tabulated in [82]. The Fowler-Nordheim equation (Eqn.A.3.4) has been shown to agree with experiment [83], [84].

Experimental data [85] [86] has shown shows that field emission tips can be made to be <

100 nm with a field $>10^7$ V/cm^2, resulting in emission currents on the order of 10^7 A/cm^2. [81] further references some experiments with tungsten nano-tips emitting at 10^9-10^{10} A/cm^2. A major disadvantage of field emission is that it demands very high vacuum, usually $<10^{-10}$ Torr, which could require very long pump-down times. The emission current is highly sensitive to contamination on the emission tips. Even for high densities such as 10^{10} A/cm^2, the actual emitted beam current is low because the tip size in this case is about 10 nm which translates to 0.01A in the best case.

Once field emitted electrons (stripped from "cold cathodes") and/or plasmas are formed, their extraction current limit is as described in Section 1.4.2 in the Child law with $G(\rho)=1$.

Appendix B

B.1

Setup Details and Machine Drawings

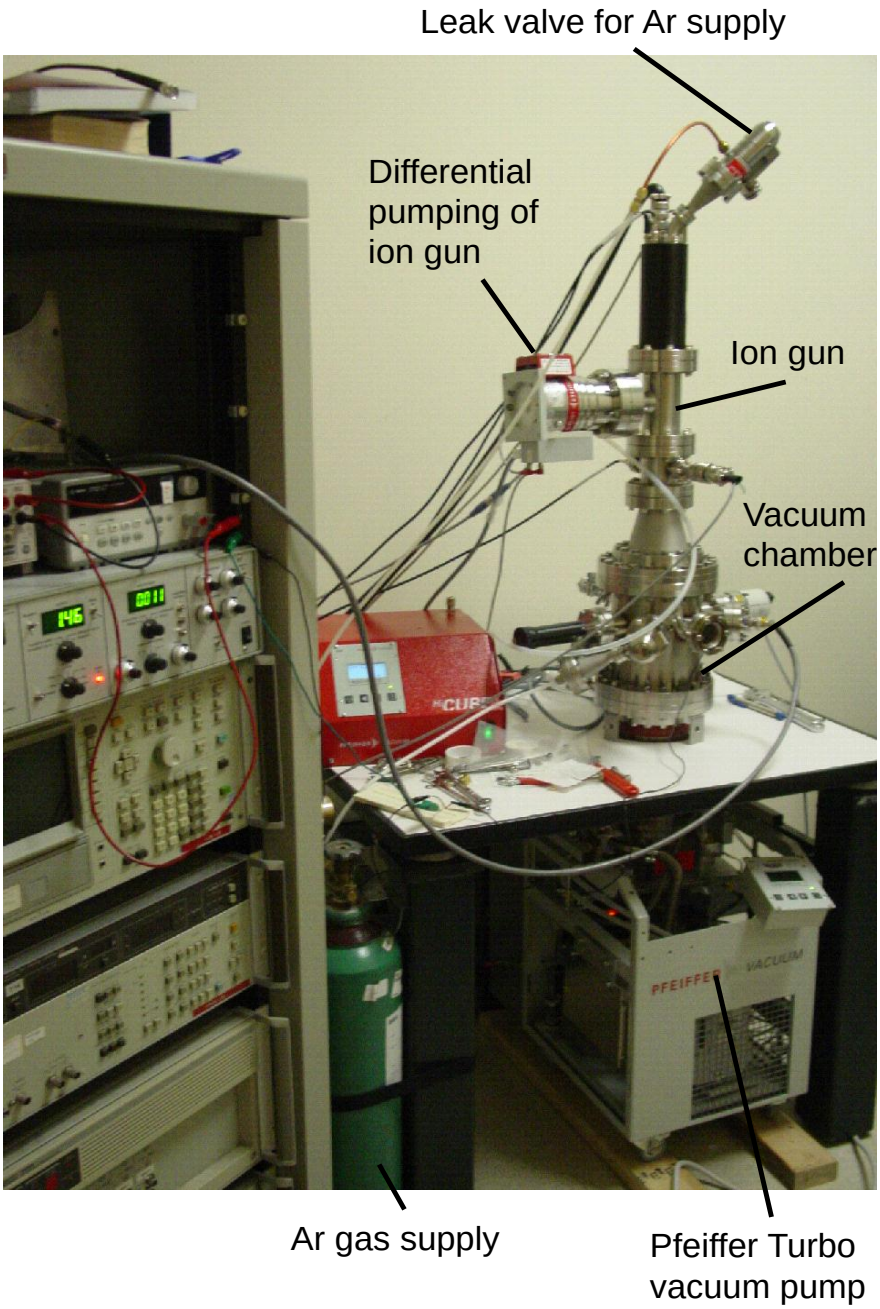

Figure B.1.1 View of entire preliminary setup. Vacuum chamber is pumped from below by pump hanging through a hole in the air table. Ion gun ejects beam vertically down into chamber from top, and is differentially pumped.

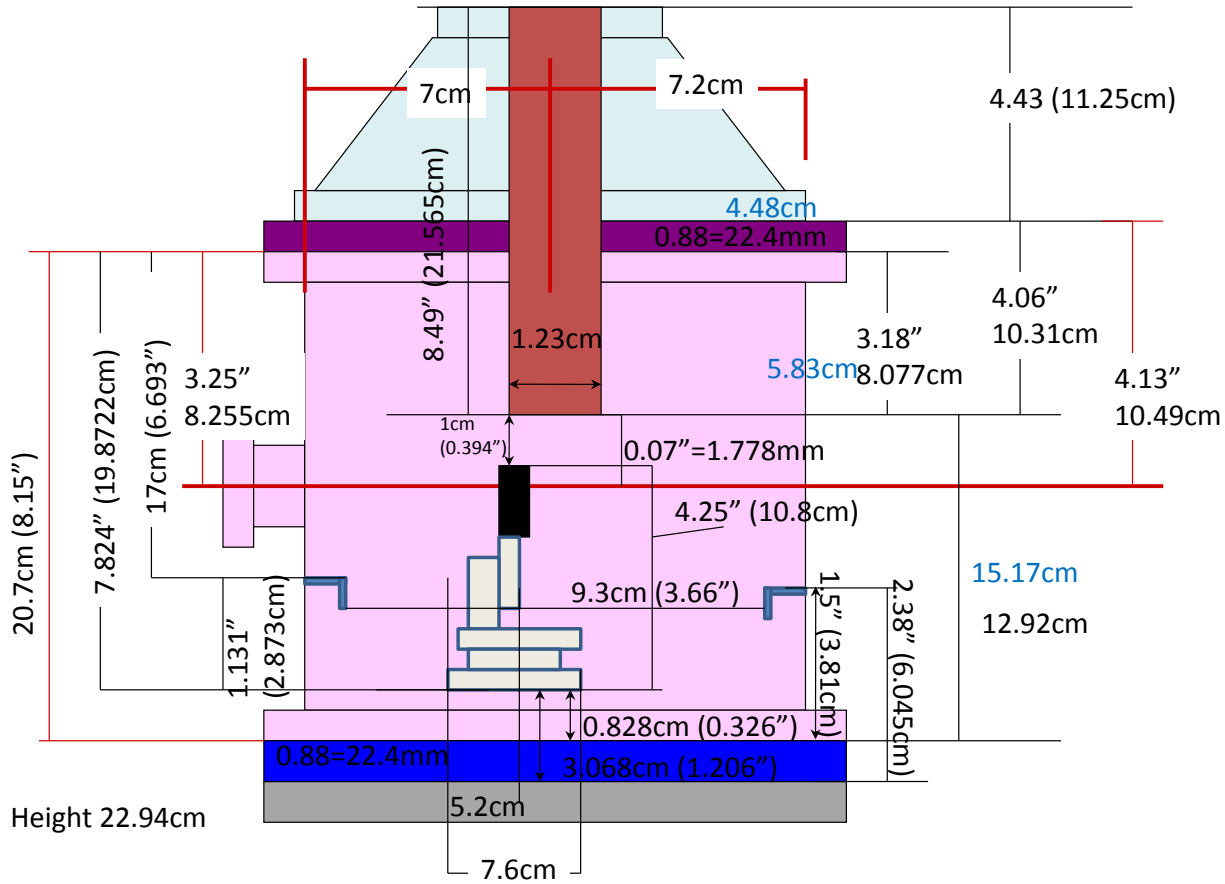

Figure B.1.2 Schematic of chamber and stage placements within with dimensions.

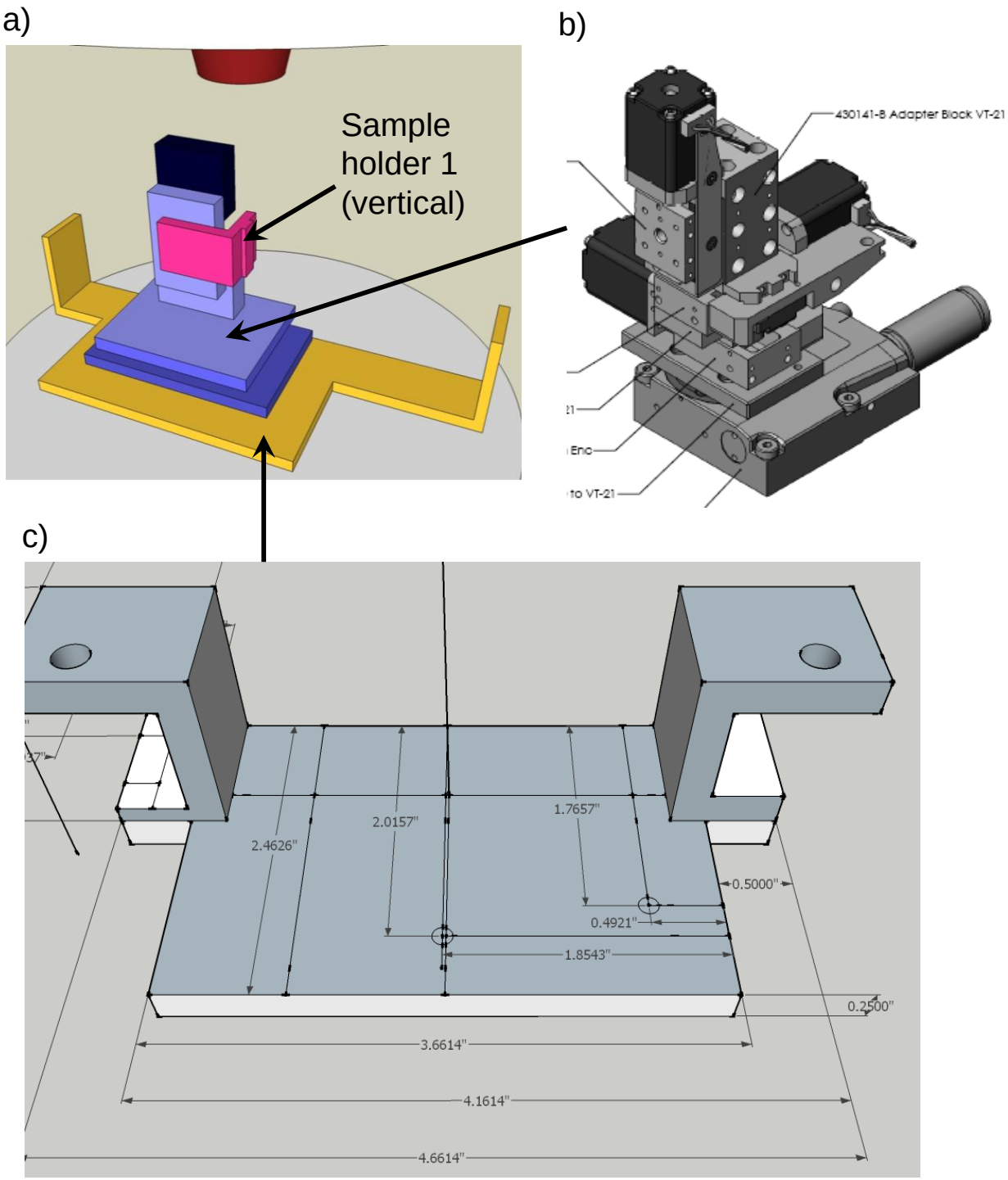

Figure B.1.3 a) Schematic of sample holder, stage, and carrier boat assembly inside vacuum chamber. b) CAD drawing of X-Y-Z stage (VT-21 10mm RS-40) from MicosUSA **[63]**. c) Machine drawing of carrier boat to secure the stage in chamber.

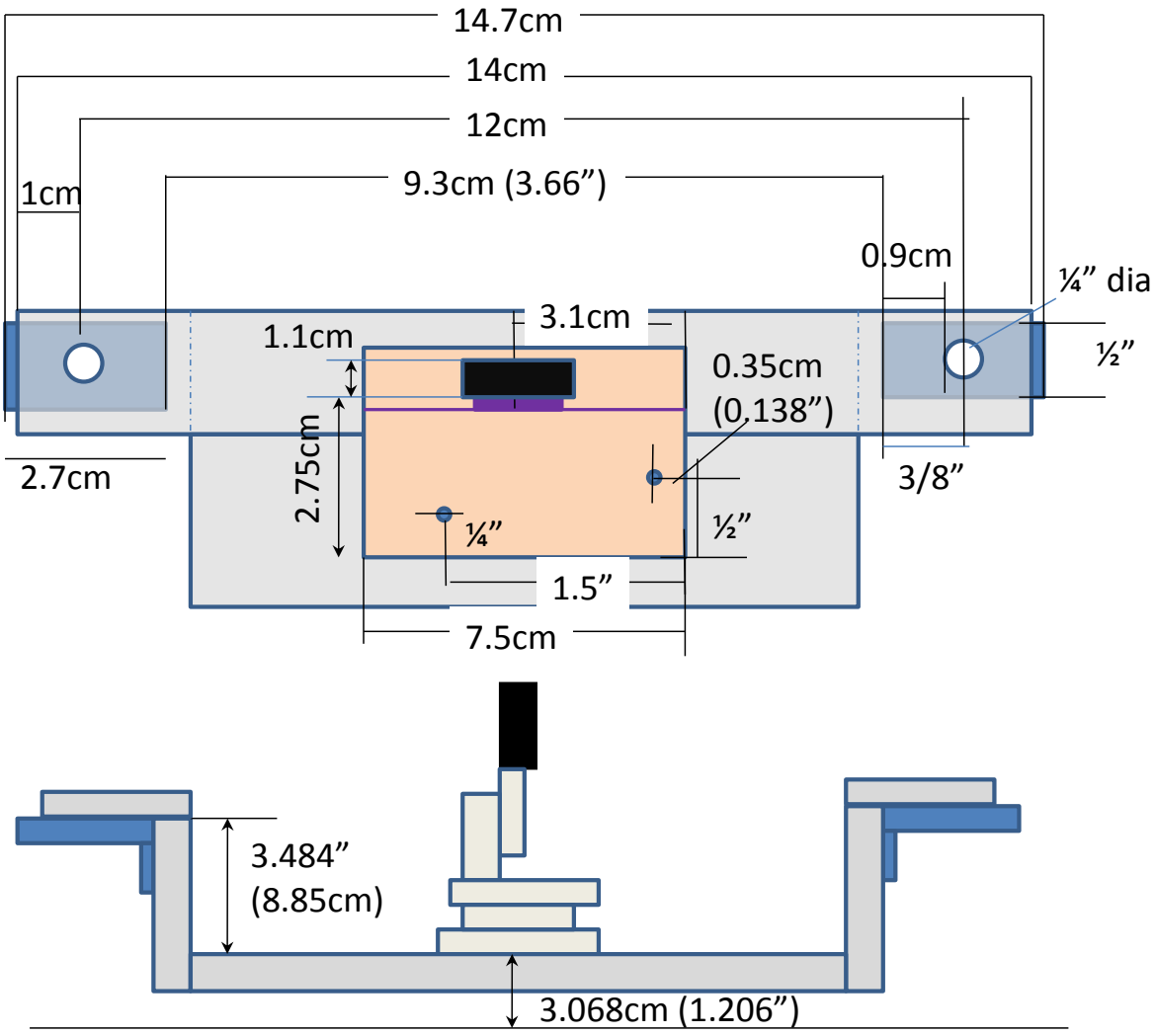

Figure B.1.4 Schematic drawing of carrier boat and stage placement with dimensions. Top: top view; Bottom: side view.

Figure B.1.5 Machine drawings of vertical "sample holder 1" in Figure 4.1.

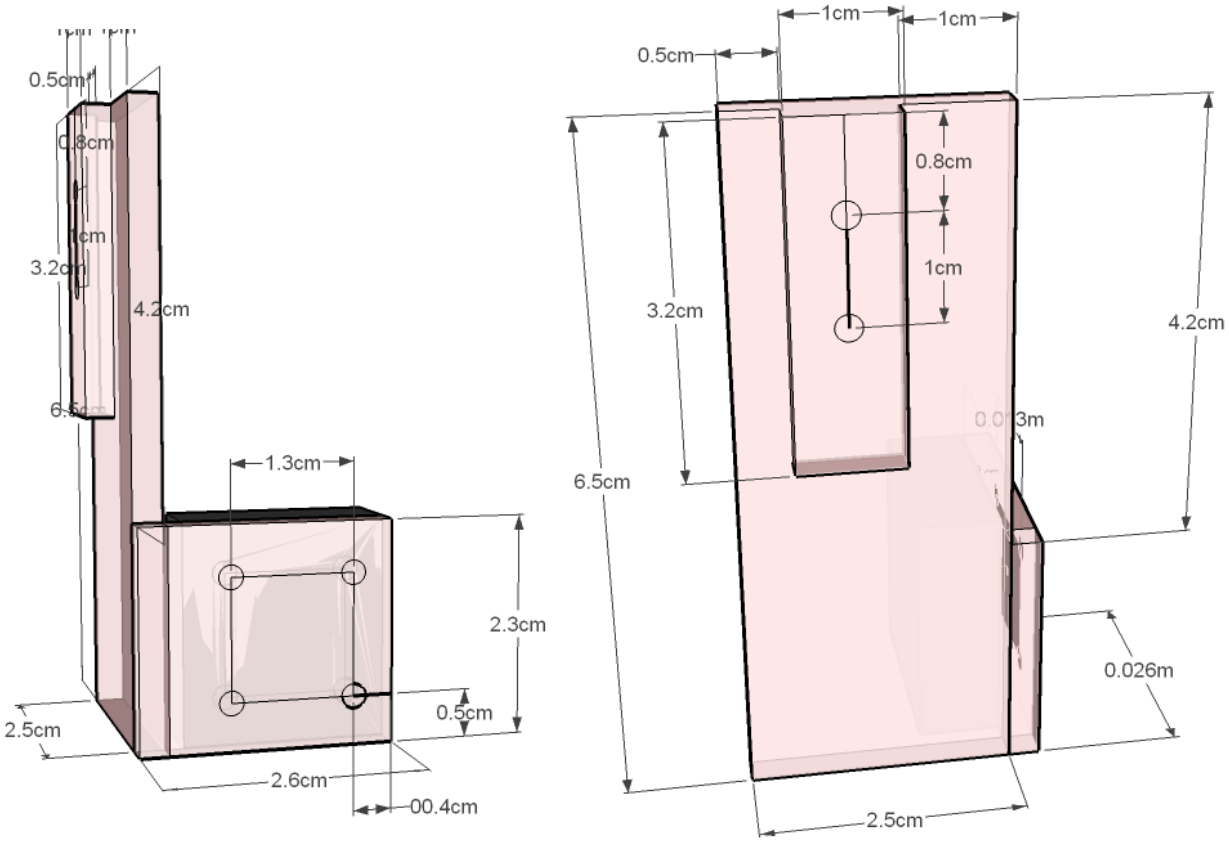

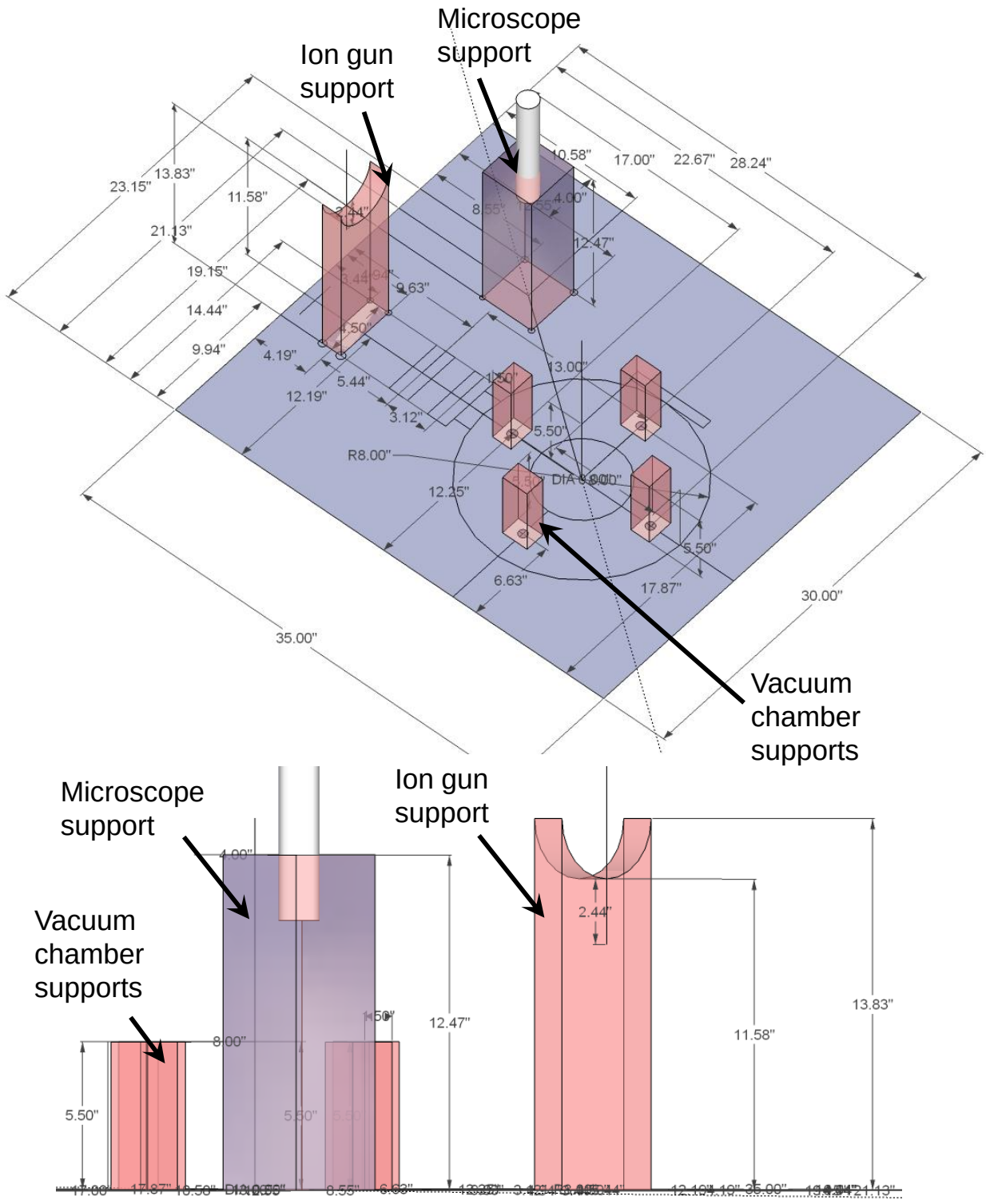

Figure B.1.6 Schematic drawing of aluminum supports and their placements on the air table shown in 3D (top), and side view (bottom).

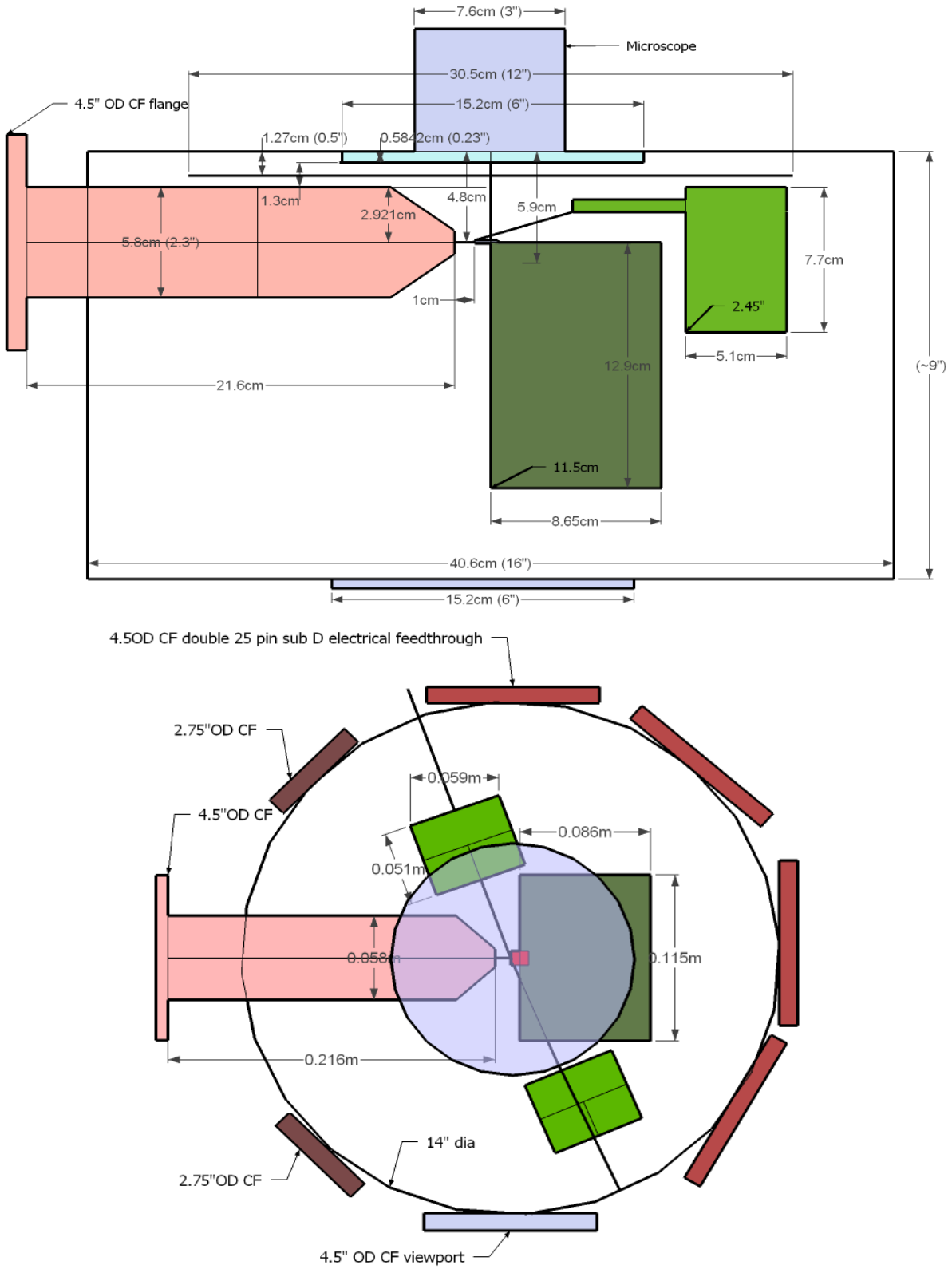

Figure B.1.7 Schematic drawings of the vacuum chamber interior and component sizes with relevant dimensions. TOP: side view; BOTTOM: side view.

B.2

Ion Gun Data

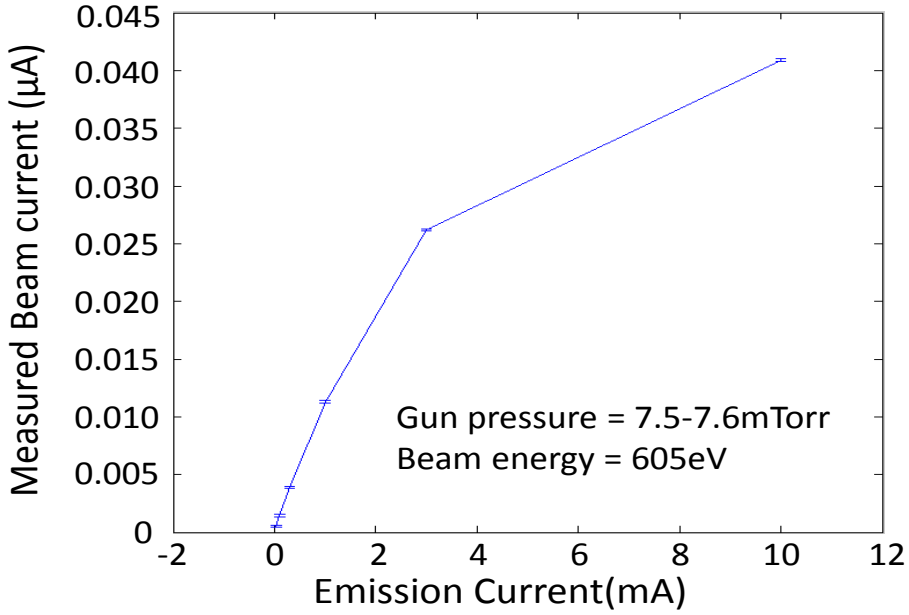

Figure B.2.1 Measured beam current as a function of emission current

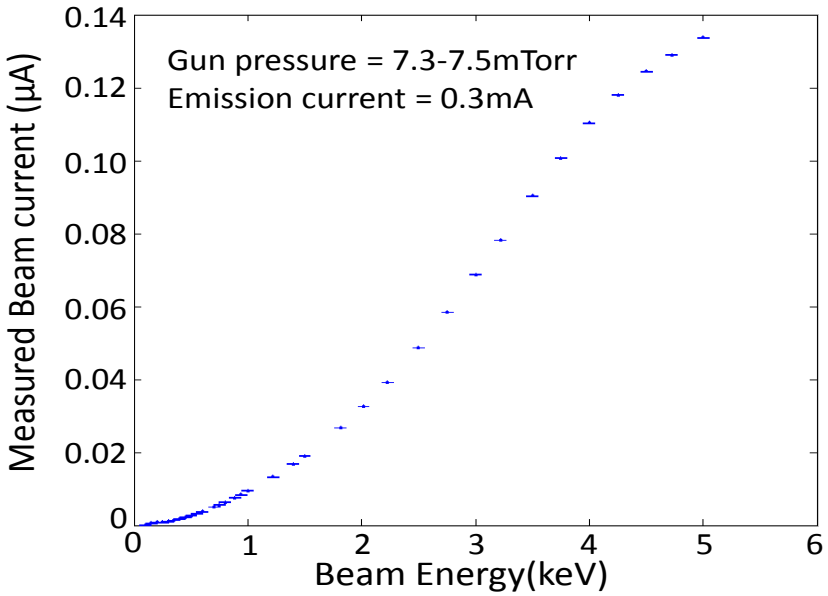

Figure B.2.2 Measured beam current is affected by energy of ion beam.

B.3

Labview Programs

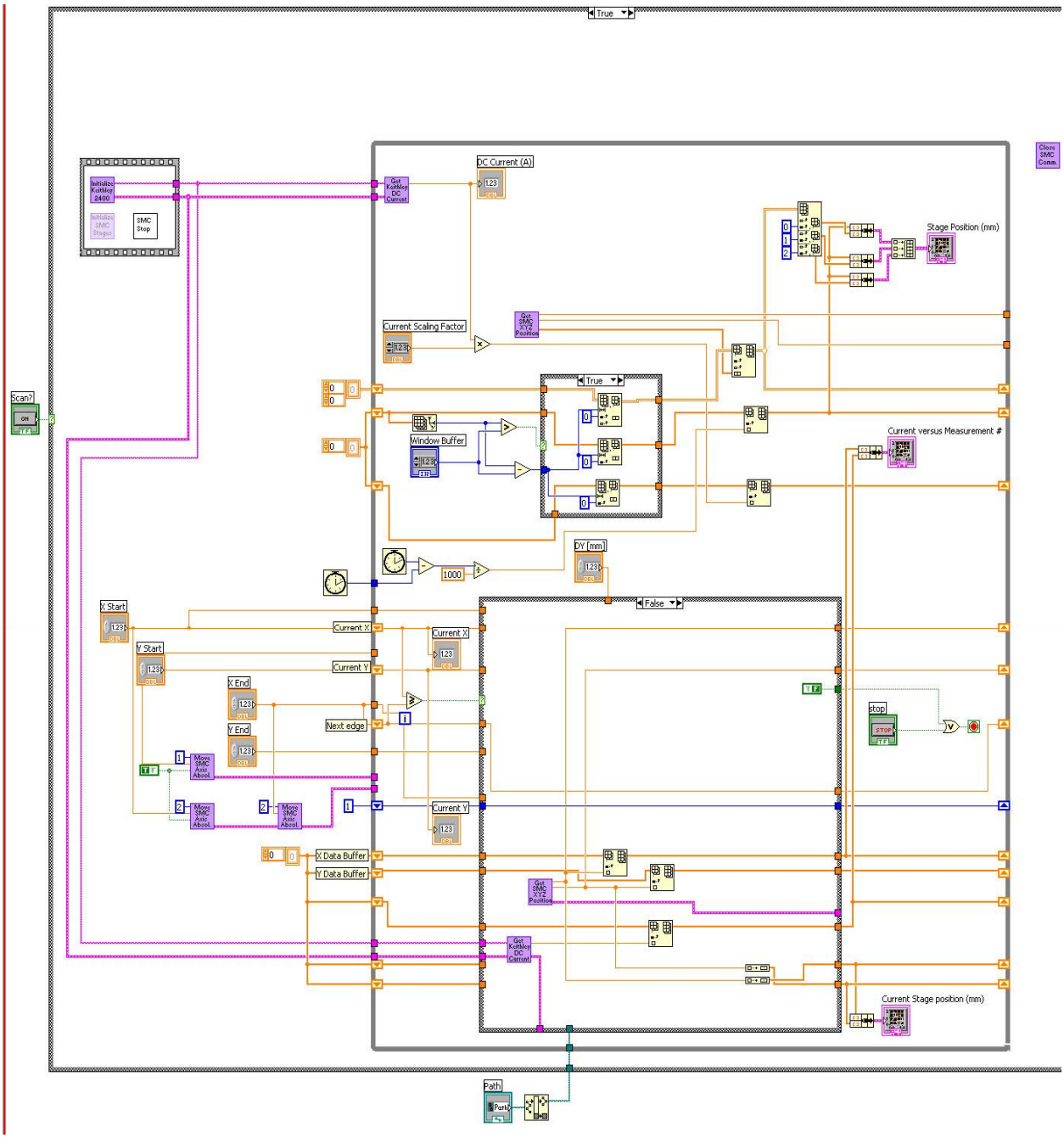

Figure B.3.1 Labview program to raster movement of microstage while taking current signal data from Keithley 2400, which are saved into file.

Bibliography

[1] O'Hanlon, *A User's Guide to Vacuum Technology*.: Wiley & Sons, 1980.

[2] Rouki et. al., "Ultra-high vacuum compatibility measurements of materials for the CHICSi detector system," *Physica Scripta. Vol. T104*, pp. 107-108, 2003.

[3] Alexi Assmus, "Early History of X Rays," *SLAC Beam Line*, 1995.

[4] Wilson, *An Introduction to Particle Accelerators*.: Oxford Scholarhip Online, 2001.

[5] Wangler, *RF Linear Accelerators*.: Wiley Series in Beam Physics and Accelerator Technology, 1998.

[6] Lawrence and Edelfsen, *Science, 72*, pp. 376-7, 1930.

[7] Cornell High Energy Synchrotron Source. [Online]. http://www.chess.cornell.edu/

[8] Accelerator - Fermilab's Tevatron. [Online]. http://www.fnal.gov/pub/science/accelerator/

[9] Large Hadron Collider. [Online]. http://lhc.web.cern.ch/lhc/

[10] Reiser, *Theory and Design of Charged Particle Beams*.: Wiley & Sons, 1994.

[11] Pierce, *Theory and Design of ELectron Beams*. New York: Van Nostrand, 1954.

[12] Avaldi et. al., *Nuclear Instruments and Methods in Physics Research B49*, pp. 24-28, 1990.

[13] H. Paul, *Nuclear Instruments and Methods in Physics Research B3*, pp. 5-10, 1984.

[14] Avaldi et. al., *Nucl. Instr. Meth. Phys. Res. A299*, pp. 240-245, 1990.

[15] Weinrich, "Recent Advanced for Ion Beam Therapy Accelerators Using Synchrotrons," *Nuclear Instruments and Methods in Physics Research Section B: Beam Interations with Materials and Atoms, Vol 269*, pp. 2879-2881, 2011.

[16] Schulz-Ertner et. al., "Radiation Therapy with Charged Particles," *Seminars in Radiation Oncology, Vol 16*, pp. 249-259, 2006.

[17] Kraft, "Tumortherapy with Ion Beams," *Nuclear Instruments and Methods in Physics Research Section A: Accelerators, Spectrometers, Detectors and Associated Equipment, Vol 454*, pp. 1-10, 2000.

[18] Melngailis, "Focused Ion Beam Technology and Applications," *J. Vacuum Science & Technology B:*

Microelectronics and Nanometer Structures Vol 5, pp. 469-495, 1987.

[19] Syms and Ahmad, "Tow-dimensional microfabricated electrostatic Einzel lens," *Sensors and Actuators A 107*, pp. 285-295, 2003.

[20] Despont et. al., "MIcrofabrication of Lenses for a Miniaturized Electron Column," *Microelectronic Engineering 27*, pp. 467-470, 1995.

[21] Kratschmer et. al., "Experimental evaluation of a 20x20mm footprint microcolumn," *J.Vac.Sci. Technol. B 14*, p. 3792, 1996.

[22] Chang et. al., "Arrayed miniature electron beam columns for high throughput sub100nm lithography," *J. Vac. Sci. Technol. B 10*, p. 2743, 1992.

[23] Saile, *LIGA and Its Applications*.: Wiley, 2009.

[24] Humphries, *CHarged Particle Beams*.: Wiley & Sons, 1990.

[25] Miller, *Intense Charged Particle Beams*. New York: Plenum Press, 1985.

[26] Ouyang and Cooks, "Miniature Mass Spectrometers," *Annu. Rev. Anal. Chem.* , pp. 187-214, 2009.

[27] Rudd, "Electrostatic Analyzers," in *Low Energy Electron Spectrometry*. New York: Wiley-Interscience, 1972, pp. Chap.2, Section 3.

[28] Davis, Coplan Moore, *Building Scientific Apparatus*.: Perseus Books, 2002.

[29] Rohm and Haas Electronic Materials, MEGAPOSIT SPR 220 series photoresists for i-Line Applications, Sep. 2004.

[30] CNF Lab Users Site. [Online]. http://www.cnfusers.cornell.edu/

[31] AZ Electronic Mateirals. Photoresist Developers. [Online]. http://www.azem.com/en/Products/Litho-technology/Photoresist%20Developers.aspx

[32] Shipley Report, "Micropost Remover 1165,".

[33] Keithley, A Tektronix Company. [Online]. http://www.keithley.com/products/dcac/voltagesource/broadpurpose/?mn=2400

[34] Ouyang and Cooks, "Miniature Mass Spectrometers," *Annual Review of Analytical Chemistry 2*, pp. 187-214, 2009.

[35] Gao et. al., "Handheld retilinear ion trap mass spectrometer," *Anal. Chem. 78*, pp. 5994–6002, 2006.

[36] Gao et. al., "Design and characterization of a multisource hand-held tandem mass psectrometer," *Anal. Chem. 80*, pp. 7198-7205, 2008.

[37] Collins et. al., "PET imaging for gene & cell therapy," *Current Gene Therapy 12*, pp. 20-32, 2012.

[38] Wangler, *RF Linear Accelerators*.: Wiley & Sons, 1998.

[39] Livingood, *Principles of cyclic particle accelerators*. New York: Van Nostrand, 1961.

[40] Danon Geuther, *J. Appl. Phys. 97*, p. 074109, 2005.

[41] Danon, Saglime Geuther, *Phys. Rev. Lett. 96*, p. 054803, 2006.

[42] T. Ditmire, *Optics & Photonics News*, p. 29, May 2002.

[43] Fortagh et al., *Science, Vol 307*, p. 860, 2005.

[44] Turchette, *PRA, Vol 61*, p. 063418.

[45] Wangler, *RF Linear Accelerators*.: Wiley & Sons, 1998.

[46] Sonnet Software Inc. High Frequency Electromagnetic Software. [Online]. http://www.sonnetsoftware.com/

[47] Melngailis, "Focused Ion Beam Technology and Applications," *J. Vacuum Science & Technology B: Microelectronics and Nanometer Structures Vol 5*, pp. 469-495, 1987.

[48] Weinrich, "Recent Advanced for Ion Beam THerapy ACcelerators Using Synchrotrons," *Nuclear Instruments and Methods in Physics Research Section B: Beam Interations with Materials and Atoms, Vol 269*, pp. 2879-2881, 2011.

[49] Schulz-Ertner et. al., "Radiation Therapy with Charged Particles," *Seminars in Radiation Oncology, Vol 16*, pp. 249-259, 2006.

[50] Kraft, "Tumortherapy with Ion Beams," *Nuclear Instruments and Methods in Physics Research Section A: Accelerators, Spectrometers, Detectors and Associated Equipment, Vol 454*, pp. 1-10, 2000.

[51] Ruska, "The Early Development of Electron Lenses and Electron Microscope," *Seiten*, p. 140, 1980.

[52] Carey, *Optics of Charged Particles Beams*. New York: Harwood Academic Pub., 1987.

[53] Wollnik, *Optics of Charged Particles*. Orlando, Fl: Academic Press Inc., 1987.

[54] Read Harting, *Electrostatic Lenses*. Amsterdam and New Yok: Elsevier Scientific Pub. Co., 1976.

[55] Hawkes, "Recent advances in electron optics and electron microscopy," *Annales de la Fondation Louis de Broglie, Vol 29*, pp. 837-855, 2004.

[56] COBHAM. Opera-3d - electromagnetic design in three dimensions. [Online]. http://www.cobham.com/about-cobham/aerospace-and-security/about-us/antenna-systems/kidlington/products/opera-3d.aspx

[57] Davis, Coplan Moore, *Building Scientific Apparatus, 3rd Ed.* MA: Perseus Books, 1989.

[58] Heddle, *Electrostatic Lens Systems*. Bristol, Philadelphia, New York: Adam Hilger, 1991.

[59] SIMION Version 8.0.

[60] COBHAM, Opera 3D - electromagnetic deisng in three dimensions.

[61] RBD Instruments. [Online]. http://www.rbdinstruments.com/

[62] SPECS GmbH - Surface Analysis, Ion Source IQE 12/38 Operation Manual 1.6, April 8, 2008.

[63] MICOS USA. [Online]. http://www.micosusa.com/

[64] Hao et. al., "Cathodoluminescence of silicon in the visible–ultraviolet region," *Phys. Rev. B57*, pp. 12841-12846 , 1998.

[65] J.S. Townsend, "Motion of Electrons in Gases," *Journal of the Franklin Institute 200*, p. 563, 1925.

[66] Carazzetti et. al., "Experimental study of electrical breakdown in MEMS devices with micrometer scale gaps," *Proc. of SPIE vol.6884*, p. 688404, 2008.

[67] Chen et. al., "Electrical breakdown phenomena for devices with micron separations," *J. Micromechanics and Microengineering Vol.16*, pp. 1366-1373, 2006.

[68] Cobine, *Gaseous Conductors*. Dover, 1941.

[69] F.Strong et. al., "Electrical Breakdown across micron scale gpas in MEMS structures," in *SPIE vol. 6111*, 2006.

[70] Wallash et. al., "Electrical breakdown and ESD phenomena for devices with nanometer-to-micron gaps," *Proc. SPIE vol.4980*, p. 87, 2003.

[71] R. Gomer, *Field Emission and Field Ionization*.: Harvard Press, 1961.

[72] Torres and Dhariwal, "Electric Fild breakdown at micrometer separations in air and vacuum," *Microsystems Technologies 6*, pp. 6-10, 1999.

[73] Xiong et. al., "Research on electric field and electric breakdown problems of a micro-colloid thruster," *Sensors and Actuators A 108* , pp. 134-137, 2003.

[74] Pfeiffer Vacuum GmbH, *The Vacuum Technology Book*.

[75] Wrulich, "SIngle-beam lifetime," in *CERN Accelerator School, Fifth General Accelertor Physics Course, CERN 94-01*., p. 409.

[76] Franzke, "Interaction of stored ion beams with the residual gas," in *CERN Accelerator School, Fourth Advanced Accelerator Physics Course, CERN 92-01*., p. 100.

[77] Davis, Coplan Moore, *Building Scientific Apparatus*. Cambridge, MA: Perseus Books.

[78] LPKF Laser & ELectronics, The Swiss Army Knife of the Laboratory, Micro-Material Processing with the LPKF ProtoLaser U3.

[79] Humphries, *Charged Particle Beams*.: Wiley & Sons, 1990.

[80] Mesyats and Uimanov, "On the Limiting Density of Fild Emission Current from Metals," *IEEE Transactions on Dielectrics and Electrical Insulation, Vol.13, No.1*, pp. 105-110, 2006.

[81] Fursey, "Field Emission in Vacuum Micro-electronics," *Applied Surface Science*, pp. 113-134, 2003.

[82] Bumgess et. al., "Connected values for Fowler-Nordheim field emission function Q(y)and S(y)," *Physical Review 90*, 1953.

[83] Vasil'ev Elinson, *Field Emission*. Moscow: Fizmatgiz, 1958.

[84] Dolan, "Current density tables for field emission theory," *Physical Review 91 (3)*, pp. 510-511, 1953.

[85] Martin et. al., "Stable, high density field emission cold cathode," *J. Appl. Phys. 31 (5)*, pp. 782–789, 1960.

[86] Trolan Barbour, "Electrical stability and life of the heated field emission cathode," *J. Appl. Phys. 31 (5)*, pp. 790–805, 1960.

[87] Wideroe, *Arch. Electrotech. 21*, p. 387, 1928.